A STUDY OF THE TIME AND ENERGY VARIATION OF FAST NEUTRON PULSES IN SOME REACTOR MATERIALS

A dissertation submitted for the award of the

Doctor of Philosophy Degree

of the University of London

by

Richard Sau Hin Lee, B.Sc.

Nuclear Power Section

Department of Mechanical Engineering

Imperial College

June 1969

ABSTRACT

The behaviour of fast monoenergetic neutron pulses in the 1 to 3 MeV range in iron (Fe^{56}), a typical medium weight, non-multiplying nucleus, has been investigated. The 6 MeV/5 Mc/s Van de Graaff at A.W.R.E., Aldermaston, was used to generate bursts of 4×10^{-9} s monoenergetic neutron pulses by the T(p,n) He^3 reaction, the pulses being collimated and injected into iron blocks. An attempt was made to measure the decay spectra of the leaking neutrons by employing a fast scintillation counter and nanosecond time-of-flight electronics with energy gating applied.

The decay constant, if it exists, is a function of the assembly size and the non-elastic cross-section. This dependence is explicit in the analytical solution (expansion method) of the one-velocity, time dependent Boltzmann transport equation and is implicit in the numerical solution (Discrete Ordinates Method) through solving for the neutron fluxes. The latter method has been modified to calculate decays in non-multiplying media.

The experimental results have been compared with theoretical predictions. Sets of point non-elastic cross-section data for iron have been checked and the sensitivity of the dependence was tested by changing the data by fixed percentages whilst keeping the total cross-sections constant. Two primary neutron energies were selected at 1.285 and 2.427 MeV and two sizes of 12" x 12" x 12" and 15 x 15" x 18" were employed.

ACKNOWLEDGEMENTS

The author wishes to thank his supervisor, Professor P.J. Grant, for the constant guidance and encouragement throughout the course of this project. Special thanks are due to Dr. A.J.H. Goddard for the many interesting discussions and advice which have proved to be of great value. He is grateful to the Staff of the Neutron Physics Research Section at A.W.R.E., Aldermaston for the use of their Van de Graaff generator and acknowledges the assistance offered to him. The technical staff of the Nuclear Power Section, especially Messrs. G. Slater and N. Keats also deserve mention for their part in helping to construct some of the apparatus. The author is greatly indebted to the Commonwealth Scholarship Commission of the Association of Commonwealth Universities, United Kingdom, for having awarded him a Scholarship to carry out this project and expresses his gratitude to the Sabah Government for having nominated him. Finally he wishes to thank Miss Hudgell for typing this thesis.

CONTENTS

	Page
TITLE	1
ABSTRACT	2
ACKNOWLEDGEMENTS	3
CONTENTS	4
LIST OF SYMBOLS	6
CHAPTER 1 INTRODUCTION	7
CHAPTER 2 THEORETICAL DETERMINATION OF THE TIME DECAY CONSTANT	13
2.1 Formulation of the Problem	13
2.2 Co-ordinate Systems	15
2.3 The Simple Analytical Approach	20
2.4 Correction for First Order Anisotropy	24
2.5 The Method of Discrete Ordinates (DSN)	26
CHAPTER 3 THE ITERATIVE SOLUTION OF THE DISCRETE ORDINATES METHOD	37
3.1 The Difference Equations	37
3.2 Inner Iterations	40
3.3 Outer Iterations	43
3.4 Errors and Limitations	46
3.5 The 'DISCORD' Programme	47
CHAPTER 4 THE VELOCITY OF LIGHT EXPERIMENT	53
4.1 Principle of the Experiment	53
4.2 Time Resolution Consideration	55
4.3 Apparatus	64
4.4 Experimental Procedure	68
4.5 Results and Analysis	70

CHAPTER 5
FAST PULSED NEUTRON DECAY MEASUREMENTS IN IRON 78

5.1 Apparatus 79

5.2 Energy Determination 87

5.3 The Integral Proton Spectrum 94

5.4 The Prompt Neutron Time Spectrum 102

5.5 Neutron Decay Measurements 109

CHAPTER 6
ANALYSIS OF NEUTRON DECAY DATA 112

6.1 Analysis Part I 112

6.2 Comparison with Theoretical Calculations 113

6.3 Analysis Part II 119

CHAPTER 7
CONCLUSION 138

REFERENCES 141

LIST OF SYMBOLS

$\phi(\underline{r},\underline{\Omega},E,t)$ = angular flux of neutrons at point $\underline{r}$ in unit energy interval at E travelling within unit solid angle about the direction $\underline{\Omega}$ and crossing unit area normal to $\underline{\Omega}$ in unit time at t.

$\phi(\underline{r},E,t)$ = $\int_{\Omega} \phi(\underline{r},\underline{\Omega},E,t)d\Omega$ is the scalar flux of neutrons in unit volume at point $\underline{r}$ in unit energy interval at E and at time t.

$S(\underline{r},\underline{\Omega},E,t)$ = source of neutrons at point $\underline{r}$ in unit solid angle about $\underline{\Omega}$ in unit energy interval at E per unit time t.

$\Sigma_s(\underline{r},\underline{\Omega}\rightarrow\underline{\Omega}',E\rightarrow E')$ = differential scattering cross-section.

$\Sigma_s(\underline{r},E)$ = macroscopic total scattering cross section (cm^{-1}).

$\Sigma_a(\underline{r},E)$ = macroscopic absorption cross-section (cm^{-1}).

$\Sigma_{ne}(\underline{r},E)$ = macroscopic non-elastic cross-section (cm^{-1}).

$\Sigma_T(\underline{r},E)$ = macroscopic total cross-section (cm^{-1}).

$\Sigma_f(\underline{r},E)$ = macroscopic fission cross-section.

λ = neutron time decay constant (sec^{-1}).

Note:- Macroscopic cross-sections in the DSN Method are designated by σ to avoid confusion with the summation sign Σ.

Other symbols are defined as they occur in the text.

CHAPTER 1

INTRODUCTION

A basic aim in reactor physics research is to improve our knowledge of fundamental nuclear data by studying the behaviour, both static and kinetic, of neutrons over a wide range of energies in media typical of reactors. Under limiting conditions certain parameters are identifiable from such studies and from these parameters nuclear data may be measured or checked by comparison with theoretical predictions. Conversely if the data are known to a high degree of accuracy methods of calculation may be tested. In particular a kinetic experiment using a pulsed neutron source offers a means of determining the fundamental time decay constant (if it exists) which is characteristic of the neutron spectrum in a given medium. This parameter is a function of the non-elastic cross-section and therefore enables one to test sets of data by employing reasonably reliable theoretical calculations. This is in fact the underlying principle of the present project.

The application of the pulsed neutron technique to thermal systems, multiplying or not, is well known and both the theoretical and experimental aspects have been treated in the Brookhaven Conference on Neutron Thermalization (1962). However it is only in recent years that the technique has been extended to intermediate (keV) and fast (MeV) systems and the trend will probably continue in view of the increasing interest in fast reactors and the availability of intense nanosecond pulse generators such as the Van de Graaff. Excellent reviews of the application of fast pulsed neutrons to multiplying and non-multiplying media have been presented by Storrer and Beckurts in the Symposium on Pulsed Neutron Research held at Karlsruhe in 1965.

Consider the injection of a burst of neutrons into a bare assembly. It is arbitrary in spatial and spectral distributions and is a delta function in time. Initially excited spatial and spectral transients will obscure any interpretation of neutron behaviour. If, however, after a time the neutron population as a whole is found to decrease, through absorption and leakage, with a single dominant decay constant then we say that a discrete fundamental eigenvalue exists for that system. This exponential die-away will be in the nanosecond range for fast neutrons of 1 to 3 MeV as opposed to the millisecond range for thermal neutrons. In a thermal system with an established Maxwellian spectrum and a unique buckling (implying space and energy separability) an asymptotic mode persists, and, provided the thermalization time is shorter than the decay, can be measured. Unfortunately there is no such guarantee in a fast system where upscattering is absent since practically no neutrons will reach thermal energies. A feedback from low to high energies is effected only through fissions. Moreover, although the scattering mechanism (free atoms model) is much simpler than that in the thermal case, the fact that neutron reactions take place over a wide range of energies in which the collision rates may vary by orders of magnitude tends to complicate the problem. Thus it is argued that only in a multiplying system, and even then not too far below criticality, can a discrete eigenvalue be identified.

Generally, it is not meaningful to talk of a discrete eigenvalue in a fast non-multiplying medium because, without upscattering, the whole energy spectrum is continuously softened by the slowing down process so that an equilibrium spectrum is not attained. Each energy group will decay with its own characteristic constant giving rise to a continuum of eigenvalues. Consider, however, the case where the primary neutron pulse is fast and monoenergetic and the assembly is a

slab of under-moderating material. Under such limiting conditions there will be neutrons with the mean injection energy E_n leaking out of the system at a rate characteristic of the neutron population having energy E_n. Associated with E_n will be a width ΔE_n which is further broadened by elastic moderation inside the assembly, the broadening increasing as the material becomes more moderating. If we regard the neutrons as monoenergetic within the confine of ΔE_n then solution of the one-velocity time dependent Boltzmann transport equation (as shown by Nelkin) predicts the existence of a quasi-asymptotic decay constant. By performing an experiment in this spirit with the chosen neutron detector biased not to count those neutrons which have lost energy below a preset level it may be possible to determine a well-defined decay constant from the leakage spectrum measured. There will be no initial spectral transients although spatial ones will be present. Should a spatial mode be established before slowing down to another lower energy group occurs then a discrete eigenvalue is assured. It is the intention of the author to apply the above argument and attempt to measure decay constants for fast monoenergetic neutrons from 1 to 3 MeV in various iron blocks.

Beghian and co-workers at the Massachusetts Institute of Technology have conducted pulsed experiments on assemblies of bismuth, lead, natural uranium and iron using source neutron energies between 0.74 and 1.52 MeV. A Van de Graaff generator was used to produce monoenergetic neutron pulses (about 3×10^{-9} s long at a repetition rate of 8Mc/s) through the $Li^7(p,n)\,Be^7$ reaction. Detection was by a scintillation counter with a 1" diameter by 1" thick plastic phosphor and analysis was by nanosecond time-of-flight electronics, the resolution being about 4 ns. For iron measurements were made at 0.74, 0.93, 1.04, 1.15, 1.27, 1.39 and 1.52 MeV. Typical assembly sizes ranged from 12" x 12" x 12" to 18" x 18" x 18". In all cases definite decay periods from 6 to 30 ns were

reported to have been obtained when certain energy gatings were applied. The decays were then fitted to the expansion formula

$$\lambda = v\,\Sigma_{ne} + vDB_g^2 + CB_g^4 + \ldots \qquad 1.1$$

where the symbols have their usual meaning. The non-elastic cross-section was determined by an iterative procedure using the above equation and an initial guess value. The method of fitting was claimed to be good in spite of the fact that only 4 bucklings were used. C was regarded purely as a curve fitting constant. The error was around 15% attributed mainly to uncertainties in the total cross-section (Σ_T) and the average cosine of scattering (μ_o) used. Somewhat similar measurements were later made by d'Oultremont et al. in Belgium on carbon, copper and iron at energies of 0.67, 0.87, 1.1 and 1.4 MeV. P_1 and Monte-Carlo calculations were adopted to interpret the results which were not analysed on a monoenergetic basis. Moreover it was stressed that the objective was a feasibility study and was therefore not "biased" to determine decay constants. The conclusion was that if moderating effects were weak the neutron density *appeared* to decay exponentially. Small wonder then that a lively discussion developed between Beghian and d'Oultremont in the Symposium on Pulsed Neutron Research! In Japan, Hiraoka et al. pulsed lead and natural uranium cubes and decay curves have been measured for neutron energies in the ranges 0.8 - 1.2 MeV, 2.5 - 3.5 MeV and 4.5 - 5.8 MeV. It would seem that they did not adopt a one-velocity model in their calculations which were not very clear anyway because their theoretical analysis was still in progress at that time.

For the present work iron has been chosen as the medium for two reasons. Firstly it is a medium weight nucleus in which neutron energy

degradation by elastic moderation becomes somewhat significant and it will be interesting to see whether an asymptotic decay can be measured in the presence of this moderating effect. Secondly the non-elastic cross-section of iron exhibits many narrow resonances separated by tens of keV only; it is desirable to find out to what extent the neutron energy resolution ΔE_n can take into account the resonance widths. The method of detection is a plastic phosphor-photomultiplier combination. This detector has a very good time resolution, fairly good energy resolution and is quite sensitive to fast neutrons. The outputs can be fed direct to the fast nanosecond time-of-flight electronic system for the decay spectrum analysis. A suitable Van de Graaff will be used to yield neutrons via the T(p,n) He^3 reaction. The usual theoretical procedure of evaluating the decay constant is to fit it to the expansion expression (equation 1.1) using a method of least squares. In cases where measurements can be made with only a few bucklings least squares fitting would be impracticable. Instead Σ_{ne} and D are taken and computed from a set of data and used to calculate λ. The constant C can be shown to have a theoretical value (see Chapter 2) although experimentalists tend to regard it as a fitting constant. An alternative method which does not depend on expansion is the numerical solution of the time-dependent Boltzmann transport equation. A typical method is the Discrete Ordinates Method (DSN) originally due to Carlson and will be adopted by the author because of its recursive algorithms which are appropriate for calculation on a fast computer. This method has a distinct advantage over diffusion theory in that it does not assume a buckling (extrapolated distance) in the direction of neutron flow which is to be solved. The spatial flux shape is determined solely by convergence of the iterative procedure. The decay constant is fed in as an eigenvalue which is encouraged to converge as calculation proceeds.

Existing DSN computer codes do not make a proviso for time eigenvalue determination in the case of non-multiplying media, i.e. a fission source is always assumed whenever a homogeneous problem is to be solved. The method will therefore be modified to perform an eigenvalue determination in a non-multiplying medium which is the case in hand.

CHAPTER 2

THEORETICAL DETERMINATION OF THE TIME DECAY CONSTANT

In this chapter the Boltzmann Transport Equation expressing neutron balance is solved under various simplifying assumptions and, assuming that a discrete time decay constant does exist the latter is obtained both analytically and numerically. The analytical approach has been vigorously examined by Nelkin and his method as applied to the problem in hand will be derived and discussed. For the numerical solution the method of Discrete Ordinates (DSN) originally due to Carlson has been adopted and it will be showr how the method has been modified to determine the time eigenvalue in the case of neutron decay in a non-multiplying medium.

2.1 FORMULATION OF THE PROBLEM

The behaviour of neutrons in a given system is governed by the Boltzmann Transport Equation which is given as

$$\frac{1}{v}\frac{\partial\phi}{\partial t} = -[\underline{\Omega}.\nabla + \Sigma_T(\underline{r},E)]\phi + \int_{E'}\int_{\Omega'} [\Sigma_s(\underline{r},\underline{\Omega}'\rightarrow\underline{\Omega},E'\rightarrow E) + \frac{\chi(E)}{4\pi}\nu\Sigma_f(\underline{r},E')]\,\phi'\,dE'd\Omega' + S(\underline{r},\underline{\Omega},E,t) \qquad 2.1$$

where $\phi = \phi(\underline{r},\underline{\Omega},E,t)$

$\phi' = \phi(\underline{r},\underline{\Omega}',E',t)$

$\Sigma_T(\underline{r},E) = \Sigma_a(\underline{r},E) + \Sigma_s(\underline{r},E)$

and

$$\Sigma_s(\underline{r},E) = \int_{E'}\int_{\Omega'} \Sigma_s(\underline{r},\underline{\Omega}\rightarrow\underline{\Omega}',E\rightarrow E')\,dE'd\Omega'$$

Fission is assumed to be an isotropic process. Equation 2.1 merely states that the rate of change of neutron density is equal to

gains from sources less the losses due to leakage and collisions.

Consider now the injection of a pulse of fast neutrons into a *non-multiplying* medium. At time t = 0 there will be a delta source but at t > 0, we have the equation

$$\left[\frac{1}{v}\frac{\partial}{\partial t} + \underline{\Omega}.\nabla + \Sigma_T(\underline{r},E)\right]\phi = \int_{E'}\int_{\Omega'} \left[\Sigma_s(\underline{r},\underline{\Omega}'\to\underline{\Omega},E'\to E) \times \phi'\, dE'd\phi'\right] \qquad 2.2$$

Other sources are assumed to be absent.

In general the neutron flux will be a non-separable function of position and energy. If, however, the time variable is regarded as separable, then the following series

$$\phi(\underline{r},\underline{\Omega},E,t) = \sum_n A_n\phi_n(\underline{r},\underline{\Omega},E)\, e^{-\lambda_n t} \qquad 2.3$$

is a general solution of 2.2. The λ_n are the eigenvalues and the ϕ_n the corresponding eigenfunctions. The coefficients A_n can be determined from the boundary conditions which may be specified at some particular time.

At t >> 0 the behaviour of $\phi(\underline{r},\underline{\Omega},E,t)$ will be described by one dominant eigenvalue λ_N and the corresponding eigenfunction $\phi_N(\underline{r},\underline{\Omega},E)$. The coefficient A_N has been incorporated into ϕ_N. Hence we have

$$\phi(\underline{r},\underline{\Omega},E,t) = \phi_N(\underline{r},\underline{\Omega},E)\, e^{-\lambda_N t} \qquad t >> 0 \qquad 2.4$$

$\lambda_N = |\lambda_n|_{min}$ is known as the fundamental time decay constant and is to be determined.

Substitution of 2.4 into 2.2 and dropping the subscript N, we get

$$[\underline{\Omega}.\nabla + \Sigma_T(\underline{r},E) - \lambda/v]\phi(\underline{r},\underline{\Omega},E) = \int_{E'}\int_{\Omega'} \Sigma_s(\underline{r},\underline{\Omega}'\to\underline{\Omega},E'\to E)\phi(\underline{r},\underline{\Omega}',E')\, dE'd\Omega' \qquad 2.5$$

λ/v has the dimension of macroscopic cross-section (cm^{-1}) and as such can be regarded as a "time absorption" cross-section. Solution of 2.5 will yield λ. The directional derivative term $\underline{\Omega}.\nabla$ expresses neutron leakage and its form depends on the co-ordinate system used. In order to simplify the problem we shall consider its form in one-dimensional geometry only.

2.2 CO-ORDINATE SYSTEMS

Consider a small distance $\underline{ds}$ along the direction $\underline{\Omega}$. Then, by definition (Wigner)

$$\underline{\Omega}.\nabla\phi = \frac{d\phi}{ds} \qquad 2.6$$

For the case of plane geometry (Fig. 2.2) the angular flux distribution depends on one spatial co-ordinate x and is symmetrical for rotation around the x axis. With μ defined as the cosine of the angle between $\underline{\Omega}$ and the x axis, we have

$$\underline{\Omega}.\nabla = \frac{d}{ds} = \mu \frac{d}{dx} \qquad 2.7$$

In spherically symmetric geometry the flux distribution has a component along the radius vector $\underline{r}$ and one along the μ direction, the latter representing flux distribution in curved space. Hence

$$\underline{\Omega}.\nabla = \frac{d}{ds} = \frac{\partial r}{\partial s}\frac{\partial}{\partial r} + \frac{\partial \mu}{\partial s}\frac{\partial}{\partial \mu} .$$

With reference to Fig. 2.3 we have

$$dr = \cos\theta\, ds \quad \text{and} \quad -rd\theta = \sin\theta\, ds,$$

the negative sign indicating that θ decreases as ds increases along $\underline{\Omega}$. Thus

$$\frac{dr}{ds} = \cos\theta = \mu$$

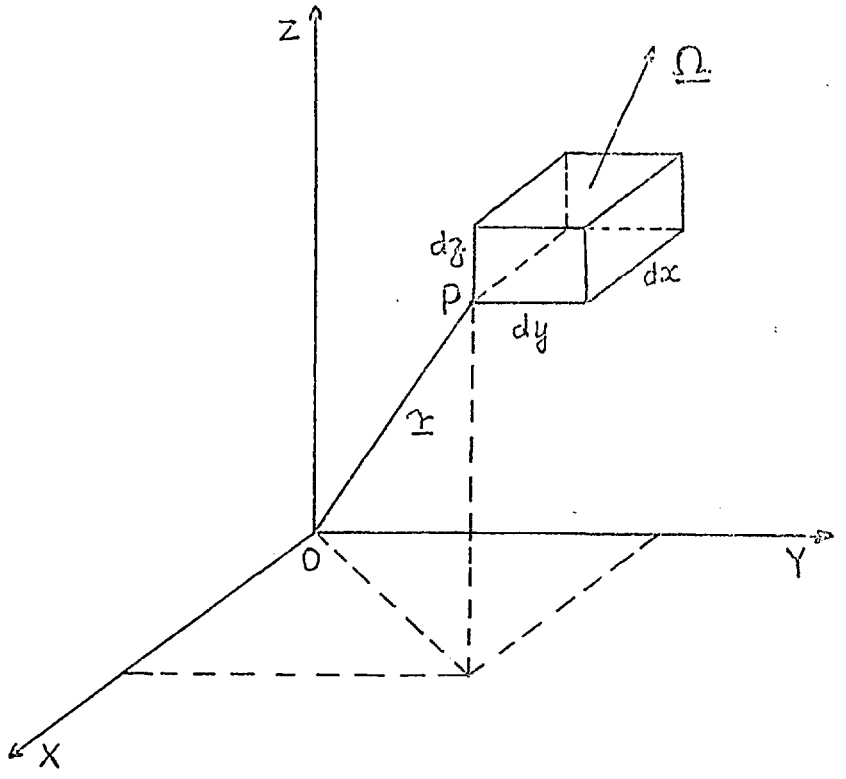


FIGURE 2.1 CO-ORDINATE SYSTEM

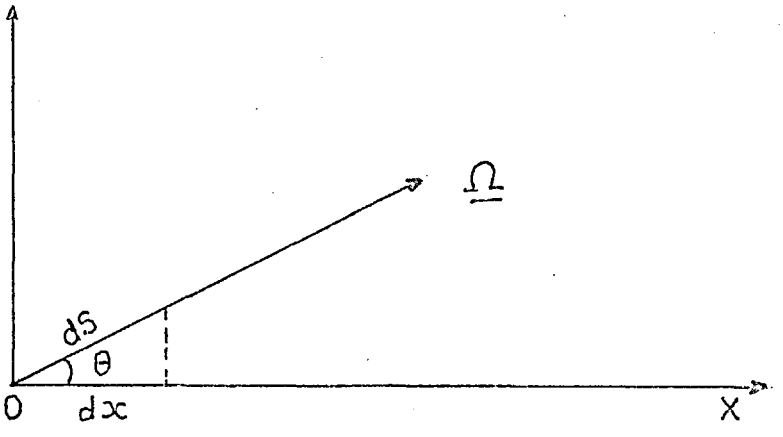


FIGURE 2.2 PLANE CO-ORDINATES

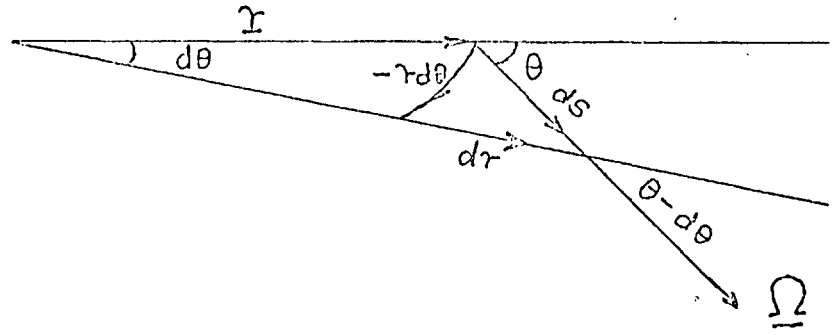


FIGURE 2.3 SPHERICAL CO-ORDINATES

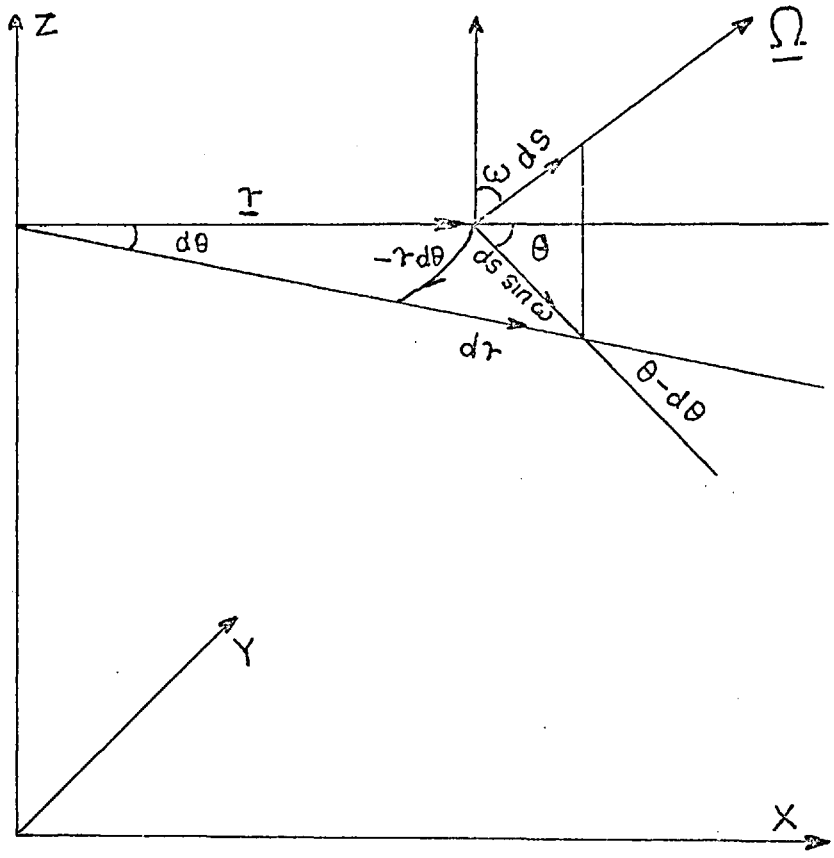


FIGURE 2.4 CYLINDRICAL CO-ORDINATES

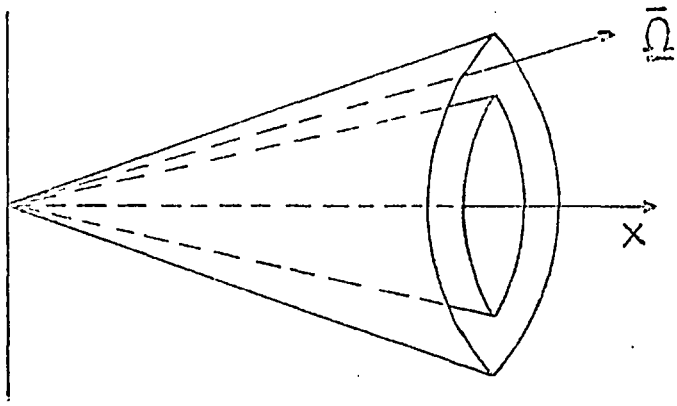


FIGURE 2.5 SOLID ANGLE REPRESENTATION FOR PLANE AND SPHERE

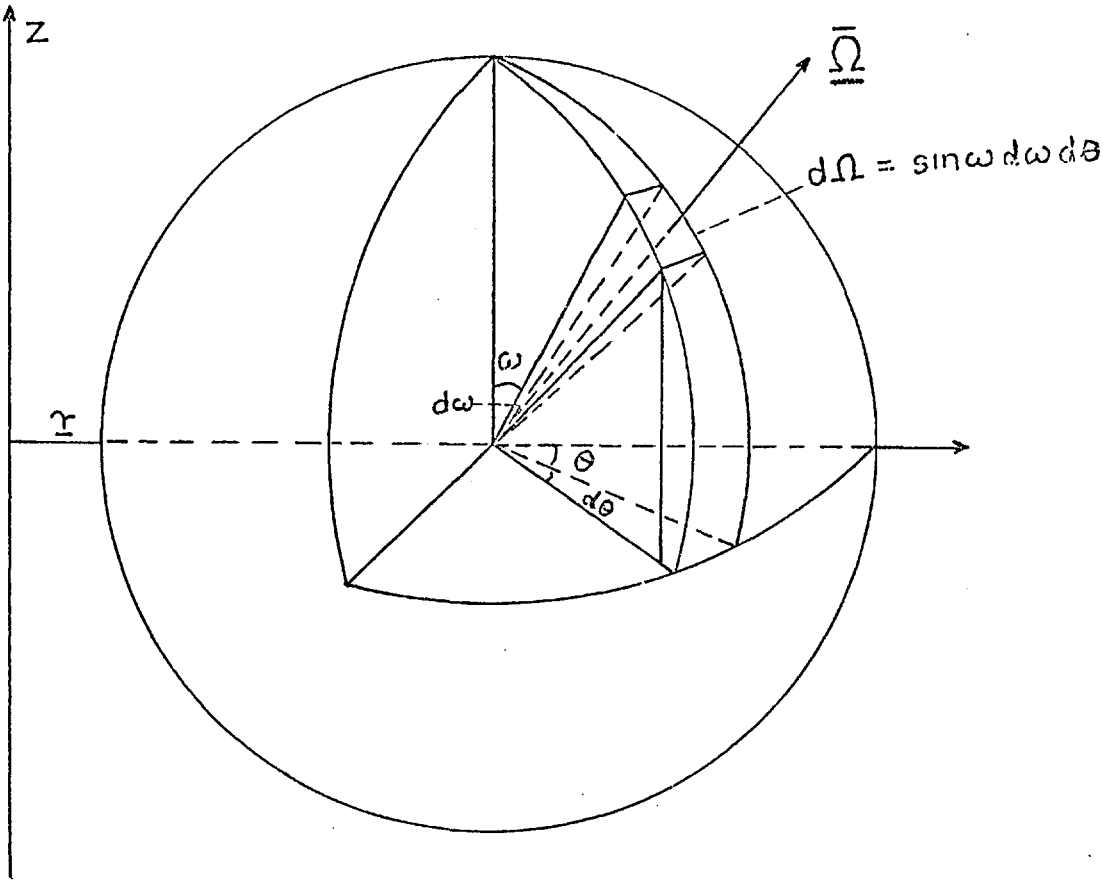


FIGURE 2.6 SOLID ANGLE REPRESENTATION FOR CYLINDER

$$r(-\sin\theta\, d\theta) = \sin^2\theta\, ds$$

$$\frac{d\mu}{ds} = \frac{1-\mu^2}{r}$$

so that

$$\underline{\Omega}.\nabla = \mu \frac{\partial}{\partial r} + \frac{(1-\mu^2)}{r} \frac{\partial}{\partial \mu} \qquad 2.8$$

For a cylindrically symmetric system, infinite in the axial (z) direction the angular flux will depend on two angular coordinates (ω,θ) and on the radius vector $\underline{r}$. θ is the angle between the projection of $\underline{\Omega}$ on to the horizontal plane section of the cylinder and the radius vector $\underline{r}$; ω is the angle between $\underline{\Omega}$ and the vertical axis. From Fig 2.4 we see that

$$\sin^2\omega\, (ds)^2 = (dr)^2 + (r d\theta)^2$$

$$dr = \sin\omega \cos\theta\, ds$$

$$-r d\theta = \sin\omega \sin\theta\, ds$$

with $\eta = \sin\omega$ and $\mu = \cos\theta$

$$\frac{dr}{ds} = \eta\mu \quad \text{and} \quad \frac{d\theta}{ds} = -\eta \frac{\sqrt{1-\mu^2}}{r}$$

since $$\underline{\Omega}.\nabla = \frac{\partial r}{\partial s} \frac{\partial}{\partial r} + \frac{\partial \theta}{\partial s} \frac{\partial}{\partial \theta}$$

we get

$$\underline{\Omega}.\nabla = \eta\{\mu \frac{\partial}{\partial r} - \frac{\sqrt{1-\mu^2}}{r} \frac{\partial}{\partial \theta}\} \qquad 2.9$$

Although only one-dimensional geometry has been treated, a correction to finite dimensions in the case of slabs and cylinders can be made in the numerical solution of the transport equation. This is the so-called "Buckling Absorption" and will be discussed later on. We shall now consider the determination of λ from

2.3 THE SIMPLE ANALYTICAL APPROACH

The basic procedure is to solve the Fourier Transformed Transport Equation from an infinite non-mulitplying homogeneous medium with a Cos Bx solution and express λ as an infinite series in the square of the Fourier transform variable B. In slab geometry equation 2.5 becomes

$$\left[\mu \frac{d}{dx} + \Sigma_T - \lambda/v\right] \phi(\underline{x},\underline{\mu},E)$$

$$= \int_{E'} \int_{o} \int_{-1}^{2\pi\ +1} \Sigma_s(\underline{\Omega}'\rightarrow\underline{\Omega},E'\rightarrow E)\phi(\underline{x},\mu,E')\ dE'\ d\Omega' \qquad 2.10$$

In order to illustrate the method, isotropic scattering will be assumed and a correction for first order anisotropy then applied. A fuller anisotropic treatment of the scattering cross-sections will be dealt with in a later section. Equation 2.10 is now given as

$$\left[\mu \frac{d}{dx} + \Sigma_T - \lambda/v\right] \phi(\underline{x},\mu,E)$$

$$= \frac{1}{2} \int_{E'} \int_{-1}^{+1} \Sigma_{so}(E'\rightarrow E)\phi(x,\mu,E')\ dE'\ d\mu \qquad 2.11$$

The important question of whether space and energy variables can be assumed to be separable now arises. In the case under consideration this assumption will hold. If it is also valid for a finite assembly (viz. the fluxes of all energies vanish at the same extrapolated end point) then a unique buckling B^2 can be ascribed to that system. This concept is shown to be valid by Williams provided an asymptotic energy spectrum is well established.

For the case of monoenergetic neutrons this question does not arise and since the experiment is based on a one velocity treatment we shall no longer consider energy dependence. We define the Fourier transform $\phi(B,\mu)$ as

$$\phi(B,\mu) = \int_{-\infty}^{\infty} \phi(x,\mu)\, e^{-iBx}\, dx \qquad 2.12$$

Multiplying 2.11 by e^{-iBx} and integrating over x, the first term on the L.H.S. yields

$$\int_{-\infty}^{+\infty} \mu \frac{\partial}{\partial x}\, \phi(\underline{x},\mu)\, e^{-iBx}\, dx = [\mu\phi(\underline{x},\mu)\, e^{-iBx}]_{-\infty}^{+\infty}$$

$$\therefore\ iB\mu \int_{-\infty}^{+\infty} \phi(\underline{x},\mu)\, e^{-iBx}\, dx \qquad 2.13$$

Since $\phi(\pm\infty,\mu) = 0$, the first term on the R.H.S. vanishes and the transform of 2.11 is

$$[\Sigma_T - \lambda/v + iB\mu]\phi(B,\mu) = \frac{\Sigma_{so}}{2} \int_{-1}^{+1} \phi(B,\mu)\, d\mu \qquad 2.14$$

The R.H.S. (integrated over μ) is independent of μ and so we can put

$$\phi(B,\mu) = \frac{\phi(B)}{[\Sigma_T - \lambda/v + iB\mu]} \qquad 2.15$$

where $\phi(B)$ is a function of B only.

Substituting (2.15) back into (2.14) gives

$$\phi(B) = \frac{\Sigma_{so}}{2}\, \phi(B) \int_{-1}^{+1} \frac{d\mu}{[\beta + iB\mu]} \qquad 2.16$$

with $\beta = \Sigma_T - \lambda/v = \Sigma_{so} + \Sigma_a - \lambda/v$

In general $\phi(B) \neq 0$ and therefore

$$\frac{\Sigma_{so}}{2iB} \ln\left[\frac{\beta + iB}{\beta - iB}\right] = 1 \qquad 2.17$$

Let $$\frac{1}{2i} \ln\left[\frac{\beta + iB}{\beta - iB}\right] = \theta$$

then $$\frac{\beta^2 - B^2}{\beta^2 + B^2} + \frac{2i\beta B}{\beta^2 + B^2} = e^{i(2\theta)}$$

i.e. $\cos 2\theta = \frac{\beta^2 - B^2}{\beta^2 + B^2}$ and $\sin 2\theta = \frac{2\beta B}{\beta^2 + B^2}$

giving $\theta = \tan^{-1}[B/\beta]$ which is real.

Define a function $f(B,\lambda) = \frac{1}{B} \tan^{-1}[\frac{B}{\beta}]$ 2.18

Since $\tan^{-1}[\frac{B}{\beta}] = \frac{B}{\beta} - \frac{1}{3}(\frac{B}{\beta})^3 + \frac{1}{5}(\frac{B}{\beta})^5 \ \ldots$

we see that $f(B,\lambda)$ is an even function of B and the expansion is in terms of B^2. λ is also expanded in terms of B^2, both expansions being carried out simultaneously. Nelkin expands λ as

$$\lambda = \sum_{j=0}^{\infty} \alpha_{2j} (iB)^{2j} \qquad 2.19$$

$$= \lambda_o + D_o B^2 - CB^4 + FB^6 + \ldots$$

Equation 2.17 now becomes

$$\frac{1}{f(B,\lambda)} - \Sigma_{so} \equiv 0 \qquad 2.20$$

The lowest order expansion of 2.20 is

$$[\Sigma_a + \Sigma_{so} - \lambda_o/v] - \Sigma_{so} = 0$$

so that $\lambda_o = v\Sigma_a$ 2.21

The expansion up to terms in B^2 is

$$\frac{\beta}{[1 - \frac{1}{3}(\frac{B}{\beta})^2 + \ldots]} - \Sigma_{so} = 0 \qquad 2.22$$

where β is now $\Sigma_a + \Sigma_{so} - \frac{\lambda_o}{v} - \frac{D_o}{v} B^2 = \Sigma_{so} - \frac{D_o}{v} B^2$.

Equation 2.22 can be written as

$$[\Sigma_{so} - \frac{D_o}{v} B^2] \quad \frac{1}{1 - \frac{B^2}{3\Sigma_{so}^2}(1 + \frac{D_o}{v\Sigma_{so}} B^2 + \ldots)} \quad - \Sigma_{so} = 0$$

which becomes

$$[\Sigma_{so} - \frac{D_o}{v} B^2] \quad \{1 + \frac{B^2}{3\Sigma_{so}^2} + \ldots\} \quad - \Sigma_{so} = 0$$

This leaves $[\frac{D_o}{v} - \frac{1}{3\Sigma_{so}}] \; B^2 = 0$

so that

$$\frac{D_o}{v} = \frac{1}{3\Sigma_{so}} = D \qquad 2.23$$

where D is known as the Diffusion Coefficient.

Continuing the expansion up to terms in B^4, equation 2.20 becomes

$$\frac{\beta}{[1 - \frac{1}{3}(\frac{B}{\beta})^2 + \frac{1}{5}(\frac{B}{\beta})^4 - \ldots]} \quad - \Sigma_{so} = 0 \qquad 2.24$$

with $\beta = \Sigma_{so} - \frac{D_o}{v} B^2 + \frac{C}{v} B^4$

This gives

$$\beta / \; [1 - \frac{B^2}{3\Sigma_{so}^2}\{1 - \frac{D_o}{v\Sigma_{so}} B^2 + \ldots\}^{-2} + \frac{B^4}{5\Sigma_{so}^4}\{1 - \frac{D_o}{v\Sigma_{so}} B^2 + ---\}^{-4}]$$

$$- \Sigma_{so} = 0$$

which becomes

$$\beta\{1 - \frac{B^2}{3\Sigma_{so}^2} + (\frac{1}{5\Sigma_{so}^4} - \frac{2D_o}{3v\Sigma_{so}^3}) B^4\}^{-1} - \Sigma_{so} = 0$$

Substituting for β,

$$(\Sigma_{so} - \frac{D_o}{v} B^2 + \frac{C}{v} B^4) \{1 + \frac{B^2}{3\Sigma_{so}^2} + (\frac{2D_o}{3v\Sigma_{so}^3} - \frac{4}{45\Sigma_{so}^4}) B^4 + \ldots\} - \Sigma_{so} = 0$$

$$[\frac{1}{3\Sigma_{so}} - \frac{D_o}{v}] B^2 - [\frac{1}{3\Sigma_{so}^2} (\frac{4}{15\Sigma_{so}} - \frac{D_o}{v}) - \frac{C}{v}] B^4 = 0$$

Therefore

$$\frac{C}{v} = \frac{1}{3\Sigma_{so}^2} \{\frac{4}{15\Sigma_{so}} - \frac{1}{3\Sigma_{so}}\} = -\frac{1}{45\Sigma_{so}^3}$$

whence $$C = -\frac{v}{45\Sigma_{so}^3} \qquad 2.25$$

The decay constant is therefore analytically expanded as

$$\lambda = v\Sigma_a + vDB_g^2 + CB_g^4 + \ldots \qquad 2.26$$

where B^2 is now identified with the geometrical buckling B_g^2 of a finite system. λ is expressed explicitly in terms of neutron velocity, the absorption cross-section and the buckling. No flux determination is necessary. The buckling for a rectangular system is as usual

$$B_g^2 = \pi^2 [\sum_{i=1}^{3} \frac{1}{(a_i + 2\lambda_{ext})^2}] \qquad 2.27$$

where the a_i are the dimensions and the extrapolated distance λ_{ext} is given as

$$\lambda_{ext} = 0.7104\ \lambda_{tr} \qquad 2.28$$

2.4 CORRECTION FOR FIRST ORDER ANISOTROPY

The assumption that scattering is isotropic in the laboratory system is generally not valid as there will be a preferential scattering

of the neutrons in the forward direction. The usual first order correction for this anisotropic is made by replacing the elastic scattering cross-section by an elastic transport cross-section defined as

$$\sigma_{s\ tr} = \sigma_{so}\ (1 - \bar{\mu}_o) \qquad 2.29$$

where $\bar{\mu}_o = \overline{\cos\theta}$ is the average cosine of the scattering angle per collision and given as (Yiftah et al.)

$$\bar{\mu}_o = \frac{\int_{-1}^{+1} \mu\sigma(\mu)\ d\mu}{\int_{-1}^{+1} \sigma(\mu)\ d\mu} \qquad 2.30$$

The differential scattering cross-section $\sigma(\mu)$ has been expressed as an expansion in a series of Legendre polynomials

$$\sigma(\mu) = \frac{\sigma_t}{4\pi} \sum_{\ell=0}^{\infty} \omega_\ell P_\ell(\mu) \qquad 2.31$$

so that to first order

$$\bar{\mu}_o \doteqdot \omega_1/3$$

The coefficient ω_1 has been measured experimentally at specific energies and from these plots $\bar{\mu}_o$ is obtained. It is to be noted that the non-elastic removals are considered to be isotropic.

A better expression for the diffusion coefficient is given by Glasstone and Edlund as

$$D = \frac{1}{3\Sigma_T(1-\mu_o)} \Big/ \left[1 - \frac{4}{5}\frac{\Sigma_a}{\Sigma_T} + \frac{\Sigma_a}{\Sigma_T} \cdot \frac{\bar{\mu}_o}{1-\mu_o} + \ldots\right] \qquad 2.32$$

2.5 THE METHOD OF DISCRETE ORDINATES (DSN)

The Method of Discrete Ordinates due to Carlson offers a useful numerical solution to the integro-differential Boltzmann transport equation (2.5) on a fast computer because of the iterative nature of its algorithms. In this method the energy dependence of the neutron flux is divided in IG distinct groups (multigroup representation) of width ΔE_g, g = 1 to IG with g = 1 the largest energy group. The group average of $\phi(\underline{r},\underline{\Omega},E)$ is defined as $\phi_g(\underline{r},\underline{\Omega},E)$ and the group angular flux of neutrons in ΔE_g is defined as

$$N_g(\underline{r},\underline{\Omega}) = \phi_g(\underline{r},\underline{\Omega})\ \Delta E_g \qquad 2.33$$

The spatial $\underline{r}$ dependence is represented by JM intervals with JM+1 space points and distance from the origin is therefore given by $\underline{r}_j$, j = 1 to JM+1. The surface area at r_j is denoted by A_j and the volume bounded by r_j and r_{j+1} is $V_{\overline{j}}$ (TABLE 2.1).

GEOMETRY	COORDINATE	$\underline{r}$	AREA	VOLUME
Plane	x	x_j	1	$x_{j+1} - x_j$
Cylinder	r	r_j	$2\pi r_j$	$\pi(r_{j+1}^2 - r_j^2)$
Sphere	r	r_j	$4\pi r_j$	$4\pi(r_{j+1}^3 - r_j^3)/3$

TABLE 2.1. ONE DIMENSIONAL GEOMETRIC REPRESENTATIONS

To represent the directional coordinate $\underline{\Omega}$ (Figs 2.2, 2.3, 2.4) discrete directions $\underline{\Omega}_m$, m = 1 to NN, are chosen and associated with each direction is a solid angle ω_m. The $(\underline{r},\underline{\Omega})$ representations from a mesh of JM.N (N = NN-1) "cells", (Figure 2.7) each cell being bounded by two spatial coordinate edges r_j and r_{j+1} and by two "angular edges" which are in fact the boundaries of the solid angles (Figs 2.5, 2.6).

In order to illustrate clearly the discrete form of the Boltzmann equation we shall have need to deal with local averages of the angular flux $N_g(\underline{r},\underline{\Omega})$. These "locals" are defined as certain weighted averages of N over the faces and interior of a $(\underline{r},\underline{\Omega})$ cell (Fig. 2.8). If a cell is solved (i.e. the right fluxes and neutron balance obtained) then a summation over the mesh gives the overall solution. Firstly, the flux in the centre of the cell is averaged over the volume V_j and the solid angle ω_m, is defined as

$$N_{g,\bar{j},\bar{m}} = \int_{V_{\bar{j}}} \int_{\omega_m} N_g(\underline{r},\underline{\Omega})\, d\Omega\, dV/V_{\bar{j}}\, \omega_m \qquad 2.34$$

The average over the area A_j at r_j and over ω_m is

$$N_{g,j,\bar{m}} = \int_{A_j} \int_{\omega_m} N_g(\underline{r},\underline{\Omega})\, d\Omega\, dA/A_{\bar{j}}\, \omega_m \qquad 2.35$$

and that over A_{j+1} at r_{j+1}, $N_{g,j+1,\bar{m}}$ is similarly defined. The average over the cell between r_j and r_{j+1} and over the angular edge of the directional cell is defined as

$$N_{g,\bar{j},m} = \int_{\alpha_{\bar{j},m}} N_g(\underline{r},\underline{\Omega})\, d\alpha/\alpha_{\bar{j},m} \qquad 2.36$$

with a similar definition for $N_{g,\bar{j},m+1}$. These local averages are shown in a typical $(\underline{r},\underline{\Omega})$ cell in Fig. 2.8. How they are related depends on the difference scheme adopted for the iterative solution. The $\alpha_{j,m}$ are coefficients describing angular distribution in curved space [corresponding to the geometrical area A_j in 2.34]. They will be defined and determined later on.

To obtain neutron balance in a finite cell, losses are equated to gains. The number of neutrons lost from flow through the face at r_j is the product of the average flux at r_j, the surface area normal to $\underline{r}$

and the solid angle. This gives $\omega_{\bar{m}}\mu_{\bar{m}}A_j N_{g,j,\bar{m}}$ where $\mu_{\bar{m}} = \cos\bar{\theta}$ is the vector product of $\underline{\Omega}_{\bar{m}}$ and the $\underline{r}$ direction. The net loss due to flow is therefore

$$\omega_{\bar{m}}\mu_{\bar{m}}\,(A_{j+1}N_{g,j+1,\bar{m}} - A_{j'}N_{g,j,\bar{m}})$$

To represent the loss due to angular redistribution in curved space we draw an analogy and say that the net number lost due to streaming through the angular faces can be written as

$$\alpha_{\bar{j},m+1}N_{g,\bar{j},m+1} - \alpha_{\bar{j},m}N_{g,\bar{j},m}$$

The loss due to collisions and absorptions (including time absorption) is

$$\omega_{\bar{m}}V_{\bar{j}}N_{g,\bar{j},\bar{m}}\,(\sigma^t_{g,\bar{j}} + \lambda/v_g)$$

where $\sigma^t_{g,\bar{j}}$ is the group- and space-cell averaged total *macroscopic* cross-section, v_g is the group average velocity and λ the time decay constant which is negative in a non-multiplying medium.

If now an average source $S_{g,\bar{j},\bar{m}}$ is defined exactly as the average flux in 2.34, we have the discrete form of the transport equation

$$\mu(A_{j+1}N_{j+1} - A_jN_j) + (\alpha_{m+1}N_{m+1} - \alpha_mN_m)/\omega\,) + V(\sigma^t+\lambda/v)N = VS \quad 2.37$$

where the averaged subscripts and g have been dropped for convenience. The term α/ω in 2.37 is present only in curved geometries and α represents angular redistribution of neutrons. Now the *net* angular redistribution must be zero if streaming is a conservative process and if therefore 2.37 is multiplied by ω and summed over all angles, the condition

$$\sum_{m=1}^{NN}(\alpha_{m+1}N_{m+1} - \alpha_mN_m) = \alpha_{NN+1}N_{NN+1} - \alpha_1N_1 = 0 \qquad 2.38$$

must be satisfied. Since in general N_{NN+1} and N_1 are non-zero, this

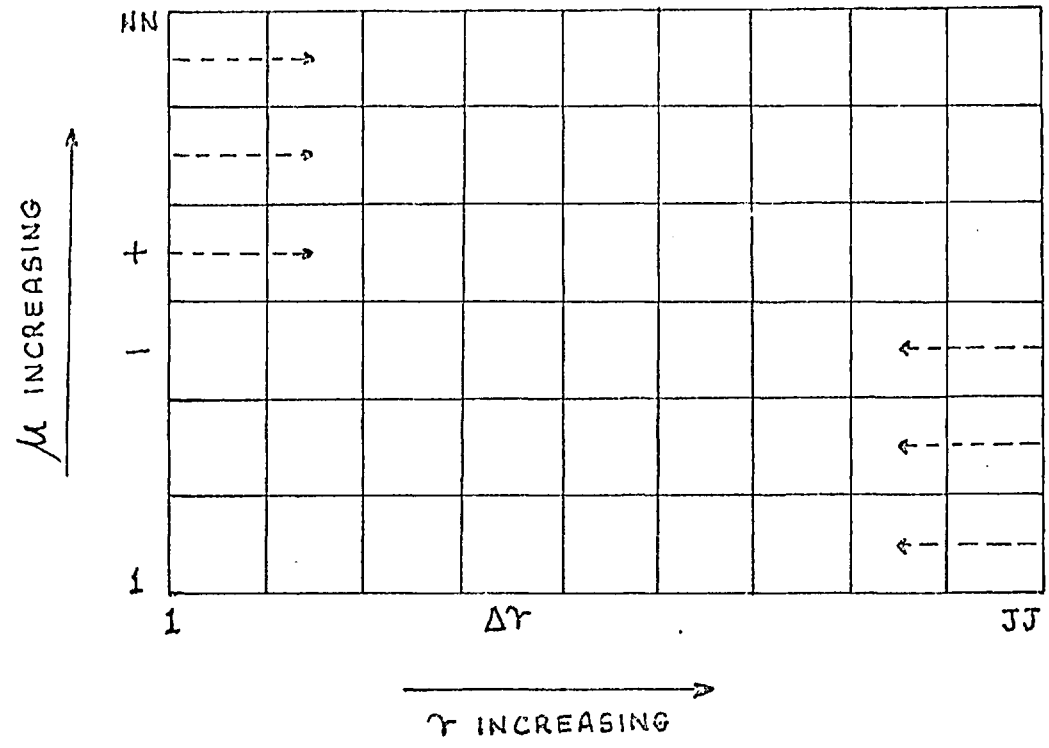


FIGURE 2.7 MESH REPRESENTATION FOR DISCRETE ANGLES AND SPACE POINTS

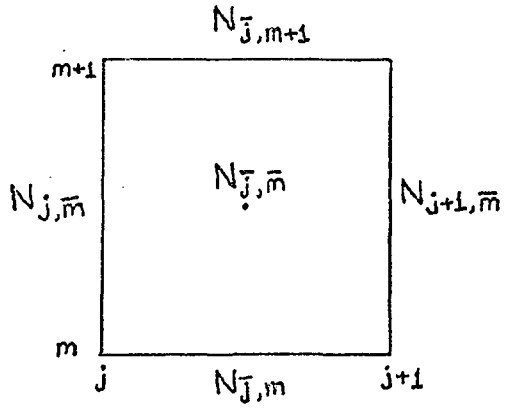


FIGURE 2.8 A TYPICAL ($\underline{r}$, $\underline{\Omega}$) CELL WITH THE AVERAGED ANGULAR FLUXES

implies that $\alpha_{NN+1} = \alpha_1 = 0$. This shows clearly that the first direction only transmits neutrons and the last only receives; in between there is ray-to-ray transfer. Consider the particular case where $V\sigma^t N = VS$ ($\lambda = 0$) and all the N's are equal, i.e. everywhere uniform flow. Under such conditions equation 2.37 yields

$$\alpha_{m+1} - \alpha_m = -\omega\mu(A_{j+1} - A_j) \qquad 2.39$$

which, with $\alpha_1 = 0$, defines the α's recursively. For plane geometry $A_{j+1} = A_j = 1$ for all j so that the α's are zero (no angular redistribution). Summing 2.39 over m and with $\alpha_1 = \alpha_{NN+1} = 0$ we see that the left-hand side vanishes so that

$$\sum_{m=1}^{NN} \omega_{\overline{m}}\, \mu_{\overline{m}} = 0 \qquad 2.40$$

This requirement indicates that the quadrature set chosen must have symmetric coefficients about $\mu = 0$ implying that $\mu = 0$ itself is not allowed as a direction.

If we let NN and JM both $\to \infty$, then for plane geometry, $\omega \to d\mu$; $V \to dx$ and $N_{j+1} \to N + dN/2$, $N_j \to N - dN/2$, whence equation 2.37 becomes the conservation form of the transport equation

$$\mu \frac{\partial N}{\partial x} + (\sigma^t + \lambda/v)N = S \qquad 2.41$$

The conservation forms in spherical and cylindrical geometry are also obtained by this approach of small intervals and has been detailed in LA3373. The α's defined by 2.39 therefore not only express neutron conservation but also reduce, in the limiting case, to the correct analytical form of the transport equation.

The source term S in 2.37 represents scattering collisions plus fissions and "fixed" sources which are independent of the fluxes. The latter two may not be present and are always assumed to be isotropic.

The fixed source is usually denoted by $Q_{g,\bar{j}}$ and the fission source given by

$$S^{f}_{g,\bar{j}} = \chi_g F_{\bar{j}} \qquad 2.42$$

where χ_g is the fission spectrum fraction in group g and $F_{\bar{j}}$ the total number of fission neutrons in Δr_j

$$F_{\bar{j}} = \sum_g \nu\sigma^{f}_{g,\bar{j}} \bar{N}_{g,\bar{j}} \qquad 2.43$$

$\bar{N}_{g,\bar{j}}$ is the group scalar flux in Δr_j and summed over the angles so that it is defined by

$$\bar{N}_{g,\bar{j}} = \int_\Omega N_g(\underline{r}_{\bar{j}},\underline{\Omega})\, d\Omega = \sum_{m=1}^{NN} \omega_{\bar{m}} N_{\bar{j},\bar{m}} \qquad 2.44$$

The current $\bar{I}_{g,\bar{j}}$ is correspondingly

$$\bar{I}_{g,\bar{j}} = \int_\Omega N_g(\underline{r}_{\bar{j}},\underline{\Omega})\, \Omega d\Omega = \sum_{m=1}^{NN} \omega_m \mu_m N_{\bar{j},\bar{m}} \qquad 2.45$$

The scattering term from 2.5 is

$$\int_{E'} \int_{\Omega'} \sigma^{s}(\underline{r},\underline{\Omega}'\to\underline{\Omega},E'\to E)\phi(\underline{r},\underline{\Omega}',E')\, dE'\, d\Omega'$$

The normal procedure is to expand the differential scattering cross-section in terms of Legendre polynomials

$$\sigma^{s}(\underline{r},\underline{\Omega}'\to\underline{\Omega},E'\to E') = \sum_{\ell=0}^{NC} \frac{2\ell+1}{4\pi} \sigma^{s\ell}(\underline{r},E'\to E)\, P_\ell(\underline{\Omega}'.\underline{\Omega}) \qquad 2.46$$

where NC is the order of anisotropy required.

In the case of plane and spherical geometry the addition theorem gives

$$P_\ell(\underline{\Omega}'.\underline{\Omega}) = P_\ell(\mu')P_\ell(\mu) \qquad 2.47$$

so that substitution for the scattering cross-section yields a collision source of the form

$$\sum_{\ell=0}^{NC} \frac{2\ell+1}{4\pi} P_\ell(\mu) \int_{E'} \sigma^{s\ell}(\underline{r},E'\to E) \int_0^{2\pi}\int_{-1}^{1} \phi(\underline{r},\underline{\mu}',E')P_\ell(\mu')\,d\mu'\,d\phi\,dE$$

which in discrete representation becomes

$$\sum_{\ell=0}^{NC} \frac{2\ell+1}{2} P_\ell(\mu_{\bar{m}}) \sum_{g'=1}^{IG} \sigma^{s\ell}_{g'\to g,\bar{j}} \sum_{m=1}^{NN} \omega_{\bar{m}'} P_\ell(\mu_{\bar{m}'}) N_{g',\bar{j},\bar{m}'} \qquad 2.48$$

Here $\sigma^{s}_{g'\to g,\bar{j}}$ is an appropriate group averaged macroscopic scattering cross-section anisotropic up to order NC. $P_\ell(\underline{\Omega}'.\underline{\Omega})$ in cylindrical geometry gives a more complex form and has been treated (LA 3373).

The choice of linear quadrature sets (μ and ω) to represent directional coordinates in discrete form is restricted by certain conditions, equation 2.40 being one of them and is in fact a symmetry condition. Thus the sets are reflective, i.e. if Ω is a direction in the set, so is the direction opposite to Ω. Two important conditions to be satisfied are

$$\sum_m \omega_{\bar{m}} = 1 \quad ; \qquad \sum_m \omega_{\bar{m}} \mu^2_{\bar{m}} = 1/3$$

The first merely represents solid angle normalization. The second is the diffusion theory condition and stems from the fact that in the trivial case of the quadrature order n = 2 the transport equation must become the diffusion equation. In the DSN this is arrived at by assuming that angular flux is related to the scalar flux and current by

$$N(\underline{r},\Omega) = N(r) + 3\mu I(r)$$

or

$$N_{\bar{j},\bar{m}} = \bar{N}_{\bar{j}} + 3\mu_{\bar{m}} \bar{I}_j \qquad 2.49$$

But

$$\bar{I}_{\bar{j}} = \sum_m \omega_{\bar{m}} \mu_{\bar{m}} N_{\bar{j},\bar{m}}$$

$$= \sum_m \omega_{\bar{m}} \mu_{\bar{m}} \bar{N}_{\bar{j}} + 3 \sum_m \omega_{\bar{m}} \mu^2_{\bar{m}} \bar{I}_j$$

so $$\bar{I}_j \{1 - 3 \sum_m \omega_m \mu_m^2\} = \sum_m \omega_m \mu_m \bar{N}_j$$

Now $\sum_m \omega_m \mu_m = 0$ and in general $\bar{I}_j \neq 0$; $\bar{N}_j \neq 0$.

This leaves $$\sum_m \omega_m \mu_m^2 = 1/3$$

In addition the "current" condition should also be satisfied. Consider the case of an *isotropic* flux of neutrons in the hemisphere next to a black region. The current into the absorber is

$$I_{in} = \sum_{\text{inwards}} \omega_m \mu_m N_m = N \Sigma \omega_m \mu_m$$

But the current is actually $I_{in} = \frac{1}{2} N$ so that it is advisable to have

$$\sum_m \omega_m |\mu_m| = 1/2$$

Although the first three conditions are in general correctly satisfied, certain quadrature sets give small errors when the last condition is applied, the errors diminishing as the order n increases. Carlson et al. have developed several sets for the discrete S_n method; in one-dimensional plane and spherical geometry this can also incorporate the P_{n-1} Method (Spherical Harmonics) and Double $P_{(n/2)-1}$ Method, both based on Gauss quadrature. The improved Brissenden quadrature sets developed at Winfrith is especially suitable for cylindrical geometry and satisfies the current condition well. For plane geometry the $DP_{(n/2)-1}$ set is recommended because it satisfies the current condition and because of the "bunching" of directions as $\mu \to 0$ so that the angular fluxes in the directions which are near normal to the neutron flow are more accurately described.

The $DP_{(n/2)-1}$ are related to the P_n by

$$P_n^+(\mu) = P_n(2\mu-1) \qquad 0 \leq \mu \leq 1$$
$$= 0 \qquad \mu < 0$$

$$P_n^-(\mu) = P_n(2\mu+1) \qquad -1 \leq \mu \leq 0$$
$$= 0 \qquad \mu > 0$$

In Gauss quadrature it turns out that the μ_m are the roots of the Legendre Polynomials of degree 2n+1 and the corresponding weights given by (MaCracken)

$$\omega_m = 2/[(1-\mu_m)(dP_n(\mu_m)/d\mu)^2]$$

Both the roots and weights are derived numerically and have been tabulated up to $DP_7 (= S_{16})$ in LA2595. For a given S_n of order n, there will be n, n+1 and n(n+4)/4 directions for plane, spherical and cylindrical geometry respectively. For the sphere there is one unweighted starting direction $\mu = -1$, and for the cylinder there are n/2 such directions, $\mu_m = -(1- \cos \theta_m)^{1/2}$ with $\theta_m = 0$ for each of the n/2 cos ω_m level (Fig. 2.6). These directions are necessary for initial flux calculations of curved space in the iterative procedure and will be shown to be so later on in the next chapter.

The discrete transport equation 2.37 is applicable only for one-dimensional geometry. However, in the case of a block, it is possible to account approximately for the two finite dimensions normal to the direction of neutron flow that is being solved. For plane geometry equation 2.37 becomes

$$\mu(N_{j+1} - N_j) + V\sigma^t N = VS \qquad 2.50$$

with the time dependence being dropped for the present. Multiplying 2.50 by ω_m and summing over m gives

$$\bar{T}_{j+1} - \bar{T}_j + V\sigma^t \bar{N}_j = VS \qquad 2.51$$

with the flux and currents defined by 2.44 and 2.45 respectively. Here S is assumed to be isotropic or corrected for first order only so that it is independent of angle. We further make the diffusion approximation, i.e. equation 2.49 holds and n = 2 with $\mu = \pm 1/\sqrt{3}$ and $\omega = 0.5$ for all quadrature sets which are applicable. If equation 2.49 is multiplied by $\bar{\omega}_m \bar{\mu}_m$ and summed over m then, under the assumed conditions, it becomes

$$\bar{N}_{j+1} - \bar{N}_j + 3V\sigma^t \bar{I}_j = 0 \qquad 2.52$$

Now should the actual flux shape be given by

$$\bar{N}_j = \phi \cos(\pi x_j/2a) \qquad 2.53$$

with $-a < x_j < a$, we find that as $\Delta x_j \to 0$ equation 2.52 will give

$$\bar{I}_j = -\frac{1}{3\sigma^t}\frac{\partial \bar{N}_j}{\partial x_j} = \frac{\pi}{6\sigma^t a}\phi \sin(\pi x_j/2a)$$

and the term $\bar{I}_{j+1} - \bar{I}_j$ in 2.51 will be $\partial \bar{I}_j$ so that

$$\frac{\partial \bar{I}_j}{\partial x_j} = \frac{V\pi^2}{12a^2\sigma^t}\phi\cos(\pi x_j/2a) = \frac{\pi^2\sigma^t}{12(a\sigma^t)^2} V\bar{N}_j \qquad 2.54$$

For each transverse leakage this so-called "buckling absorption" term is added in equation (2.37). Usually $a\sigma^t$ is replaced by $a\sigma^t + \lambda_{ext}$ where $\lambda_{ext} = 0.71044608$ is the extrapolated end point. Here $d_{ext} = 0.71044608/\sigma^t$. It should be noted here σ^t is the *total* cross-section and to first order anisotropy is replaced by $\sigma^{t,tr}$ which is the *total* transport cross-section and not the scattering transport cross-section $\sigma^{s,tr}$. This definition of λ_{ext} is peculiar to the DSN Method. For a block σ^t is replaced by an effective total cross-section.

$$\sigma^{t'} = \sigma^t \{1 + \frac{\pi^2}{3}\left(\frac{1}{(2a\sigma^t + 2\lambda_{ext})^2} + \frac{1}{(2b\sigma^t + 2\lambda_{ext})^2}\right)\}$$

where 2a and 2b are the transverse dimensions. It should be mentioned here that in the direction of neutron flow to be solved, no assumption of an extrapolated end point is made. The flux shape is determined entirely by the numerical procedure. $\pi^2/3$ is called the buckling factor.

Having defined and explained the coefficients and terms in the discrete transport equation 2.37 it now remains for it to be put into an appropriate algorithm for recursive solution. It is solved in terms of the neutron fluxes (the eigen functions) and if λ is present it becomes an eigenvalue which together with the fluxes is improved upon iteratively until convergence of both are obtained and neutron balance established. The method of solution will be detailed in the next chapter.

CHAPTER 3

THE ITERATIVE SOLUTION OF THE DISCRETE ORDINATES METHOD

3.1 THE DIFFERENCE EQUATIONS

Equation 2.37 is

$$\mu(A_{j+1}N_{j+1} - A_jN_j) + (\alpha_{m+1}N_{m+1} - \alpha_mN_m)/\omega + V(\sigma^t + \lambda/v)N = VS \qquad 3.1$$

It contains five unknowns: N_{j+1}, N_j, N_{m+1}, N_m and N. Two of these are known from the cell boundary conditions and therefore there is need to apply a suitable difference scheme to relate the fluxes in order to reduce the number of unknowns to the number of equations. Equation 3.1 is then converted into a basic recursion formula which is evaluated repeatedly subject to certain iterative procedures and evaluation rules.

A common and useful difference scheme termed the "diamond" difference scheme assumes that the flux within a cell is continuous and linear and that the unknowns are related by:

$$2N = N_{j+1} + N_j = N_{m+1} + N_m \qquad 3.2$$

For μ negative we substitute for N_j and N_{m+1} in 3.1 and obtain

$$N = \frac{-\mu_m A N_{j+1} + \alpha_m N_m + V(S + (\lambda/v)N)}{-2\mu A_i + 2\alpha_{m+1}/\omega_m + \sigma^t V} \qquad 3.3$$

with $A = (A_{j+1} + A_j)$

and $\alpha_m = (\alpha_{m+1} + \alpha_m)/\omega_m$ 3.4

Here λ is positive for a non-multiplying medium. Applying equation 3.4 twice for m+1; m and m, m-1 gives

$$\alpha_{\overline{m}} = [(\alpha_{m+1} - \alpha_{m-1}) + \alpha_{\overline{m-1}}\ \omega_{\overline{m-1}}]/\omega_{\overline{m}} \qquad 3.5$$

The same procedure applied to 2.39 yields

$$\alpha_{m+1} - \alpha_{m-1} = (A_j - A_{j+1})(\omega_{\overline{m}}\mu_{\overline{m}} - \omega_{\overline{m-1}}\mu_{\overline{m-1}})$$

Substituting this in 3.5 we have

$$\alpha_{\overline{m}} = [(A_j - A_{j+1})(\omega_{\overline{m}}\mu_{\overline{m}} - \omega_{\overline{m-1}}\mu_{\overline{m-1}}) + \omega_{\overline{m-1}}\alpha_{\overline{m-1}}]/\omega_{\overline{m}} \qquad 3.6$$

with $\alpha_1 = \omega_1 = 0$.

Equation 3.6 is in fact used to obtain the α's recursively on a computer. Combining 2.39 and 3.5, it is seen that

$$-2\mu_{\overline{m}}A_j + 2\alpha_{m+1}/\omega_{\overline{m}} = -\mu_{\overline{m}}A + \alpha_{\overline{m}}$$

so that a more elegant form of 3.3 is

$$N = \frac{-\mu_{\overline{m}}\, A\, N_{j+1} + \alpha_{\overline{m}} N_m + V(S + \lambda/vN)}{-\mu A + \alpha_{\overline{m}} + V\sigma^t} \qquad 3.7$$

It is to be noted that the time absorption term $(\lambda/v)N$ has been transferred over to the R.H.S. as a "source". The reason for this will become apparent when we come to the actual solution for λ. For μ positive (outgoing direction) a similar expression is obtained except that the negative signs become positive and N_{j+1} replaced by N_j. A general recursion formula for N can therefore be written as

$$N = \frac{|\mu_{\overline{m}}| AN' + \alpha_{\overline{m}} N_m + VS^{\lambda}}{|\mu_{\overline{m}}| A + \alpha_{\overline{m}} + V\sigma^t} \qquad 3.8$$

with $N' = N_{j+1}$ for $\mu_{\overline{m}} < 0$ and $N' = N_j$ for $\mu_{\overline{m}} > 0$ and $S^{\lambda} = S + (\lambda/v)N$. N is solved if N' and N_m are known and we get the fluxes for the next cell by using equation 3.2, viz.

$$\left.\begin{aligned} N_{m+1} &= 2N - N_m \\ N_j &= 2N - N_{j+1} \quad \text{or} \quad N_{j+1} = 2N - N_j \end{aligned}\right\} \qquad 3.9$$

Each $(\underline{r},\underline{\Omega})$ cell is scanned in turn beginning with the most negative μ and the outer boundary ($j = JJ$). It is advisable to integrate in the direction of neutron flow because this reduces the errors in the numerical process. Consider a flux of neutrons N_1 incident on a thin layer of material with a source distribution S. The emergent flux N_2 is

$$N_2 = \varepsilon N_1 + fS \qquad 3.10$$

where ε is an attenuation factor and f is the fraction of source neutrons escaping. Equation 3.10 follows the neutrons whereas if we integrate against the flow 3.10 will become

$$N_1 = (N_2 - fS)/\varepsilon$$

This involves subtraction and division both of which will amplify the errors on a computer.

Initially N' is known from boundary conditions

$N(x_{JJ},\mu) = 0, \quad \mu < 0$	zero incoming flux	right
$N(x_1,\mu) = 0, \quad \mu > 0$	" " "	left
$N(x_{JJ},-\mu) = N(x_{JJ},\mu)$	reflective	right
$N(x_1,+\mu) = N(x_1,-\mu)$	"	left

N_m, however, is not known initially and it has to be determined by the starting directions which have no weights ($\omega = 0$) and whose α's are zero. The initial starting equation is therefore simply

$$N = \frac{|\mu_1|A\, N_{j+1} + VS^{\lambda}}{|\mu_1|A + V\sigma^{t}} \qquad 3.11$$

and we set

$$N_{m+1} = N_m = N = (N_{j+1} + N_j)/2 \qquad 3.12$$

What this means is that there are no angular edges and the cell has "collapsed" into a line and hence $\omega_1 = 0$. For plane geometry such a starting direction is not necessary since there is no dependence on N_m.

3.2 INNER ITERATIONS

A complete scan through all angles (m = 1 to NN) and space intervals (j = 1 to JM) for each energy group comprises an inner iteration. The source S^λ depends on N through the self-scatter ($\sigma^s_{g\to g,\bar{j}}$), the fission source (if any) and, in our present problem, the time absorption $(\lambda/v)N$. Therefore, to construct S^λ initially we have to feed in guess scalar fluxes for each group. S^λ may also contain a flux independent term $Q_{g,\bar{j}}$. We can write S^λ as

$$S^\lambda = \sigma^s_{g\to g,\bar{j}} \bar{N}_{g,\bar{j}} + S' \qquad 3.13$$

where $\bar{N}_{g,\bar{j}}$ is the scalar flux defined previously. S' is to be regarded as "fixed" for each inner iteration and can only be recomputed after inner iteration convergence for all groups is satisfied. The self-scatter term will be modified after each inner iteration cycle, hence the need to split S^λ.

At the end of an inner iteration the neutron balance equation when summed over angles will be

$$A_{j+1}\bar{T}_{j+1} - A_j\bar{T}_j + V(\sigma^r + \sigma^s_{g\to g})\bar{N} = V(\sigma^s_{g\to g}\bar{N}^p + S') \qquad 3.14$$

where the removal cross-section $\sigma^r = \sigma^t - \sigma^s_{g\to g}$. $\bar{N}^p$ is the scalar flux from a previous iteration and initially will of course be the guess flux. Equation 3.14 as it stands is balanced mathematically but is

not very meaningful physically since $\overline{N}$ is not equal to $\overline{N}^p$. As iteration proceeds $\overline{N}^p$ will approach $\overline{N}$ and in order to accelerate convergence, the fluxes are scaled in the following way: Multiplying equation 3.14 by a factor f_{in}, adding $(f_{in}\sigma^s_{g\to g}\overline{N} - f_{in}\sigma^s_{g\to g}\overline{N})$ and $(S'-S')$ to the R.H.S. and rearranging terms gives

$$f_{in}[A_{j+1}\overline{T}_{j+1} - A_j\overline{T}_j + V(\sigma^r + \sigma^s_{g\to g})\overline{N}] = V[f_{in}\sigma^s_{g\to g}\overline{N} + S']$$

$$+ \underline{V[f_{in} - 1]S' + f_{in}V\sigma^s_{g\to g}(\overline{N}^p - \overline{N})} \qquad 3.15$$

Equation 3.15 would give an exact physical balance for a flux level $f_{in}\overline{N}$ if and only if the underlined expression vanishes. Now f_{in} is merely a constant and the other quantities depend on j, so the best thing to do is to say that this expression does vanish on the whole when equation 3.15 is summed over j. This then provides a definition for f_{in} which is

$$f_{in} = \sum_j VS' / \{[\sum_j VS' + V\sigma^s_{g\to g}(\overline{N}^p - \overline{N})]\} \qquad 3.16$$

All fluxes are scaled by this factor f_{in} after each inner iteration and as $\overline{N}^p \to \overline{N}$, $f_{in} \to 1$. S' is regarded as fixed and is not to be scaled. It is assumed to be *always non-zero*. In a one-group calculation with no fissions and no independent source S' is in fact zero. However if there is time dependence, the time absorption term $(\lambda/v)\overline{N}$ can be transferred over to the R.H.S. of the balance equation so that $S' = (\lambda/v)\overline{N}$ and is therefore non-zero. This is exactly the case with the present problem.

Iteration can be terminated when a point-wise convergence criterion ε_x is satisfied, i.e.

$$\max_j \left| \frac{\overline{N}_j - \overline{N}^p_j}{\overline{N}^p_j} \right| < \varepsilon_x \qquad 3.17a$$

Another criterion is to compute "false" sources such as

$$\varepsilon_2 = \sum_j V_o \sigma^s_{g\to g,\bar{j}} \left|\bar{N}_{\bar{j}} - \bar{N}^p_{\bar{j}}\right|$$

or $$\varepsilon_3 = \sum_j V(\sigma^t_{\bar{j}} - \sigma^s_{g\to g,\bar{j}}) \left|\bar{N}_{\bar{j}} - \bar{N}^p_{\bar{j}}\right| \quad \text{if } \sigma^s_{g\to g,\bar{j}} \text{ is small and}$$

require that these be less than a small fraction of the true source, e.g.

$$\varepsilon_2 \text{ or } \varepsilon_3 < \varepsilon \sum_j V \{ \sum_g (Q_{g,\bar{j}} + \chi_g F_{g,\bar{j}}) \} = \varepsilon_t \qquad 3.17b$$

where ε is very small.

If in a problem the boundaries are reflective there is need for further adjustment to the fluxes at the right boundary. At the left boundary the outgoing fluxes are merely set equal to the incoming fluxes (specular reflection). Thus

$$N(x_1,\mu) = N(x_1,-\mu)$$

However as the sweep continues to the right boundary there is no guarantee at all that the latest right boundary fluxes $N(x_{JJ},\mu)$ will be equal to the old inward fluxes $N(x_{JJ},-\mu)$ with which the sweep is started. We set $N'(x_{JJ},-\mu) = N(x_{JJ},\mu)$ and start another iteration obtaining $N'(x_{JJ},\mu)$. These N' are stored with the current $I'_{JJ} = \sum_m \omega_{\bar{m}} \mu_{\bar{m}} N'(x_{JJ},\mu_{\bar{m}})$.

Now we let $N''(x_{JJ},-\mu) = N'(x_{JJ},\mu)$ and with $S^\lambda = 0$ perform yet another iteration obtaining $N''(x_{JJ},\mu)$ with the corresponding current $I''_{JJ} = \sum_m \omega_{\bar{m}} \mu_{\bar{m}} N'(x_{JJ},\mu_{\bar{m}})$. The resultant current must be zero for reflection. $I'_{JJ} + I''_{JJ}$ may not be zero but we can always scale I''_{JJ} by a factor f_b such that

$$I'_{JJ} + f_b I''_{JJ} = 0$$

giving $$f_b = -I'_{JJ}/I''_{JJ} \qquad 3.18$$

f_b is therefore the boundary scale factor needed to effect the correct reflective condition. This so-called implicit boundary scaling (if necessary) is carried out before the inner iteration scaling.

In equation 3.8 the coefficients, σ^t, S^λ and V are all positive so that N will always be positive provided N' and N_m are positive. However it may happen that the extrapolations $N_j = 2N - N_{j+1}$ (or $N_{j+1} = 2N - N_j$) and $N_{m+1} = 2N - N_m$ will yield negative values of N' and/or N_{m+1} for calculation in the next cell. This is undesirable as they may cause oscillations and produce negative N which is physically meaningless. Rather than let the fluxes go negative, the "offenders" are set to zero in the balance equation 3.1 and a correct recursive formula is set up so as not to upset neutron balance. As an example, suppose in slab geometry $N_j = 2N - N_{j+1}$ becomes negative. $N_j = 0$ in equation 3.1 so that the correct recursive formula to use is

$$N = [|\mu| A_{j+1} N_{j+1} + VS^\lambda] / V\sigma^t \qquad 3.19$$

3.3 OUTER ITERATIONS

For each group, starting with the highest energy g = 1 down to g = IG, a series of inner iterations are performed until convergence of the fluxes is achieved. The total result is called an outer iteration. The downscatter part of the source is always recomputed from the latest converged fluxes as we proceed down the groups so that if there are no fissions, upscatter or other flux-dependent sources (i.e. only an independent fixed source Q_g is present) the first outer iteration is also the final solution. In the present problem the source is $(\lambda/v)\overline{N}_j$. It depends on λ and $\overline{N}_j$, both of which are initially guessed so that we have to improve on them by a series of outer iterations to get convergence.

Let λ^o and $\overline{N}_j^o$ be the guess values. Prior to the first outer iteration we have the unequal expression

$$\sum_j [A_{j+1} I_{j+1}^o - A_j I_j^o + V\sigma^r \overline{N}_j^o] \neq \sum_j (\lambda^o/v)\, \overline{N}_j^p \qquad 3.20$$

A series of inner iterations is now performed until the converged fluxes $\overline{N}_j$ are obtained, remembering that $(\lambda^o/v)\overline{N}_j^o$ is fixed. Thus after one outer iteration we have the formal balance equation

$$\sum_j [A_{j+1} I_{j+1}' - A_j I_j' + V\sigma^r \overline{N}_j'] = \sum_j (\lambda^o/v)\, \overline{N}_j^o \qquad 3.21$$

which does not exhibit true physical balance since λ^o is a guess value and $\overline{N}_j^o$ is not necessarily equal to $\overline{N}_j$. Now it is possible to write an equation

$$\sum_j [(A_{j+1} I_{j+1}' - A_j I_j') + L_j + V\sigma^r \overline{N}_j'] = \sum_j (\lambda'/v)\, \overline{N}_j' \qquad 3.22$$

If L_j is made to vanish somehow, we see that 3.22 is nearer the exact balance equation although it is not quite the latter since λ' may not be the true eigenvalue. Subtracting 3.21 from 3.22 gives us an expression for L_j which is

$$L_j = (\lambda'/v)\, \overline{N}_j' - \lambda^o/v\, \overline{N}_j^o \qquad 3.23$$

L_j can be regarded as a leakage term caused by the "incorrect" decay of the "false" source neutrons. By summing over j we force it to vanish on the whole.

$$\sum_j L_j = (\lambda'/v)\, \overline{N}' - (\lambda^o/v)\, \overline{N}^o = 0 \qquad 3.24$$

where the fluxes are now the total fluxes.

Let $$P' = \overline{N}'/\overline{N}^o \qquad 3.25$$

then $$\overline{N}^o/v[P'\lambda' - \lambda^o] = 0$$

giving $\lambda' = \lambda^o/P'$ 3.26

since $\overline{N}^o/v$ is non-zero. The improved eigenvalue λ' is to be fed into another series of inner iterations to give a second outer iteration at the end of which λ^2 is computed. Before performing this second cycle the flux density $\overline{N}'/v$ must be reset to the initial density, i.e. $\overline{N}^o/v$ where $\overline{N}^o$ is fixed and may be normalised; this is effected by scaling with $1/P'$. This means that we always start a decay calculation with the same number of neutrons in the system which must be so since we are merely trying to find the right decay for this given density.

We see then that the inner iterations are responsible for establishing the flux shape with respect to a fixed source level sent in from the outer iteration. Although inner convergence is effected, the total flux level at the end may not be the same as before since the λ in the source may not be the true value. Therefore there is need to improve λ by a series of outer iterations with the flux level being scaled up to the same value for each iteration. For the n^{th} outer iteration we have

$$P^n = \overline{N}^n/\overline{N}^o \qquad 3.27$$

$$\lambda^n = \lambda^{n-1}/P^n = \lambda^o/(P^n P^{n-1} \ldots P^1) \qquad 3.28$$

As $\overline{N}^n \to \overline{N}^o$, $P^n \to 1$ and $\lambda^n \to \lambda^{true}$. Thus, provided the fluxes do not differ by wild orders of magnitude P^n will always be a reasonable parameter with which to scale λ^{n-1} and by forcing neutron balance at the end of each outer iteration stable convergence is effected. Iteration is terminated when $|P^n - 1| < \varepsilon_p$ where ε_p is a specified convergence criterion. Outer iteration scaling for fissions, upscatter and other types of eigenvalue problems will not be discussed here since they bear no relevance to the present problem.

3.4 ERRORS AND LIMITATIONS

The above method for obtaining the time decay λ is limited to one-dimensional geometry and monoenergetic neutrons. As has been mentioned before "buckling absorption" terms can be derived to account for the finite transverse dimensions in a block. This is correct up to B_g^2 only so that the decay obtained numerically is not expected to be much more accurate than that obtained by expansion up to B_g^2. However it must be emphasised that, in the direction to be solved, no assumption of a flux distribution or of an extrapolated end point is made. The flux shape is determined purely by the iterative procedure. This is certainly a break from the conventional expansion method.

The diamond difference extrapolation relations equation 3.9 are of course not exact. This means that the separate terms in the balance equation 3.1, although retaining their physical meaning, are in fact approximated. As the number of directions and space intervals are increased the relations will become more accurate. By using a recursive equation such as 3.8 errors in a cell will be propagated throughout the entire mesh so that they are systematic (cf. random errors, e.g. in Monte Carlo methods). The quadrature set to be used should satisfy the various conditions mentioned and the order n should be sufficiently large so as not to lose too much detail on angular fluxes. Use of wide space intervals encourage negative fluxes especially if the latter vary considerably from cell to cell. Assuming that a reasonable mesh of cells is established in which the above errors are minimised another parameter which will affect the accuracy of λ is the input cross-section. In particular the sensitivity of λ to changes in the σ^{ne}, the non-elastic cross-section, (with σ^t constant) will be tested. The dependence of λ on σ^{ne} is implicit through the solution of the transport equation itself (cf. expansion method where the dependence is explicit).

3.5 THE DISCORD PROGRAMME

A computer programme DISCORD (Discrete Ordinates) has been written in Fortran IV by the author to solve the transport equation and obtain λ. It is based on the Los Alamos DTF IV code for solving the one-mensional multigroup transport equation with anisotropic scattering but has been adapted and modified according to the foregoing discussions. DTF IV does not make a provision for determining λ in a non-multiplying medium; it always assumes the presence of a fission source in a homogeneous problem (no independent source). Another difference is the addition in DISCORD of a subroutine WEIGHT which calculates a quadrature set due to Carlson (8) and also a set due to Brissenden (1) for cylindrical calculations. If anisotropic scattering is used the appropriate Legendre polynomials for slab and sphere only are generated in this subroutine. The subroutine ALPHA constructs the time absorption source $(\lambda/v)\overline{N}$ and then scales λ and N as shown previously. An iteration monitor has been established in the print-out to show the convergence pattern of λ and the parameter P. Group scalar fluxes and angular fluxes (if desired) are also printed out. Neutron balance, leakages, absorption etc. are indicated. Input quantities such as cross-sections, radii, angles and weights are checked before actual calculation proceeds. DISCORD allows for a whole series of problems to be solved in one run be they distinct individual problems or sub-problems in which either the space intervals, the quadrature order or both are changed. A typical decay calculation for an iron block with 30 space intervals, S_{16} and first order anisotropy takes 0.23 minutes. A convergence tolerance of $\varepsilon_p = 0.00001$ can be achieved with a total of 125 inner iterations and 11 outer iterations. λ is strongly modified by the first three outer iterations. After that it tends to

converge rather monotonically. Of course if the guess value of λ is near to the actual value and the flux guess is of the correct shape 3 or 4 iterations will suffice. Fig. 3.1 shows the flow diagram for DISCORD.

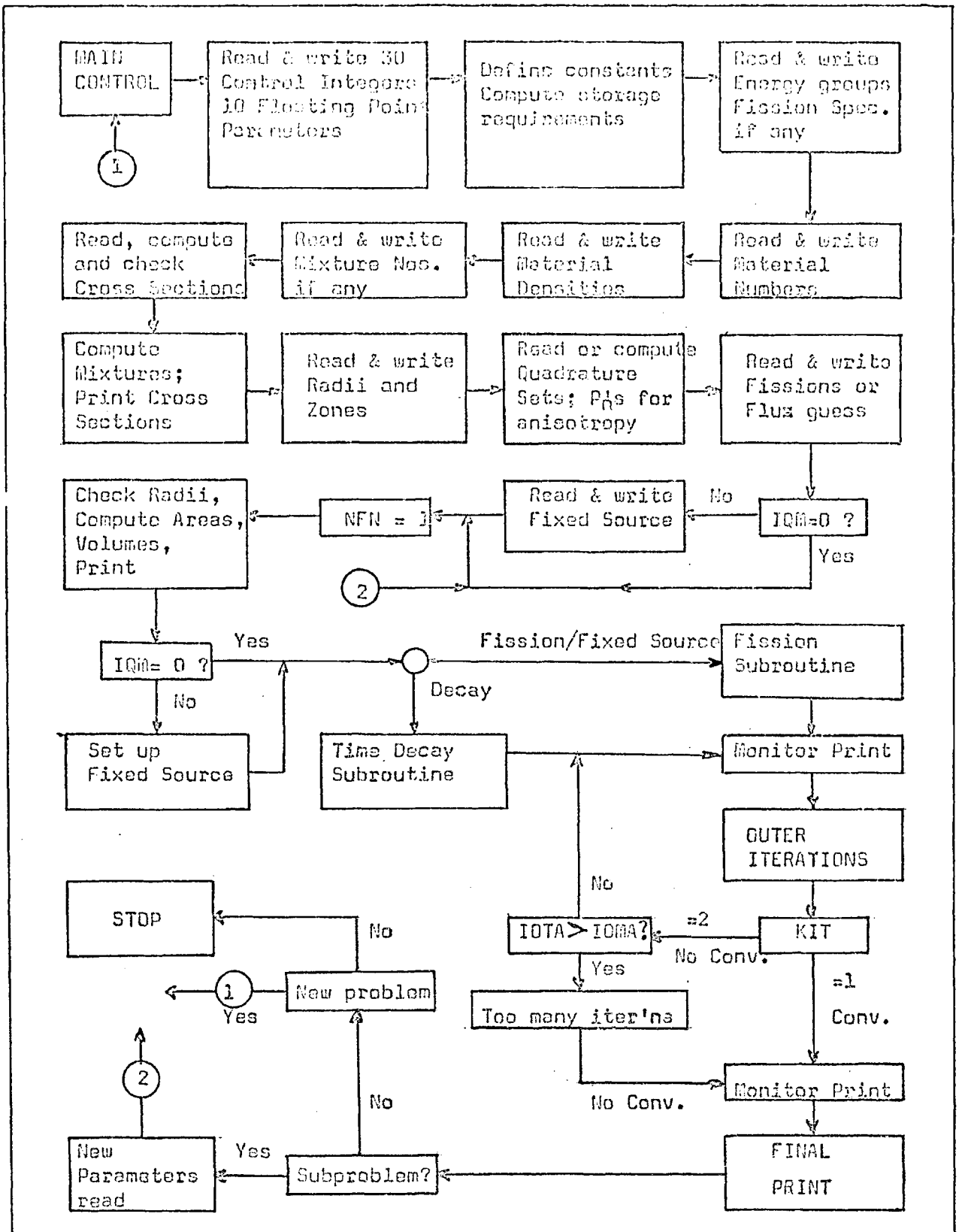


FIGURE 3.1 FLOW DIAGRAM FOR THE COMPUTER PROGRAMME 'DISCORD'

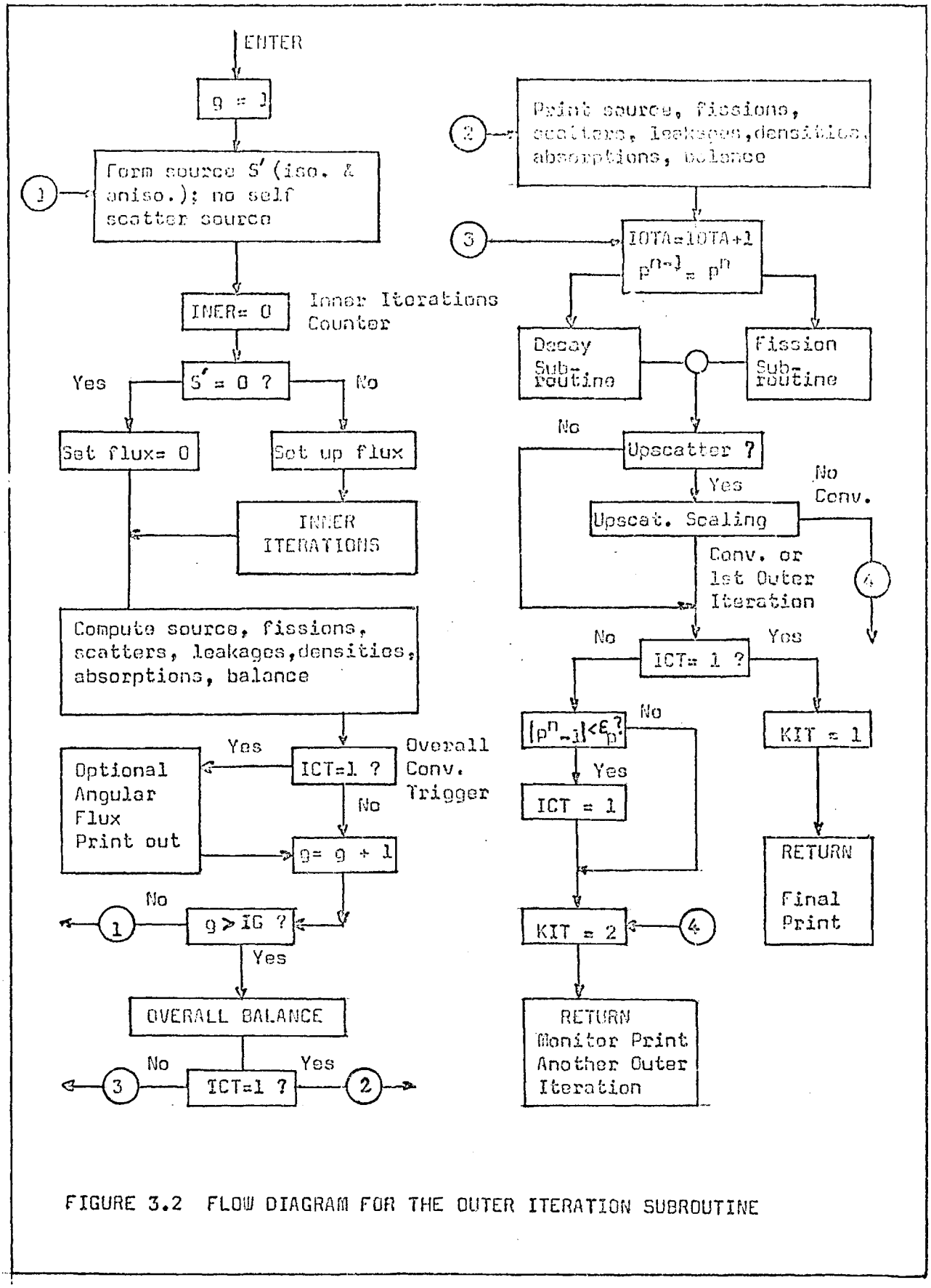


FIGURE 3.2 FLOW DIAGRAM FOR THE OUTER ITERATION SUBROUTINE

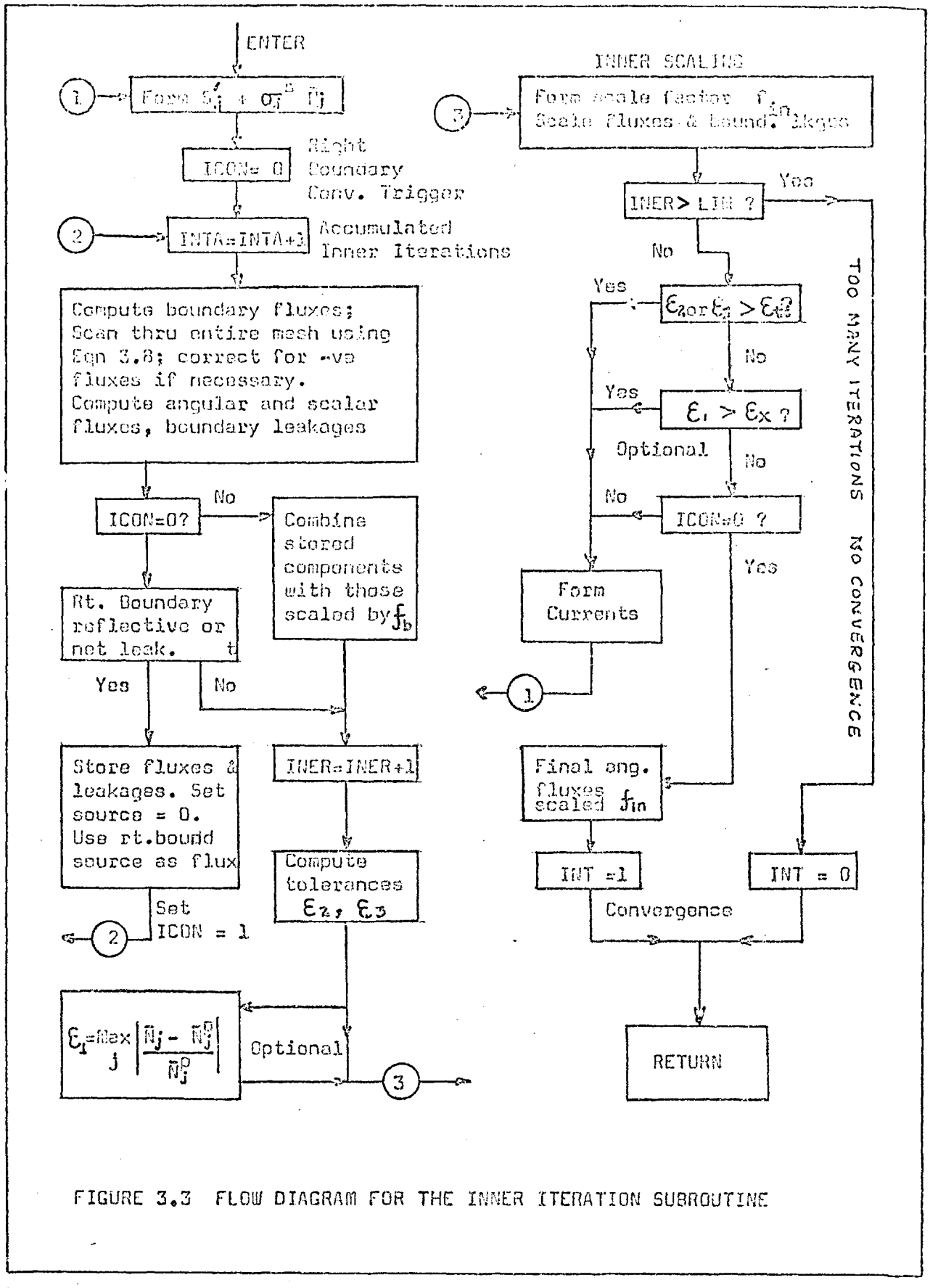


FIGURE 3.3 FLOW DIAGRAM FOR THE INNER ITERATION SUBROUTINE

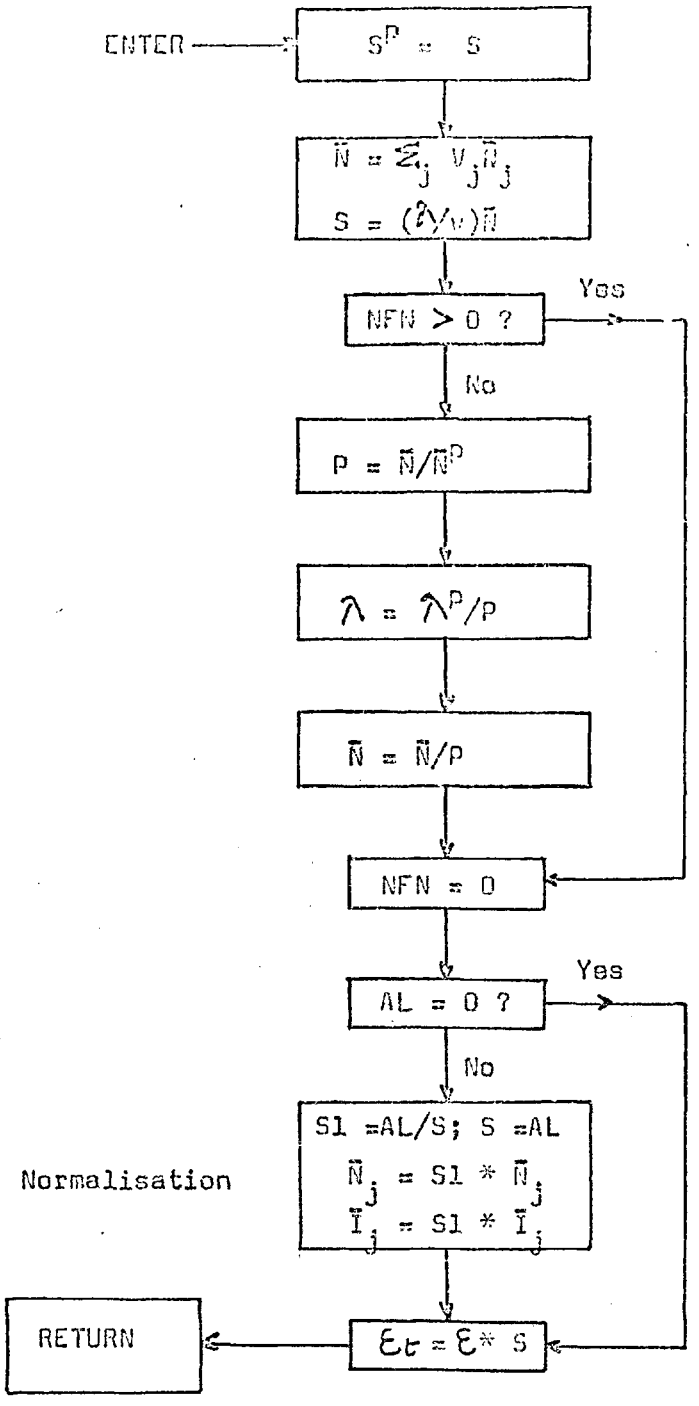


FIGURE 3.4 FLOW DIAGRAM FOR THE DECAY SUBROUTINE

CHAPTER 4

THE VELOCITY OF LIGHT EXPERIMENT

The object of this experiment was twofold:-

a) To test the time resolution of the detector and associated electronics of the fast coincidence circuitry which were later to be used to measure the decay of pulsed fast neutrons.

b) To test the linearity of the Time to Amplitude Converter - Multichannel Pulse Height Analyser (T.A.C. - M.C.P.H.A.) combination and to calibrate the latter in terms of the time-of-flight of gamma rays, i.e., the velocity of light.

4.1 PRINCIPLE OF THE EXPERIMENT

Suppose two gamma rays γ_1 and γ_2 are emitted from a source in exactly opposite direction. γ_1 is detected and analysed by channel 1 and γ_2 by channel 2 of the circuit as shown in Figure 4.1, the two detectors being placed in line with the source in between. The pulses resulting from γ_1 are made to actuate the Time to Amplitude Converter (T.A.C.) which will start to charge up a capacitive component until stopped by a pulse from channel 2. The capacitor then discharges to give an output pulse whose height will be proportional to the time delay between the start and stop pulses. The output pulse is fed, after suitable amplification, into the analyser which will register events in the entire conversion range of the T.A.C. Those events due to the two gammas will be strongly correlated and will give rise to a prompt time coincidence spectrum which should roughly be Guassian in shape provided the operating characteristics of both channels are similar. The full

width at half maximum (F.W.H.M.) will therefore give a measure of the time resolution of the circuitry. The uncorrelated events will be registered as random background.

Let d_1 = distance of detector 1 from the source (cms)

d_2 = " " " 2 " " " "

ΔT_1 = delay (inherent and inserted) in channel 1 (ns)

ΔT_2 = " " " " " " 2 "

The difference in time-of-flight of γ_1 and γ_2 will be

$$\tau = \frac{1}{C}(d_2 - d_1) = \frac{d}{C} \quad . \qquad 4.1$$

where C is the velocity of light (cms/sec).

The actual delay registered by the analyzer as a pulse height will be

$$\frac{d}{C} + \Delta T_2 - \Delta T_1 \quad \text{nanoseconds}$$

and the peak of the spectrum will fall in channel N_p. If detector 2 is moved to a new position along the line joining the two detectors and the source, keeping detector 1 fixed, then there will be a corresponding shift in the position of the peak along the analyzer. Let the channel width be λ nanoseconds. If the circuitry is linear then the following relationship in time should hold.

$$\lambda N_p = \frac{d}{C} + \Delta T_2 - \Delta T_1$$

$$N_p = \{\frac{1}{\lambda C}\}\, d + \frac{\Delta T}{\lambda} \qquad 4.2$$

A graph of channel number N_p against distance moved d (cms) should give a straight line whose slope will yield λ if the velocity of light is assumed known. The intercept on the N_p axis will give the difference in delay between the two channels.

4.2 TIME RESOLUTION CONSIDERATION

Since fast neutrons with lifetimes in the tens of nanosecond range or less were to be measured the time resolution of the detecting system must be in the nanosecond range or less. In this section the factors contributing to the time width are discussed.

Suppose a particle of energy E_o (MeV) enters and interacts with a suitable detector (e.g. a plastic phosphor coupled to a photomultiplier) in a time τ_E, leading to the excitation of optically active states. In the case of the particle being a gamma ray, the interaction will be due to the Compton effect whereby the γ ray deposits energy from zero up to the Compton edge E_c given by

$$E_c = \frac{E_o}{(1 + m_e C^2/2E_o)} \qquad 4.3$$

with $m_e C^2 = 0.511$ MeV, the electron rest mass.

If the particle is a neutron, then the energy transfer is effected through the proton recoil process in which the ideal knock-on proton has a rectangular probability distribution

$$P(E_p)\, dE_p = \frac{dE_p}{E_o} ; \quad E_p < E_o \qquad 4.4$$

$$= 0 \quad ; \quad E_p > E_o$$

(The energy resolution in both cases will not be discussed here.)

The excited states will decay with a finite time constant τ_o, emitting P photons of mean energy E_1. These will strike the photocathode of the photomultiplier (PMX) in time τ_p, producing R electrons where

$$R = \varepsilon_o \varepsilon_q P \qquad 4.5$$

ε_o is the optical transmission efficiency and ε_q the quantum efficiency. Defining the collection efficiency of the first dynode

$$\varepsilon_c = R_o/R \qquad 4.6$$

R_o photoelectrons will reach the first dynode from various parts of the cathode surface. They are accelerated down the tube to form a cascade which after a transit time, τ_{ph}, arrives at the anode and forms a pulse with a current given empirically by (Mullard Handbook)

$$I_a = -\frac{Q}{\tau_o} e^{-t/\tau_o} \qquad 4.7$$

with the total charge $Q = I_{a_{max}} \tau_o$.

The voltage pulse behaves according to

$$V(t) = -\frac{Q}{C_a} \frac{\tau_1}{\tau_o - \tau_1} [e^{-t/\tau_o} - e^{-t/\tau_1}] \qquad 4.8$$

with the time constant of the anode circuit $\tau_1 = C_a R_a$ where C_a is the anode stray capacitance and R_a is the anode load.

The leading edge which is used to trigger a fixed threshold of a fast discriminator has a rise time τ_r obtained by differentiating equation 4.8.

$$\tau_r = [\frac{\tau_1 \tau_o}{\tau_1 - \tau_o}] \ln \tau_1/\tau_o \qquad 4.9$$

This timing edge has a finite width resolution and from the above discussion this width is brought about by variations in

a) τ_E, the interaction time and E_1 the mean energy of the photons.

b) τ_o, the phosphor decay constant.

c) τ_p, the time of photon arrival at the cathode.

d) τ_{ph}, the transit time for the electron cascade due to (i) different starting points and (ii) different initial energy and angle of secondary electrons.

e) the triggering time of the discriminator.

In the case of small phosphors and for gamma rays and fast neutrons τ_E is negligible and so is τ_p unless a very long light guide is intro-

is introduced. Variations of (b), (d) and (e) will give rise to time dispersions known as "jitter" and "walk". Jitter is created by electronic noise and fluctuations in the time of arrival of the electronic cascade responsible for the pulse. Walk is the shift in time caused by fixing a threshold level with amplitude (i.e. energy) and rise time varying. In particular jitter in (e) is termed the "slewing time". The various time dispersions are illustrated in Fig. 4.2.

The effects of finite phosphor decay, transit time spread and "slewing time" are now considered and an estimate is made of the magnitude of the resolution. For argument sake we put $\varepsilon_o = \varepsilon_q = 1$ so that $R = P$ in equation 4.5. The number of photoelectrons collected after a time t will be

$$n = R[1 - e^{-t/\tau_o}]$$

$$\simeq [R/\tau_o]t \qquad t << \tau. \qquad 4.10$$

R/τ_o is the initial rate of photoelectron pulses so that the R.M.S. deviation in the time of emission of the first photoelectron is τ_o/R. The R.M.S. deviation in the time of emission of the n^{th} electron is

$$\varepsilon_n = \sqrt{\frac{\sum_{i=1}^{n} <\delta t_i>^2}{n}} \qquad 4.11$$

If $t << \tau_o$ and $n << R$, then $\delta t_1 = \delta t_2 = \delta t_3 = \ldots$

so that

$$\varepsilon_n = [\tau_o/R]\, n^{1/2} \qquad 4.12$$

In fact a rigorous calculation by Post and Schiff which holds for all values of n and R yields

$$\varepsilon_n = (\tau_o/R)\, n^{1/2}\, [1 + 2(n+1)/R + \ldots]^{1/2} \qquad 4.13$$

Both equations 4.12 and 4.13 show that ε_n is minimised by having τ_o small (fast decay), R large (good energy, optical and quantum efficiencies) and n small (triggering on the first few photoelectrons).

For the circuit to trigger on the first few photoelectrons a high gain is needed as the following simple argument shows:

Output voltage pulse	V_a	=	2 volts
Anode stray capacitance	C_a	=	.60 pF
Output charge	$Q = C_a V_a$	=	1.2×10^{-10} Coulomb
Number of electrons required		=	$\frac{1.2 \times 10^{-10}}{1.6 \times 10^{-19}}$
		≃	7.5×10^8
Number of initial photoelectrons	n	=	5
Therefore gain required	G	=	1.5×10^8

The effect of the spread in transit time of the electron cascade down the tube is now included. The R.M.S. deviation in the transit time (defined as the start of one photoelectron at the cathode to the arrival at the anode of half the total number of electrons) is shown by Gatti and Svelto to be

$$\varepsilon_{ph} = \sqrt{\varepsilon_{cd}^2 + \varepsilon_{dd}^2 /(g-1)} \qquad 4.14$$

where ε_{cd} is the cathode to first dynode standard deviation; ε_{dd} is the interdynode time spread and $1/(g-1)$ is the variance in the multiplication factor.

The total R.M.S. variation in the time of arrival of the n^{th} electon at the anode is

$$\sigma_n = \sqrt{(\varepsilon_{ph}^2/n + n(\tau/R)^2)} \qquad 4.15$$

The spread in the variance σ_n^2 is assumed to be approximately Gaussian in shape so that equation 4.15 is actually a worst case, i.e.

we are working on the skirt of the Gaussian distribution which is 3σ away from the mean. If therefore the circuit responds to the *average* time of arrival of the first n photoelectrons rather than on the n^{th} electron precisely, we have

$$\sigma_{\overline{n}} = \sigma_n/\sqrt{3} \qquad 4.16$$

If $\sigma_{\overline{n}}$ is minimised with respect to n we find

$$n/R = \varepsilon_{ph}/\tau_o \qquad 4.17$$

as the condition for minimum time resolution. If σ_s is the "slewing time" uncertainty in the discriminator, then the overall time resolution of the detector will be

$$\sigma_p = \sqrt{(\sigma_{\overline{n}}^2 + \sigma_s^2)} \qquad 4.18$$

With two detectors the prompt time coincidence spectrum will be roughly Guassian in shape with standard deviation

$$\sigma_G = \sigma_p/\sqrt{2} \qquad \text{if} \qquad \sigma_{p_1} = \sigma_{p_2} = \sigma_p$$

The F.W.H.M. is

$$\omega_{1/2} = 2\sigma_G \sqrt{(2 \ln 2)}$$

$$= 2.36\, \sigma_G \qquad 4.19$$

For a typical fast plastic phosphor, e.g. NE 104 (Nuclear Enterprises)

$$R \simeq 75 \qquad \tau_o = 2\text{ns} \quad \text{and} \quad n = 5 \text{ (assumed)}$$

and for the photomultiplier 56 AVP (Mullard)

$$\varepsilon_{ph} = 0.5 \text{ ns}$$

This gives

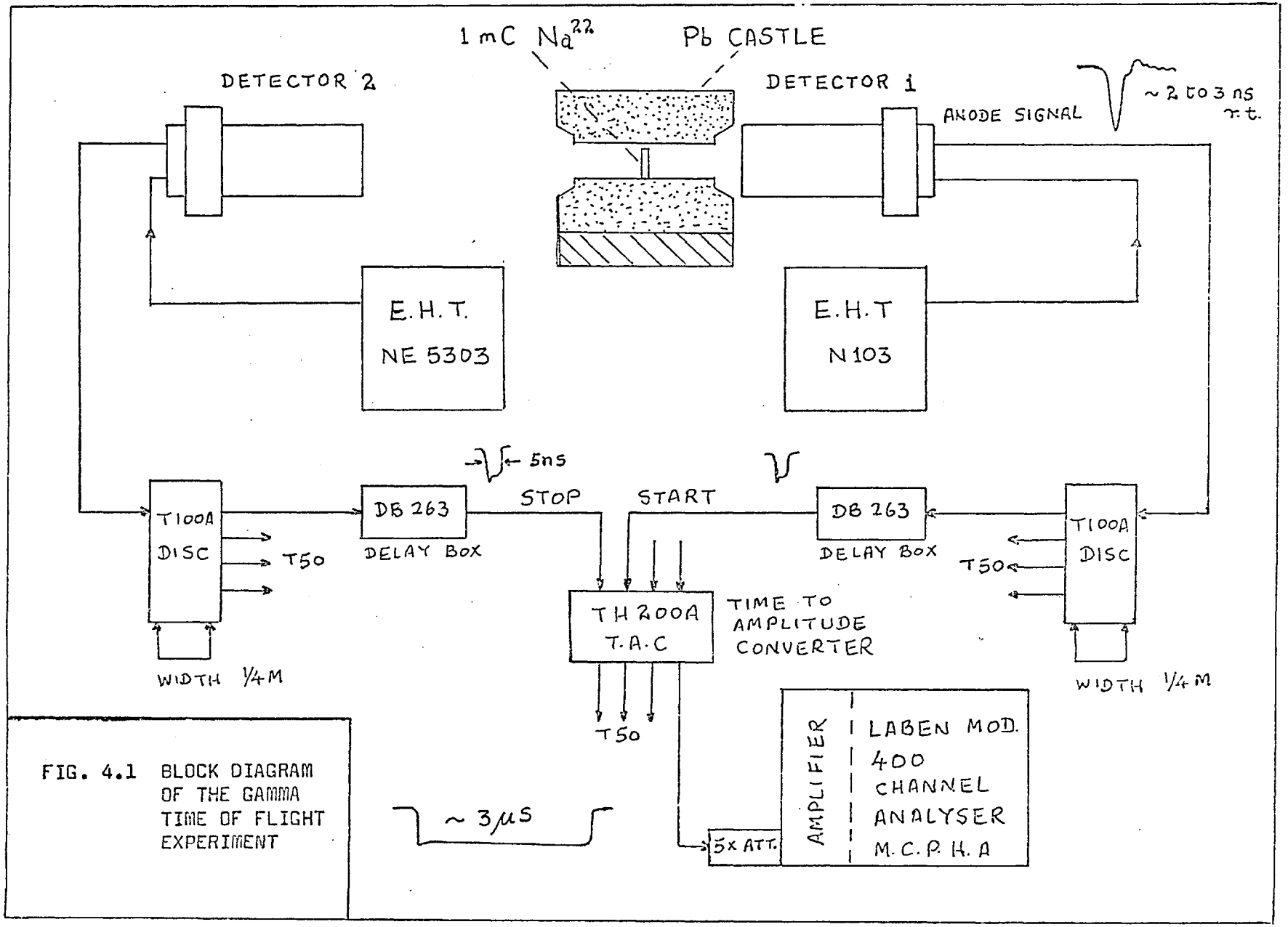
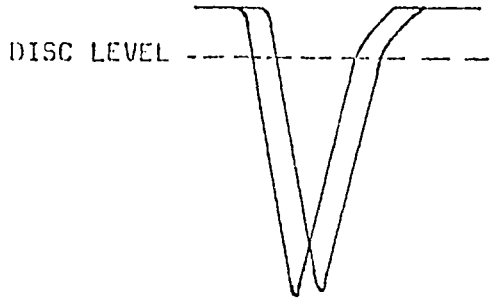
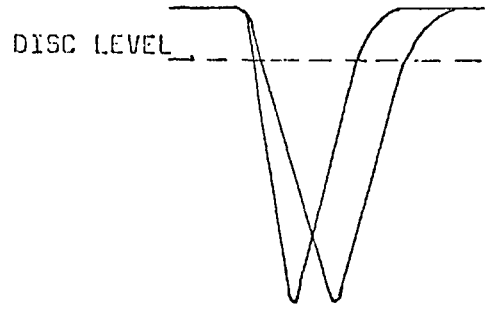


FIG. 4.1 BLOCK DIAGRAM OF THE GAMMA TIME OF FLIGHT EXPERIMENT

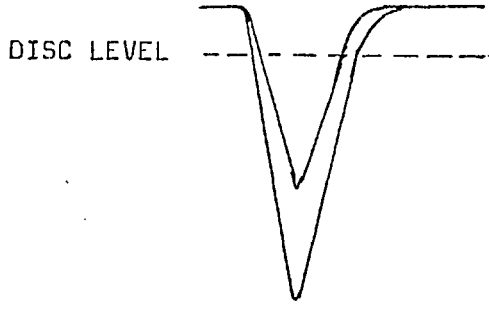


A Jitter of the leading edge.

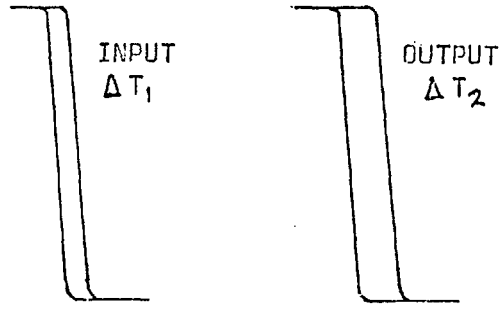
Pulses have the same rise time and amplitude.



B Walk due to pulses having the same amplitude but different rise times.

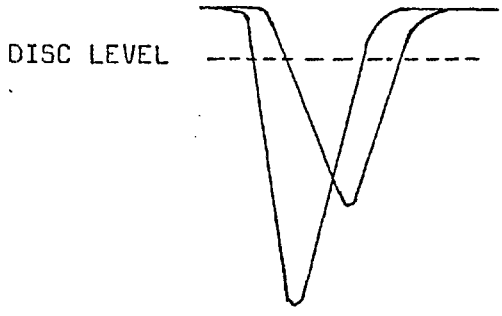


C Walk due to pulses having the same rise time but different amplitudes.



D Discriminator jitter.

'Slewing Time' = $\Delta T_2 - \Delta T_1$



E Combined effects of A B & C

'Worst case' illustration

FIGURE 4.2 THE VARIOUS TIME STATISTICS OF PHOTOMULTIPLIER PULSES

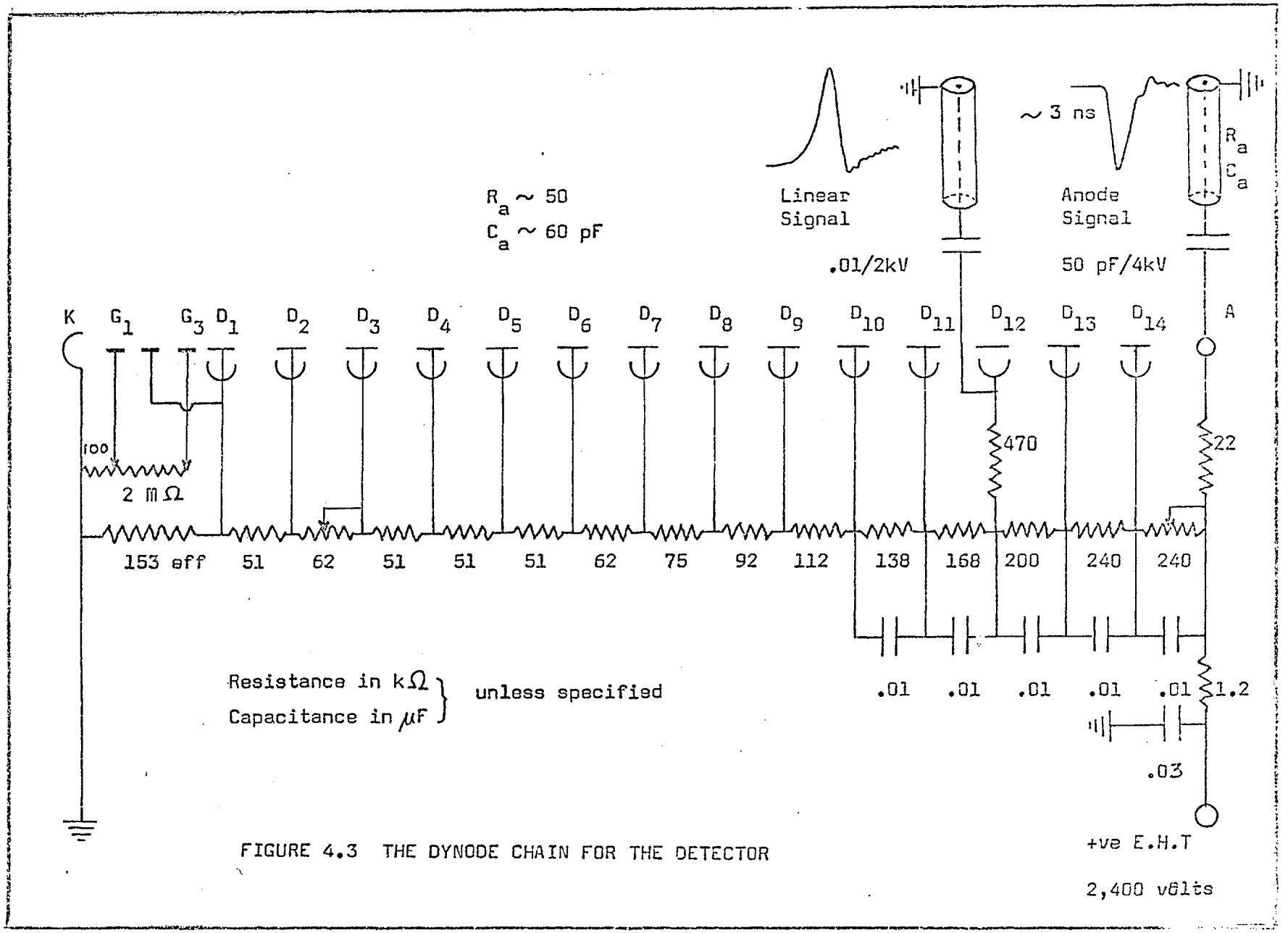


FIGURE 4.3 THE DYNODE CHAIN FOR THE DETECTOR

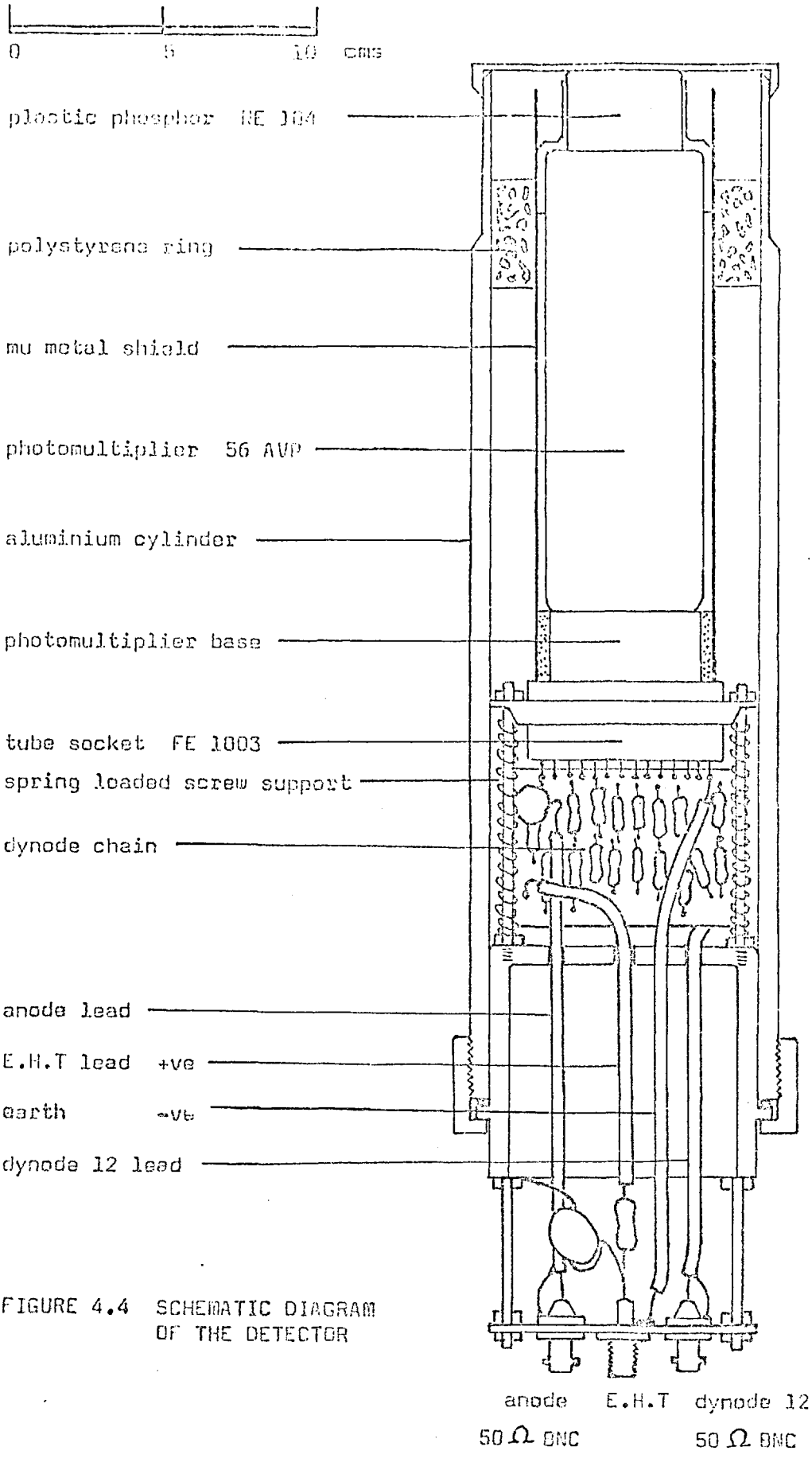


FIGURE 4.4 SCHEMATIC DIAGRAM OF THE DETECTOR

$$\sigma_n = \sqrt{[0.25/5 + 5(2/75)^2]} = 0.231 \text{ ns}$$

and

$$\sigma_{\overline{n}} = 0.138 \text{ ns}$$

The "slewing time" of the fast discriminator T100A (E.G. & G) is $\sigma_s = 0.5$ ns.

We therefore have

$$\sigma_G = \sqrt{2}(0.0176 + 0.25)$$
$$\simeq 0.73 \text{ ns}$$

This is the expected theoretical time spread in the prompt time spectrum.

4.3 APPARATUS

The source of gamma rays was a sodium 22 disc of one millicurie strength. It was enclosed in a plastic about 4 mm thick and 2 cm diameter to ensure complete positron-electron annihilation. In addition to the two 0.511 MeV annihilation gammas the sodium 22 also emits 1.28 MeV gammas. The source was placed in an aluminium holder which was slid into a cylindrical lead castle 2" thick, $6^1/4$" outer diameter and $7^1/2$" long.

The detectors were plastic phosphor-photomultiplier combinations. Plastic phosphor NE 104 (Nuclear Enterprises) was chosen because of its fast decay time, 2 ns, and its sensitivity to gamma rays and fast neutrons. The photomultiplier 56 AVP (Mullard) is a typically fast focussed tube with a high gain (14 dynodes) and good time characteristics. The rest of the fast electronics were supplied by Edgerton, Germeshausen and Grier Inc. (E.G. & G.). These modules have nanosecond time characteristics giving pulses of less than 2 ns rise time. The impedance was 50 Ω and pulse height was about 700 mV.

Since the 56 AVP is a fast high gain (> 10^8) tube special attention had to be paid in the construction of the dynode chain in order to ensure that "good clean" output pulses were obtained. Slight potential shifts especially in the last few stages would seriously distort the output pulses and cause oscillations. These had in fact been observed. After a series of trials lasting several months the dynode chain as shown in Fig. 4.3 was adopted as giving the most satisfactory performance. Because of space charge effects the potentials of the last few stages had to be stepped up. Moreover they were decoupled so that any ripples would be quickly attenuated and smoothed out. It was also discovered that the EHT supplies was a source of noise in the output and to minimise this contribution a 0.03 μF capacitance was used to filter the noise to earth. A typical bleeder current operating at 2,400 volts was about 1.5 mA. Because of saturation at the anode, a "linear" signal was taken off at the 12^{th} dynode. This output was necessary because it had to be used for energy selection purposes in the measurement of fast pulsed neutron decays later on. The "saturated" anode signal was used for timing purposes. The cathode rather than the anode was earthed because a "floating" cathode would give rise to troublesome effects, e.g. causing the glass tube to glow.

The dynode divider chain was made compactly on Veroboards. All connections were made as short as practical to reduce the effects of stray capacitances. The connections to the two outputs were carefully screened. The resistors were metal oxide types with very low inductances and good power ratings (1 Watt). The capacitors were high voltage disc ceramics (Erie). The plastic phosphor $1\frac{1}{2}$" diameter and 1" thick was coupled on to the photomultiplier with silicone grease to ensure good optical contact and was located by a thin cylindrical aluminium holder. The whole was housed in a light tight aluminium tube

1/4" thick, 4" outer diameter and 15" long as shown in Fig. 4.4. To reduce the effects of magnetic fields a mu-metal shield was put round the tube.

Output pulses (using the Na^{22} as a source) were observed on the fast 561A Tektronix Oscilloscope. The anode stray capacitance was estimated to be about 60 pF (10 from the tube, 30 from the connecting wire and the rest from various soruces such as the decoupling capacitor) and the anode load was 50 Ω. Using equation 4.9 we have a theoretical anode rise time of

$$\tau_r = [3 \times 2/(3 - 2)] \ln 3/2 = 6 \times 0.405 \simeq 2.4 \text{ ns}$$

which was comparable to the observed rise time.

The signal from the 12^{th} dynode had to be tested for linearity, i.e. to ensure that it was non-saturated. The plastic phosphor was temporarily replaced by a $1^3/4$" dia. by $1^1/2$" thick Sodium Iodide (Thallium Activated) crystal and the detectors' response to gamma rays of various energies was measured by feeding the dynode signal to the M.C.P.H.A. and noting down the positions of each photopeak. The tube was operated at 2,300 volts and the output amplification was kept constant. A correction for the slight non-linear response of the crystal to gamma energies other than that of Caesium 137 was made (R.L. Heath). A graph of photopeak position against gamma energy gave a linear relationship, Fig. 4.5. Table 4.1 gives the various sources used together with the corrected energies and photopeak positions:-

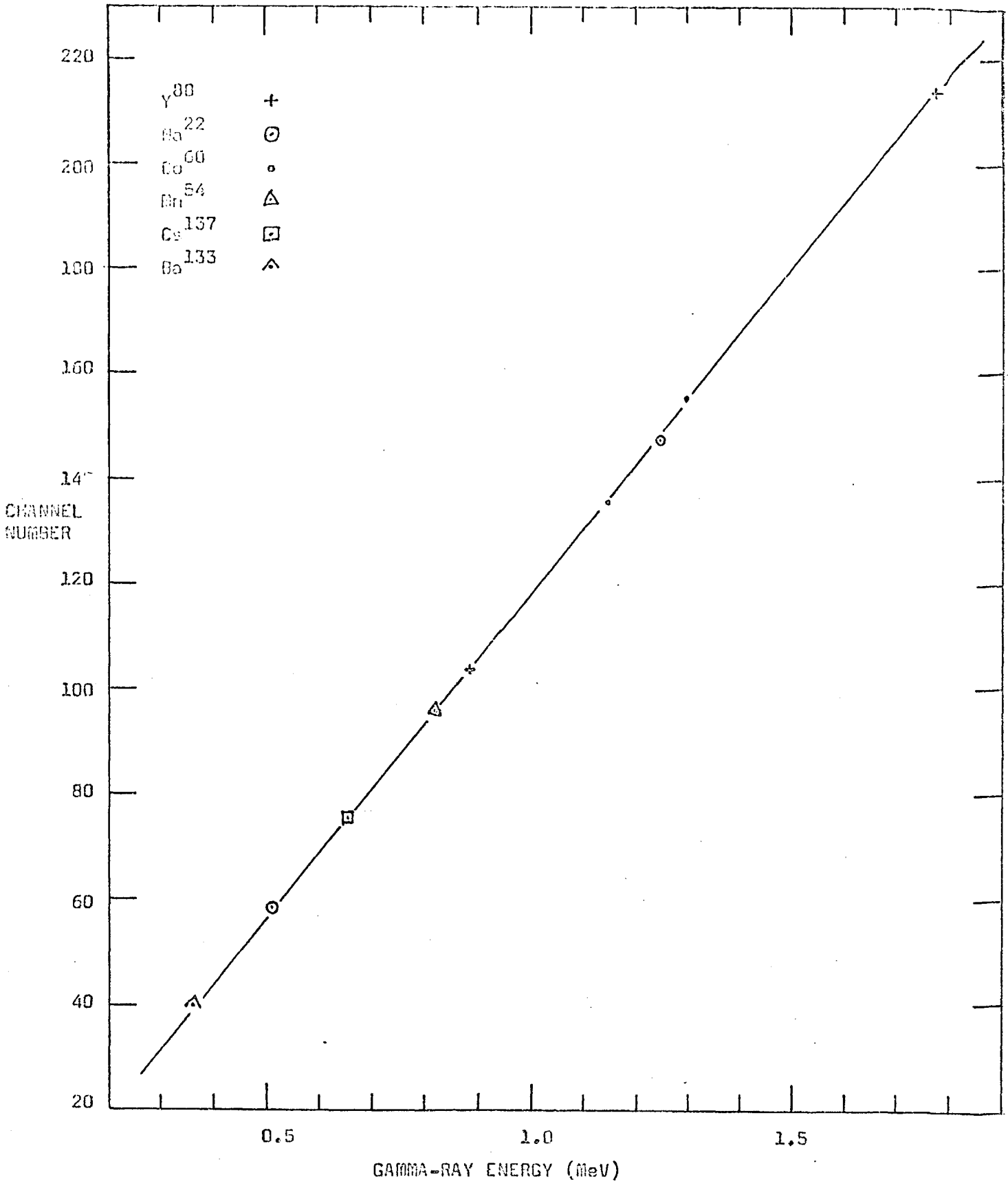


FIGURE 4.5 PHOTO-PEAK POSITION VS GAMMA-RAY ENERGY

SOURCE	ENERGY (MeV)	CORRECTED ENERGY (MeV)	PHOTOPEAK POSITION (CHANNEL NO.)
YTTRIUM 88	1.837	1.780	214 ± 1.0
	0.899	0.889	103 ± .5
COBALT 60	1.332	1.302	155.5 ± .5
	1.173	1.152	135.5 ± .5
SODIUM 22	1.280	1.252	147.5 ± .5
	0.511	0.516	58.5 ± .5
MANGANESE 54	0.835	0.828	96 ± .5
CAESIUM 137	0.662	0.662	75.5 ± .5
BARIUM 133	0.356	0.363	40.0 ± 1.0

TABLE 4.1. GAMMA RAY ENERGIES

The peaks of Yt 88 (1.837 MeV) and Ba 133 (0.356 MeV) were outside the range of the 200 channels used and "back biasing" had to be used to bring them "into the picture". Their actual positions were determined with reference to the corresponding shifts in the peaks of Cs 137 and Mn 54.

4.4 EXPERIMENTAL PROCEDURE

The Na^{22} source was placed in the middle of the cylindrical lead castle with detector 1 which gave the start pulses pressed against one flat side. Detector 2 which gave the stop pulses was placed on a straight Dexion track along which it could be slid and, for the zero reference position, was initially pushed against the otherflat side of the castle. The pulses from the anode were observed on the 561A Tektronix 'Scope in turn. The E.H.T. supplies were adjusted until the pulses were of the same voltage (about 4 volts). The count rates of both outputs were taken and further finer adjustments to the E.H.T.

units were made until the count rates were roughly the same. The two signals (typically 3 ns rise time and 5 ns wide) were then fed through 50 Ω screened cables to the two fast discriminators T100A whose threshold levels were set at 10% of the maximum pulse heights, viz. 400 mV. The outputs of the T100A were now delayed by nanosecond delay boxes DB 236 and fed to the Time-to-Amplitude Converter, the pulses from channel 1 into the start input and those from channel 2 into the stop. The steps taken to make the operating conditions of both channels the same were necessary to ensure as symmetrical a time coincidence spectrum as possible.

The range of the T.A.C. was set to the lowest one 0 to 100 nanoseconds. The output pulse width was adjusted to about 3 μs long and the dead time of the T.A.C. was set at about 50 μs. The negative rectangular output pulse was fed to the M.C.P.H.A. via a 5X attenuator and an amplifier. The amplification was adjusted so that the F.W.H.M. of the observed time coincidence spectrum was about 10 channels wide. A back bias of 2 volts was introduced and the stop pulses were delayed so that the spectrum was on a suitable (low channel) position on the display screen. This made sure that even for the initial zero position the spectrum was someway from the start edge of the conversion range. The spectrum was allowed to build up to a peak value greater than 10^4 counts. The counting time was noted. A printout was obtained and the memory core then erased. With all settings fixed, detector 2 was now moved along the Dexion rail in line with source and detector 1 to a position 25 cm away from the first position. A printout of the new spectrum was again taken. The procedure was repeated up to 4 metres with detector 2 in 14 different positions. Counting times ranged from 300 seconds for the zero position to 40 hours at 4 metres. Table 4.2 below shows the instrument settings during the experiment.

E.H.T. (kV)	2.25 (PMX 1)	2.24 (PMX 2)
DISC (mV)	400	400
CABLE LENGTH (m)	4	7.5
COUNT RATE OF PMX 1	approx. 6.3×10^5 per sec	
CONVERSION RANGE OF T.A.C.	0 - 100 ns	
INPUT AMPLIFICATION OF M.C.P.H.A.	10 x	
BACK BIAS	2 volts	
NO. OF CHANNELS USED	200	
CHANNEL SENSITIVITY	20 mV/ch	
DEAD TIME	50 μs	

TABLE 4.2 INSTRUMENT SETTINGS FOR GAMMA TIME OF FLIGHT

For the latter far away positions long times were needed to ensure good statistics. For such long times the electronics, especially the M.C.P.H.A. would drift and there would be small shifts in the peaks of the latter peaks. To correct for this the following procedure was adopted:- Immediately after a far position spectrum was printed out, detector 2 was moved back to the zero position and the corresponding spectrum obtained. The peak of this spectrum was compared with that of the original zero position and any discrepancy noted. This difference was then used to correct for the shifts in the peaks of the "far away" position spectra.

4.5 RESULTS AND ANALYSIS

The raw data obtained were corrected for the 50 μs dead time of the Time to Amplitude Converter according to

$$C_t = \frac{C_o}{(1 - C_o\tau)} \qquad 4.20$$

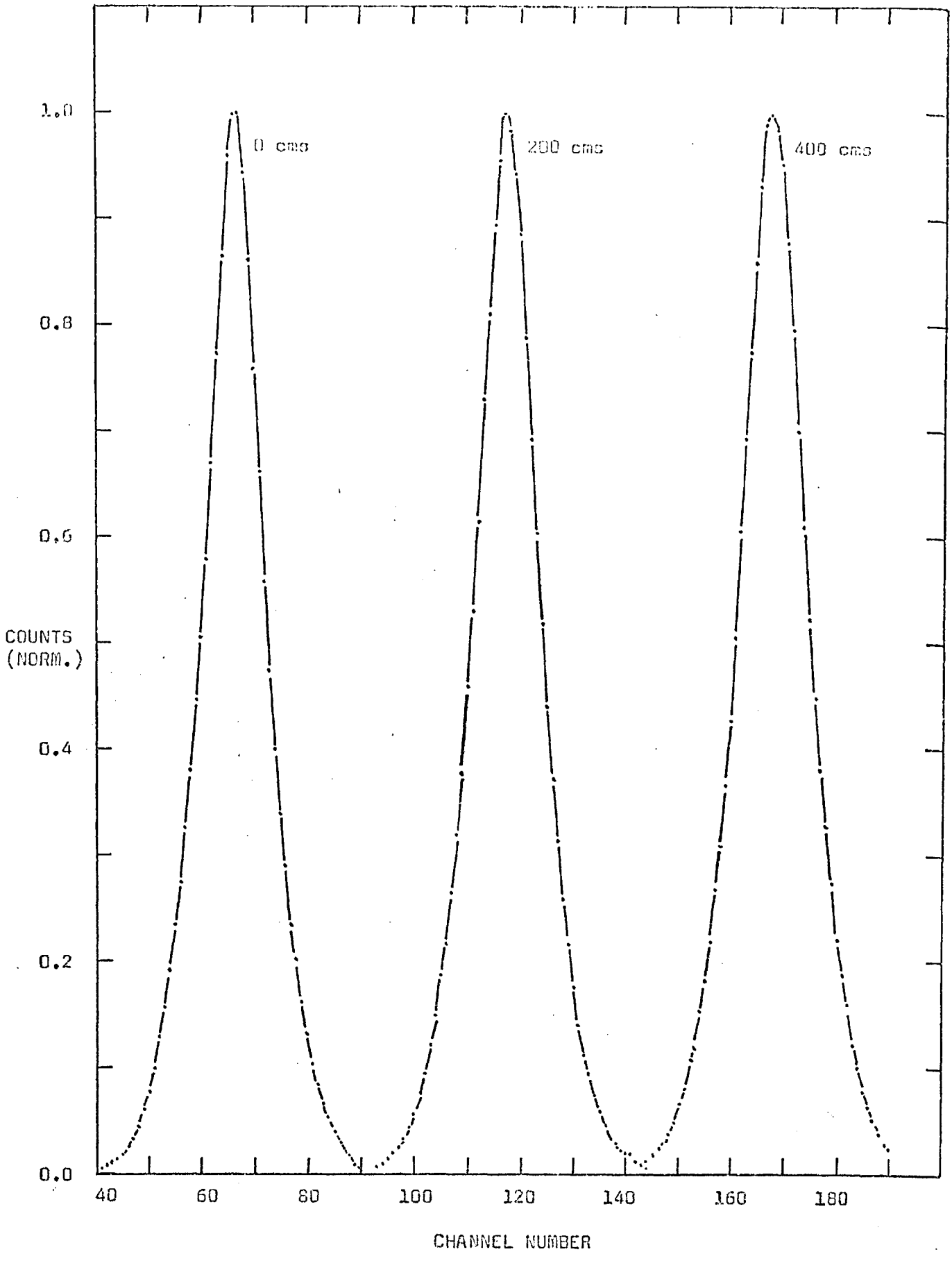
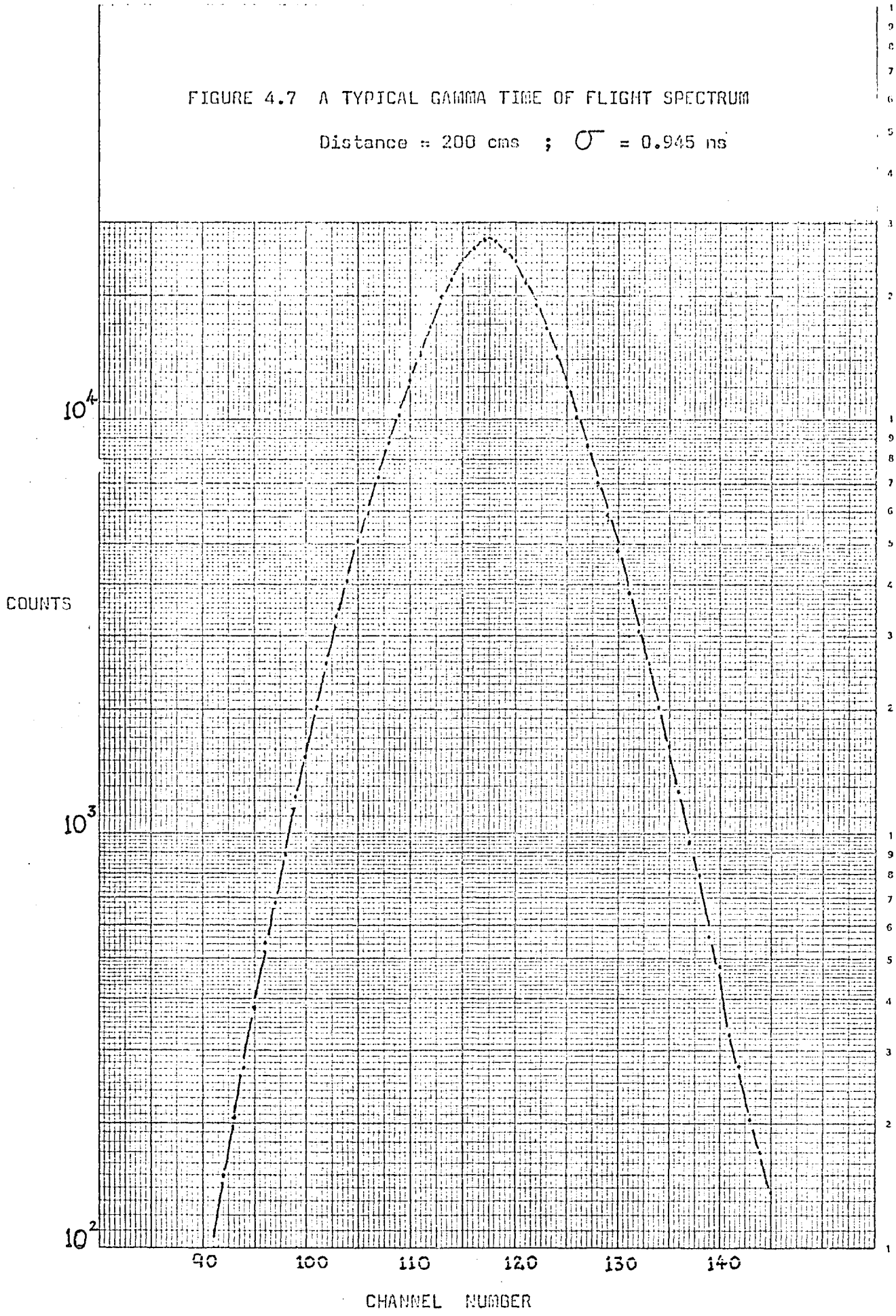


FIGURE 4.6 TYPICAL GAMMA TIME OF FLIGHT COINCIDENCE SPECTRA

FIGURE 4.7 A TYPICAL GAMMA TIME OF FLIGHT SPECTRUM

Distance = 200 cms ; σ = 0.945 ns



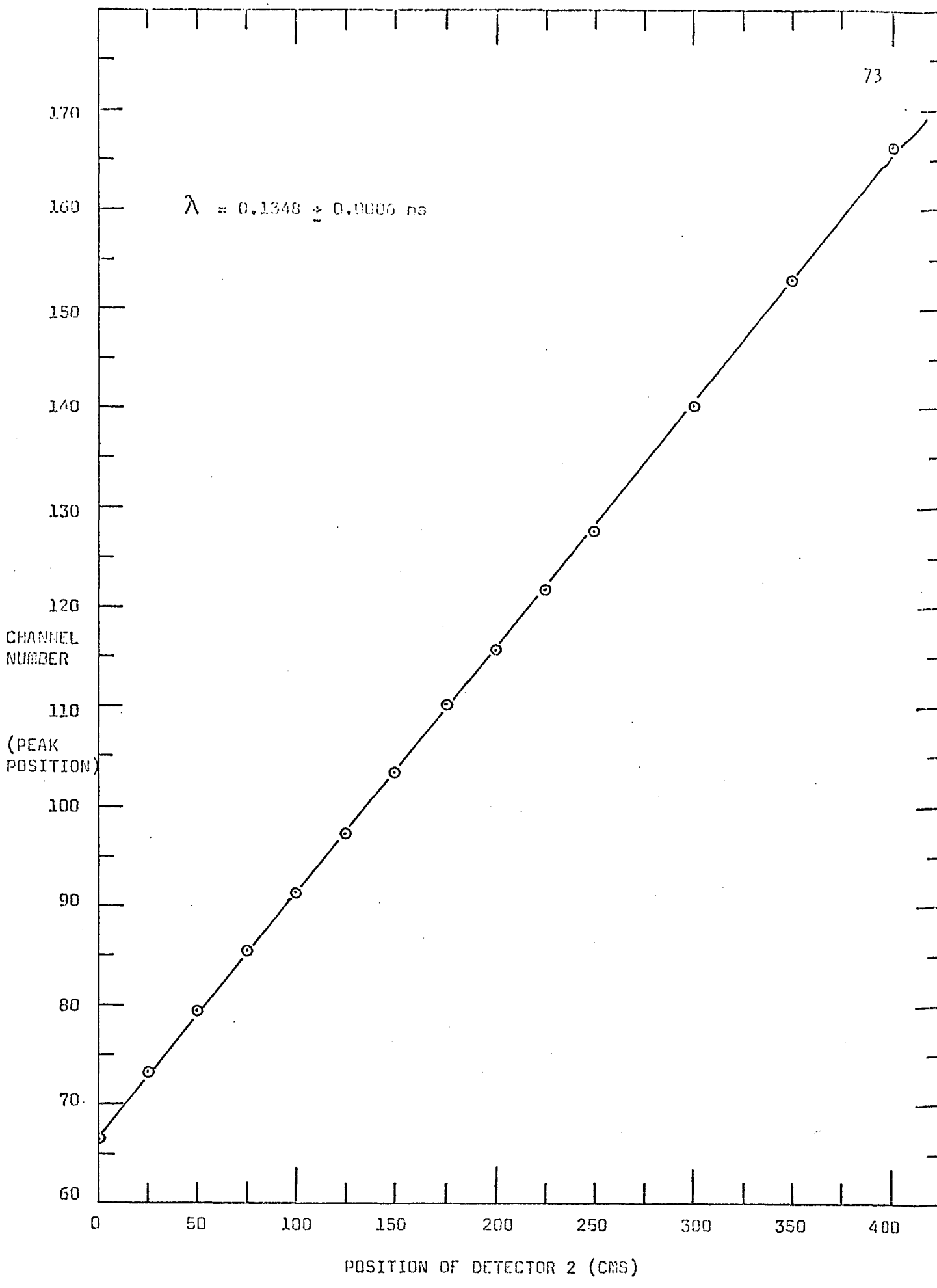


FIGURE 4.8 GAMMA TIME OF FLIGHT CALIBRATION LINE

where C_o is the observed count rate

C_t is the true count rate

and τ is the dead time.

This dead time overrode that of the M.C.P.H.A. (47 μs). The dead times of the rest of the electronics were negligible being typically less than 5×10^{-8} sec. The random background was observed to be quite constant in each case and was certainly less than 0.5% of the peak value. Table 4.3 below shows the results obtained at five distances and Fig. 4.6 shows some of the time spectra on a linear plot.

DISTANCE OF COUNTER 2 (cm)	MAXIMUM COUNTS	COUNTING TIME	CHANNEL NO. OF PEAK	BACKGROUND AVERAGED OVER 100 CHANNELS
0	55078	300 secs	67	207
100	9708	4080 secs	91	33
200	27455	12 hrs 15 mins	117	84
300	15160	15 hrs	142	53
400	21780	40 hrs	168	68

TABLE 4.3. MEASUREMENTS OF GAMMA TIME OF FLIGHT

Fig. 4.7 shows a typical time coincidence spectrum at 200 cm on a log plot. As can be seen it is quite symmetrical about the peak. Because of this good degree of symmetry exhibited by all the spectra, the data were corrected for dead time and background and fitted to a Gaussian distribution of the form

$$C_t = C_p . \exp[-(N - N_p)^2/2\sigma_G^2] \qquad 4.21$$

where C_t is the corrected counts

C_p is the maximum counts

N is the channel number

N_p is channel number of the peak

and σ_G is the Gaussian standard deviation.

The object of the fitting procedure was to obtain N_p as accurately as possible and also σ_G.

The dead time and background corrections and the Gaussian fittings were carried out by the FORTRAN IV computer programme LEEFIT. This is an adaptation of the programme PARFIT written by Peter Johnson which does non-linear least squares fits up to 4 parameters by an iterative procedure. In this present case guess values of the parameters C_p, N_p and σ_G were fed into LEEFIT and a solution effected by repeatedly improving the parameters by small increments (calculated by the programme) until all increments were less than the convergence criteria specified. Errors attendant on these parameters were also estimated by the programme. LEEFIT can accept as many problems as are permitted by computer time and output specifications and hence the fitting of the spectra were carried out in one run. A typical 17 point fit took 6 iterations for convergence in a time less than 0.1 minute. Some results of the Gaussian fits are shown in Table 4.4 below.

DISTANCE OF COUNTER 2 (cm)	MAXIMUM COUNTS C_p	CHANNEL NO. OF PEAK N_p	GAUSSIAN SPREAD CHANNELS) σ_G
0	49028 ± 2157	$66.13 \pm .25$	$6.60 \pm .03$
100	8511 ± 315	$91.29 \pm .19$	$6.73 \pm .03$
200	24323 ± 789	$117.40 \pm .17$	$6.93 \pm .03$
300	13660 ± 448	$142.22 \pm .19$	$7.08 \pm .03$
400	19908 ± 590	$168.08 \pm .17$	$7.14 \pm .03$

TABLE 4.4 RESULTS OF GAUSSIAN FITS

In order to detect any shift of the peaks in the far away positions due to electronic drifts a Gaussian fit of the zero position spectrum

obtained after moving back the counter from the furthest position (400 cm) was made and the peak channel was now found to be 67.90 giving a shift of 1.77 channels. When a linear fit of peak channel number N_p versus position of counter 2 was made using LEEFIT, it was found that the best result was obtained when each peak channel number from 225 cm upwards was reduced by 1.77 channels. Fig. 4.8 shows the result of the 14 point linear fit. With reference to equation 4.2, the fitting yielded

$$\frac{1}{\lambda C} = 0.2472 \pm .00109$$

$$\frac{\Delta T}{\lambda} = 66.51 \pm .23$$

Taking the velocity of light C to be 2.99792×10^{10} cm/sec,

$$\lambda = (0.1348 \pm .0006) \times 10^{-9} \text{ sec/channel}$$

This is the time constant of the multichannel analyser under the operating conditions described.

$$\Delta T \simeq 8.9 \times 10^{-9} \text{ sec.}$$

The M.C.P.H.A. was back biased by 2 volts at a sensitivity of 20 mV/ch giving a further 13.5 ns so that the total time delay was 22.4 ns. The cable length difference between the two channels was about 3.5 metres which at the quoted 5 ns per metre gave 17.5 ns. The relative delay in the delay boxes was around 5 ns so that the fitted value of ΔT was quite reasonable.

From Fig. 4.7 it can be seen that the F.W.H.M. is 13 channels wide. From equation 4.19

$$\sigma_G = W_{1/2}/2.36 \simeq 0.74 \text{ ns.}$$

This gives very good agreement with the theoretical value of 0.73 ns. However the fitted parameter σ_G gives 0.945 ns. This and the fact that

the fitted peak counts were below that of the observed maximum counts shows quite clearly that the actual time spectra was more peaked and less 'bulgy' than a Guassian distribution. This implies that the former was better than the latter but nevertheless the fitting procedure was quite accurate in locating the positions of the peak.

CHAPTER 5

FAST PULSED NEUTRON DECAY MEASUREMENTS IN IRON

A description is presented in this chapter of how measurements of fast pulsed neutron decays in iron blocks were attempted. Two injection energies were chosen at 2.427 MeV and 1.285 MeV, the neutrons being produced by the T(p,n) He^3 reaction using the 6 MeV/5 Mc/s Van de Graaff accelerator at A.W.R.E., Aldermaston. Measurement was made with two block sizes of 12" x 12" x 12" and 15" x 15" x 18". Too small a size would mean that the dimensions become comparable with the extrapolated distance and the leakage spectrum becomes similar to the primary spectrum with a pulse width of 4×10^{-9} s. A very large size would incur a high background since the long decay would approach the machine pulsing time. Calculations with reasonable values of Σ^{tr} for iron for the two worst cases, high energy and small size, and low energy and large size, indicated that $7 \times 10^7 < \lambda < 3 \times 10^8$ sec^{-1} so that these were in fact "safe" dimensions, the limits being 5×10^6 and 2.5×10^{10} sec^{-1}. Ideally experiments should have been conducted at several energies with a wide range of bucklings, but the very limited time of four days allocated to the author did not permit this.

One of the main aims was to try to ensure that the neutrons decaying from the blocks could be considered as monoenergetic, allowing for the slight elastic moderation. To meet this requirement energy gating of the leakage spectrum was applied. With each block size measurements were made with the detector in line with the neutron beam and perpendicular to it; this was to find out spatial effects (if any) on the decays. The problem of separating out the neutrons from the gamma rays generated by (p,γ) reactions at the target was resolved by

time-of-flight. The gammas produced by (n,n',γ) inelastic processes in the iron (e.g. the 0.847 MeV and 2.085 MeV levels of Fe^{56}) could not be separated as such since the detector was sensitive to both fast neutrons and gamma rays. However these gammas would decay in intensity at the same rate as the neutrons and since the time spectrum was the primary objective they did not pose a problem.

5.1 APPARATUS

The pulsed horizontal proton beam passed through an electrostatic pick-up system before reaching the target. The signal from the pick-up was used for zero-timing. Since the pick-up was about 6.8 metres from the target it was necessary to delay the start pulse to compensate for the time-of-flight of the protons down the beam tube. The non-relativistic time-of-flight is given by

$$t(ns) = 72.3\ D(m)\ /\sqrt{E_p}\ (MeV) \qquad 5.1$$

Thus for protons at 3.2 MeV, for example, a delay of about 0.27 μs was needed and this was provided by the insertion of 50 yards of Unirad. 43 Cable. The positive, attenuated pulse was inverted and amplified before feeding into a fast discriminator TR104 (E.G. & G.) which then provided a standard signal for the start of the Time to Amplitude Converter (TH200A).

The neutrons were generated by the $T(p,n)\ He^3$ reaction. The target was a zirconium disc 7/16" in diameter and about 0.05" thick with a total of 0.5 mgm tritium. This reaction yielded monoenergetic neutrons and had a sharp threshold which made it easy for energy calibration (to be described later). The target was ring-clamped on to the plate of a brass target assembly designed by the author. The details

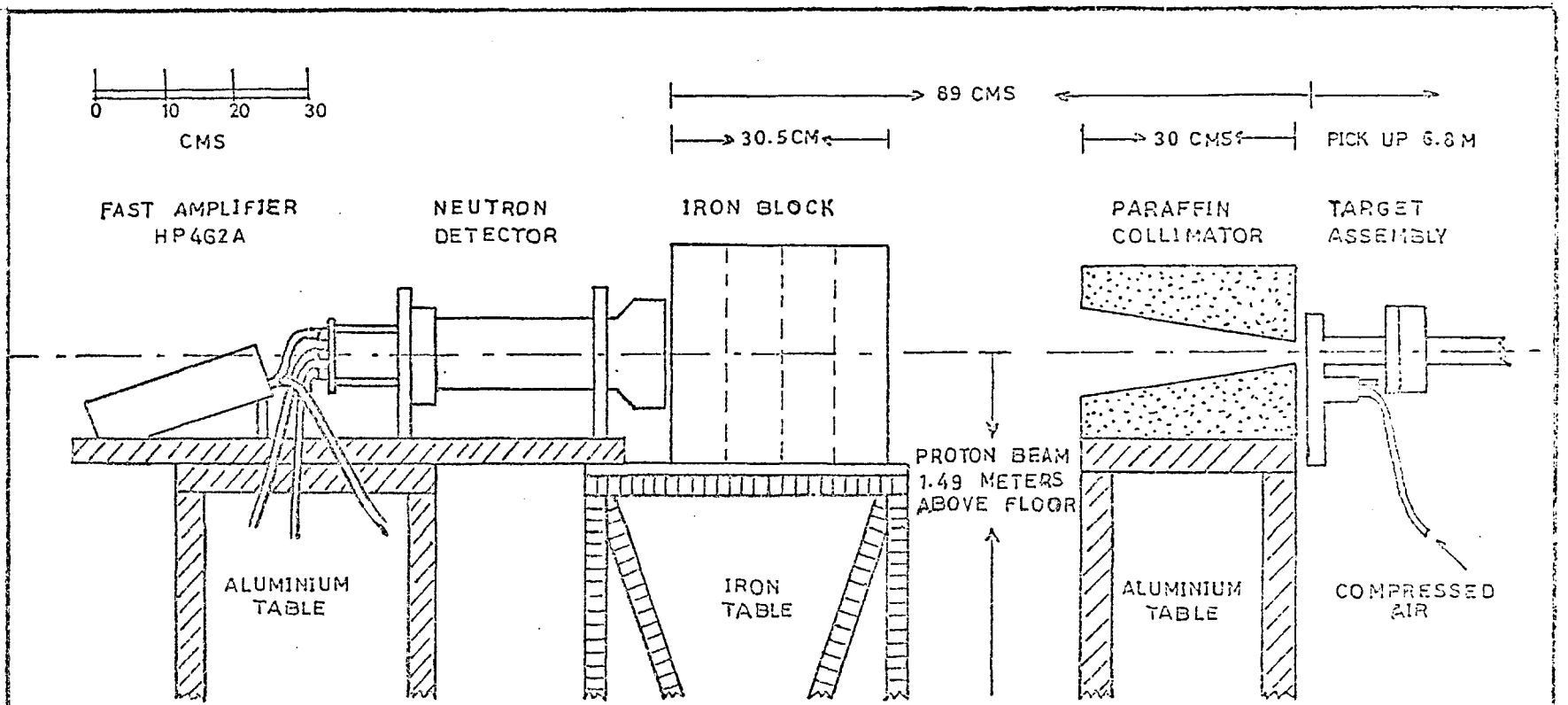


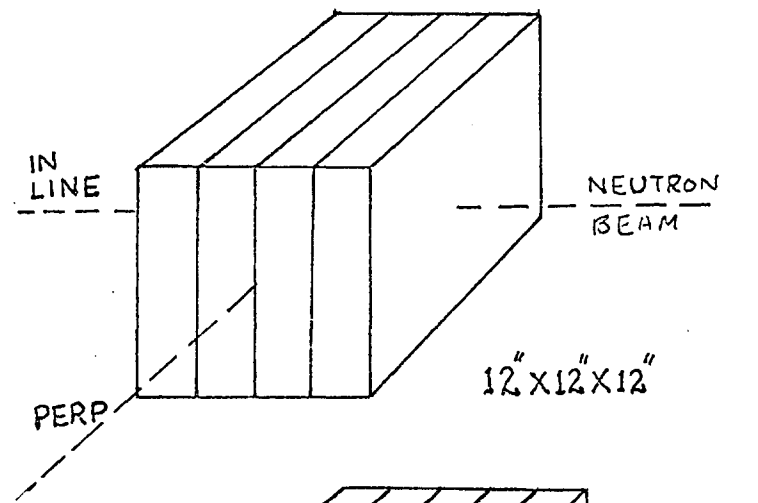
FIG. 5.1 GEOMETRY FOR DECAY OF PULSED NEUTRONS IN IRON BLOCKS

of the assembly are shown in Fig. 5A at the back. A tungsten diaphragm with a 0.5" diameter hole was inserted in front of the assembly. The traget was cooled by blowing compressed air into the thick part of the plate. This was necessary to minimise tritium evaporation due to energy deposition by the proton beam. The emerging neutrons were collimated by a 30 cm thick paraffin cone with a semi angle of about 11°. The iron blocks were placed about 29 cm away from the cone (Fig. 5.1). For the small size (large buckling), 4 slabs of 12" x 12" x 3" were combined and held together by a small iron strip placed diagonally on top and screwed in at both ends. For the large size (small buckling), 5 pieces of 12" x 12" x 3" were combined with a 12" x 15" x 3" piece and put on top of 2 slabs of 15" x 15" x 3", (Fig. 3.2). These rested on a flat 0.5" thick iron plate supported on a 18" by 18" iron table. The height of the table was adjustable by placing small 1" thick blocks underneath it so that both sizes could be centred with respect to the proton beam, the latter being 1.49 metres above the floor. The slabs were first grade iron conforming to British Standards No.15. A movable block and tackle system was used to shift the slabs, which weighed between 120 lbs and 190 lbs each. To facilitate handling, two 0.5" diameter holes were drilled and tapped at the ends of a narrow surface of each slab so that lifting screws could be inserted.

The detector was the fast decay plastic phosphor NE 104 used in conjunction with a fast photomultiplier, the 56AVP, as described in the previous chapter. For the purpose of neutron detection, however, a 5" diameter 1" thick phosphor was employed since it was desirable to detect a fair proportion of the spectrum leaking out of a side. The count rate would of course be enhanced and the counting time reduced. The phosphor was indirectly coupled on to the photomultiplier through a 2"

thick, 40° semi-angle conical light guide as shown in Fig. 5.3. The surfaces were smeared with silicone grease to ensure good optical contact whilst the sides of the phosphor and cone were surrounded by thin aluminium foils to prevent loss of light laterally. The whole assembly was encased and made light-tight. From the end of the detector were three cables, each about 20 metres long, leading to the control room. Two with BNC 50 Ω connections were for the anode and dynode signals whilst the third one with high voltage connections was for the E.H.T. supply to the tube. Since the relatively small dynode pulses (from the 12^{th} dynode) were greatly attenuated by the length of cable used, they were fed into a fast, inverting, linear amplifier HP 462A (Hewlett-Packard) prior to being driven along the cable. The larger anode signals were also attenuated but they were still usable at the other end so that there was no need for immediate amplification. The detector system here would give a poorer time resolution than that obtained in Chapter 4. However, even this would be small compared to the 4 ns width of the proton pulses and this latter time uncertainty was in fact mainly responsible for the resolution. The detector-amplifier system and the paraffin collimator were supported on aluminium stands. Fig. 5.1 shows the geometry of the arrangement in the Van de Graaff room for the in-line detection.

The electronic circuitry adopted was of the fast time coincidence type employing a Time-to-Amplitude Converter (T.A.C.) subject to gating by an energy selection circuit (Fig. 3.4.). The anode signal with a typical rise time of 3 ns and about 500 mV was used solely for timing (i.e. to produce the decay spectrum with respect to the pick-up signal). It was amplified, delayed appropriately and fed to a fast discriminator TR104 which gave out standard pulses for the stop input to the T.A.C. The pick-up pulse would initiate conversion until the arrival of a stop



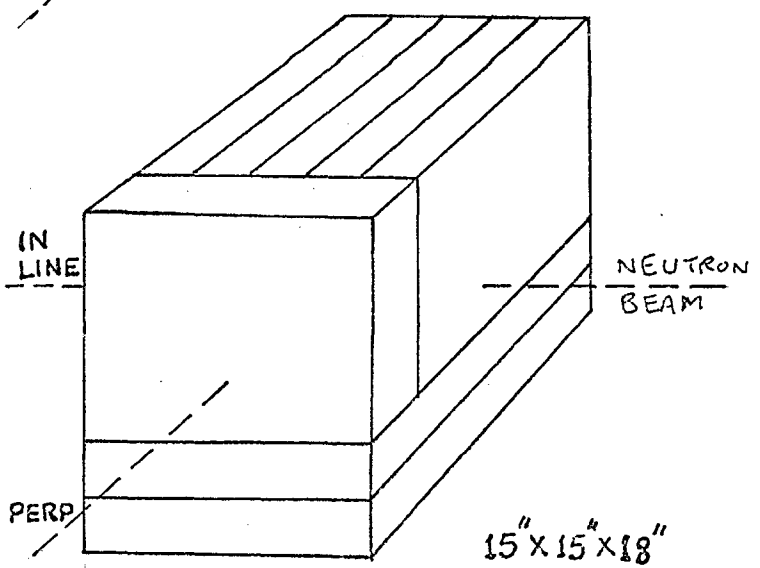


FIG. 5.2 BLOCK ARRANGEMENTS

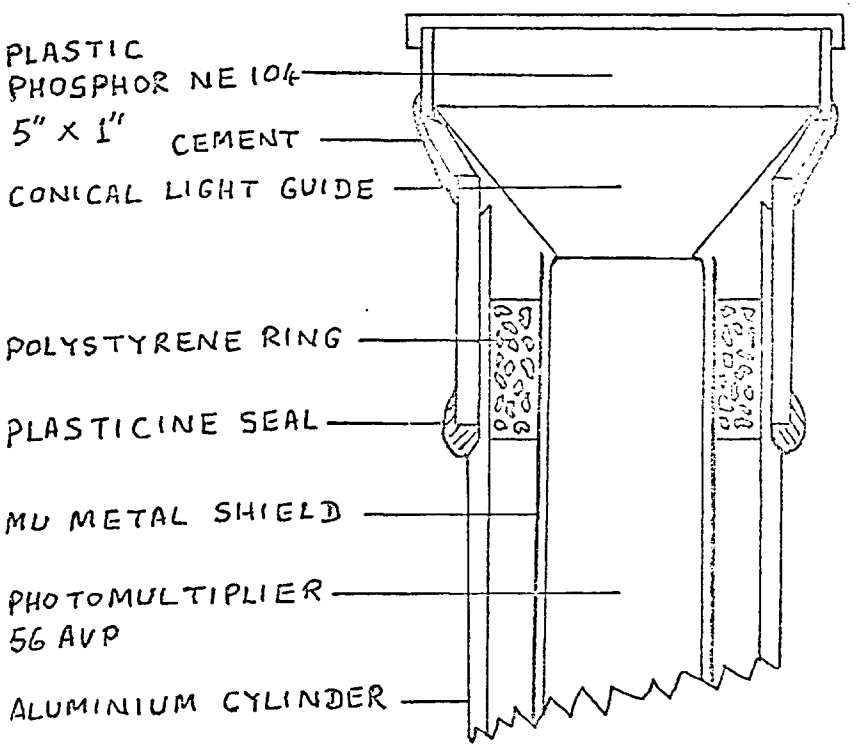


FIG. 5.3 DIAGRAM OF DETECTOR HEAD

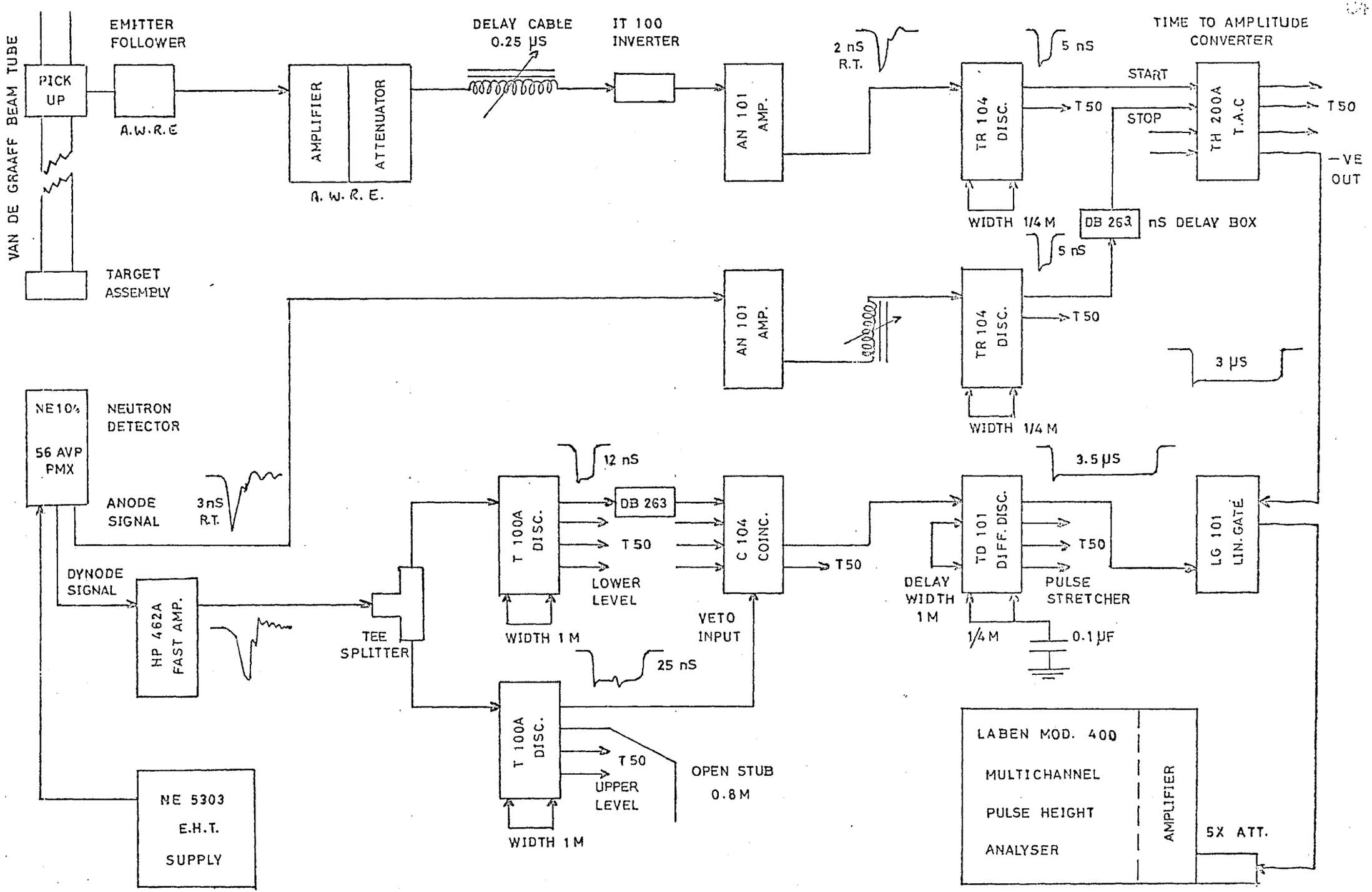


FIG. 5.4 BLOCK DIAGRAM OF 50Ω ELECTRONIC SYSTEM FOR PULSED NEUTRON DECAY MEASUREMENTS

pulse which might be due to a neutron, a gamma or some random event so that the output when displayed on a Multichannel Analyzer (M.C.P.H.A.) would represent the neutron decay spectrum plus a background along the whole conversion range of the T.A.C. If the range was set at 0 to 1 μs 5 decay spectra could be observed since the machine repetition rate was 5×10^6 c/s. Energy selection was effected by splitting the dynode pulse (after amplification) with a Tee piece and feeding into two fast discriminators T100A which when used in conjunction with the coincidence unit C104 operated in the anti-coincidence mode (veto input) served as a differential discrimination. The upper level (E + ΔE) pulse width was doubled by reflection along a 0.8 metre open stub and then fed into the veto input of the C104. The lower level (E) pulse, about 12 ns wide, was made to "sit" inside the longer pulse by adjusting the ns delay box DB 263, and observing both pulses on the fast Tektronix 'Scope 561A. This meant complete overlap so that the C104 output was essentially the same as the lower level pulse. No output would be produced whenever a pulse was present at the veto input. The lower level pulse should never be wider than the upper level one since this would imply that parts of the lower level would not be subject to the veto at all thus giving rise to erroneous outputs.

The inputs to the T.A.C. were made as narrow as possible (about 5 ns) to reduce the time uncertainty. The negative output was used, the pulse width being adjusted to 3 μs and the dead time set at 50 μs. Since this pulse width was 3 μs and since the M.C.P.H.A. would only accept pulses greater than 0.3 μs the energy pulse had to be stretched in order to gate the T.A.C. output properly. This was achieved by using a 0.1 μF capacitive delay inserted in a differential discriminator TD 101. The TD 101 did not function as a discriminator but it served effectively as a pulse stretcher, giving a pulse of width about 3.5 μs which was fed into the linear gate LG 101 to gate the incoming negative T.A.C. signal. The

gated signal was finally fed after suitable amplification into the Laben 400 Multichannel Pulse Height Analyzer (M.C.P.H.A.). An IBM electric typewriter was connected to the latter for print out purposes. Apart from the M.C.P.H.A. the whole logic system employed fast electronics. This differed from the conventional circuitry where the energy selection was usually achieved by using slow electronics (μs resolution). Because of the fast electronics used it was not necessary to adjust for any relative delays between the timing and energy selection channels. The stretched pulses for the gate would easily account for relative delays up to 1 μs long. The fast modules were supplied by Edgerton, Germeshausen and Grier Inc. (E.G. & G.). They have 50 Ω impedance giving standard pulses of 700 mV with a characteristic rise time of less than 2 ns. Pulse widths were usually adjusted by inserting given lengths of 50 Ω cables, the relation between pulse width (PW ns) and cable length (L metre) being

$$L = \frac{PW\ (FWHM)}{2 \times 5.06\ ns/m} \qquad 5.2$$

Output sockets not used were properly terminated in 50 Ω. Fig. 5.4 gives a layout of the electronic system employed.

The average proton current at the target was about 1.5 μA, a higher value could not be achieved since the Van de Graaff was beset with leakage troubles at the time of the experiment. The total number of neutrons yielded per sec was given by

$$n_n = \phi_p n_T \sigma_{p,T} \qquad 5.3$$

Here the proton flux would be numerically the same as the average current so that, with 1.6×10^{-19} Coulomb per proton, $\phi_p \simeq 10^{13}$/sec. With a total of 0.5 mgm tritium and atomic weight $3.0164 \times 1.66 \times 10^{-24}$ gm, $n_T \simeq 10^{20}$. The (p,T) cross-section could be taken as 0.45 barns in the

energy range of interest (Fig. 3.7) so that n_n was estimated at 4.5×10^8 neutrons per sec. The number that went through the cone with a half-angular spread of 12° (Fig. 5.5) would be around 5×10^6 per sec. Isotropic generation of neutrons has been assumed. With this flux injected into the iron block it is seen that less than one neutron event was detected per machine pulse.

5.2 ENERGY DETERMINATION

The relation between neutron energy E_n and proton energy E_p in the $T(p,n)\ He^3$ reaction is governed by the non-relativistic equation

$$\sqrt{E_n} = \alpha \pm \sqrt{\alpha^2 + \beta} \qquad 5.4$$

where $$\alpha = [\sqrt{M_1 M_3 E_p}/(M_3 + M_4)] \cos \theta_3 \qquad 5.5$$

and $$\beta = [M_4 Q + E_p(M_4 - M_1)]/[M_3 + M_4] \qquad 5.6$$

$M_1 = 1.0076$ a.m.u., $M_2 = 3.0164$ a.m.u., $M_3 = 1.00898$ a.m.u. and $M_4 = 3.0159$ a.m.u. are the rest masses of the proton, tritium, neutron and He^3 respectively and θ_3 is the angle of neutron emission. The Q value is related to the threshold energy E_{th} by

$$E_{th} = -Q[M_1 + M_2]/M_2 \qquad 5.7$$

E_{th} has been accurately measured (Fowler et al.) and is given as 1.019 MeV so that $Q = -0.764$ MeV. For $E_p >> E_{th}$, only the positive sign in equation 5.4 will apply. Fig. 5.8 shows the relation between E_p and E_n for $\theta_3 = 0°$ and 12°. Equation 5.4 is arrived at by considering particle collision in the isotropic lab. system (Fig. 5.6) and applying energy and momentum conservation. For energies of a few MeV non-relativistic treatment is justified.

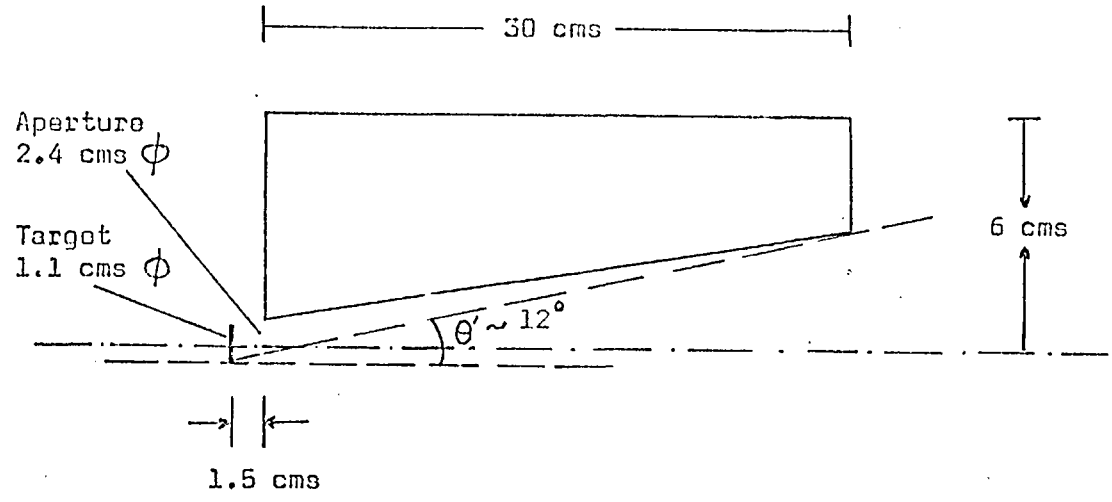


FIGURE 5.5 GEOMETRY FOR PARAFFIN COLLIMATOR

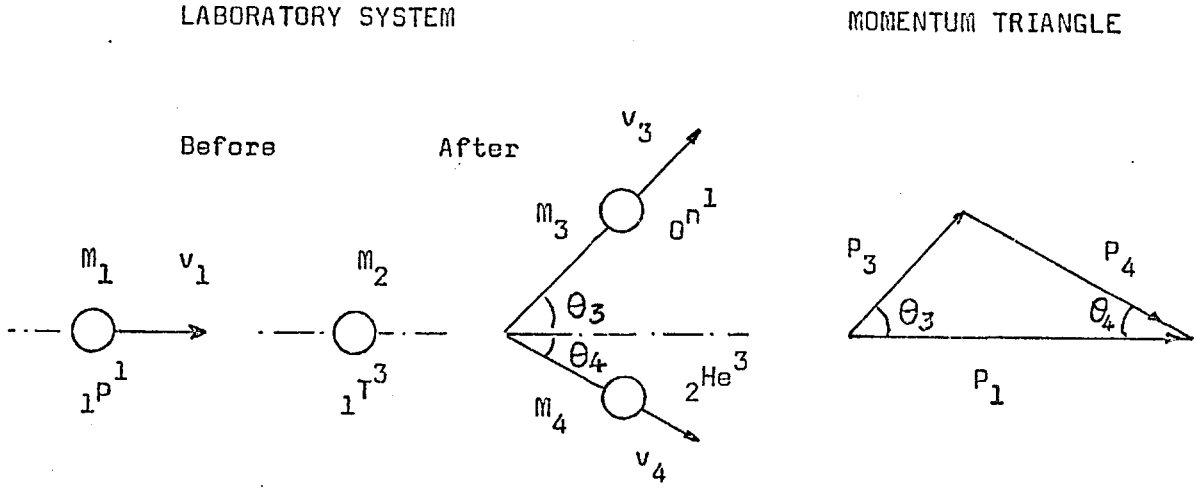


FIGURE 5.6 KINETICS OF COLLISION

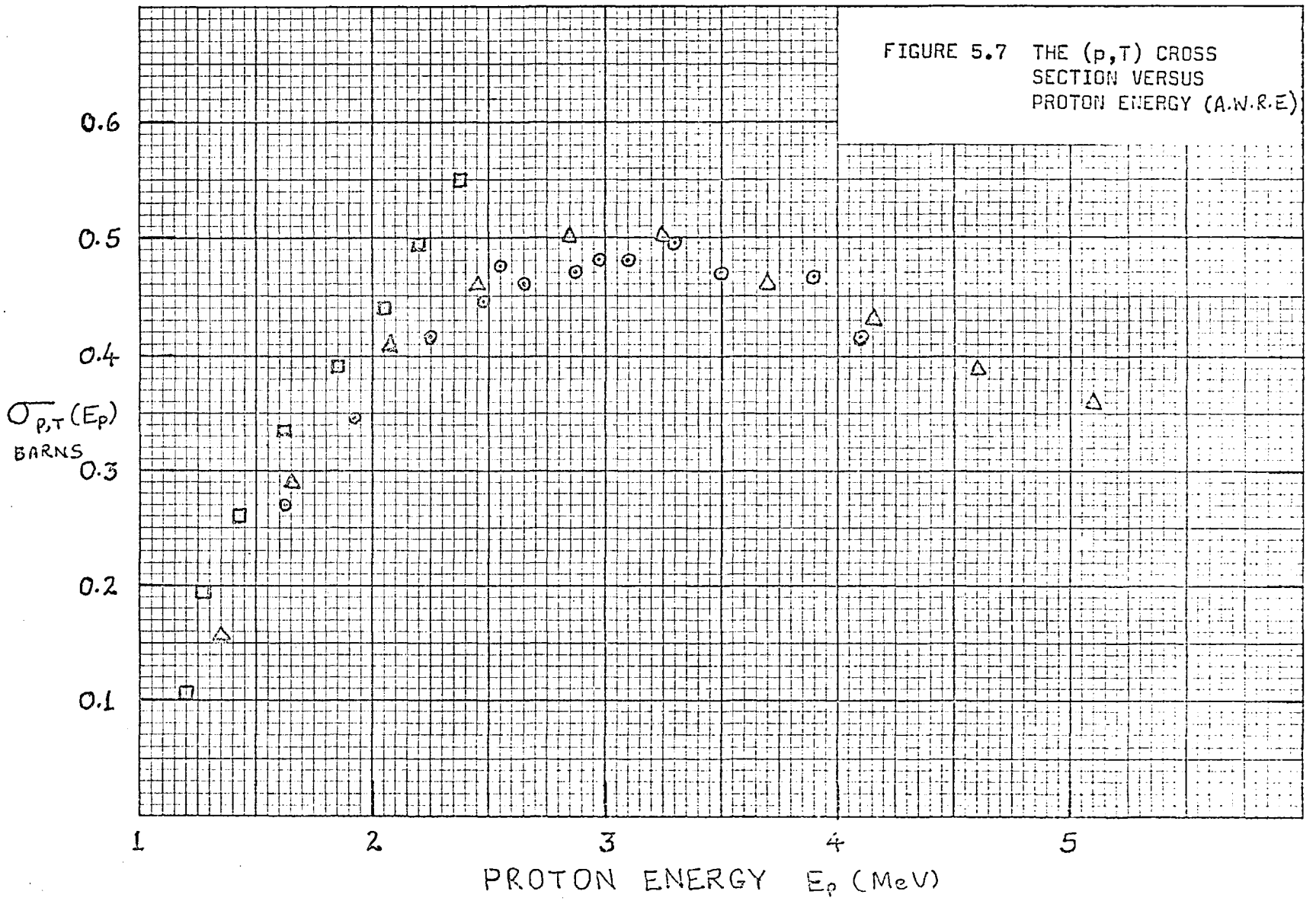


FIGURE 5.7 THE (p,T) CROSS SECTION VERSUS PROTON ENERGY (A.N.R.E)

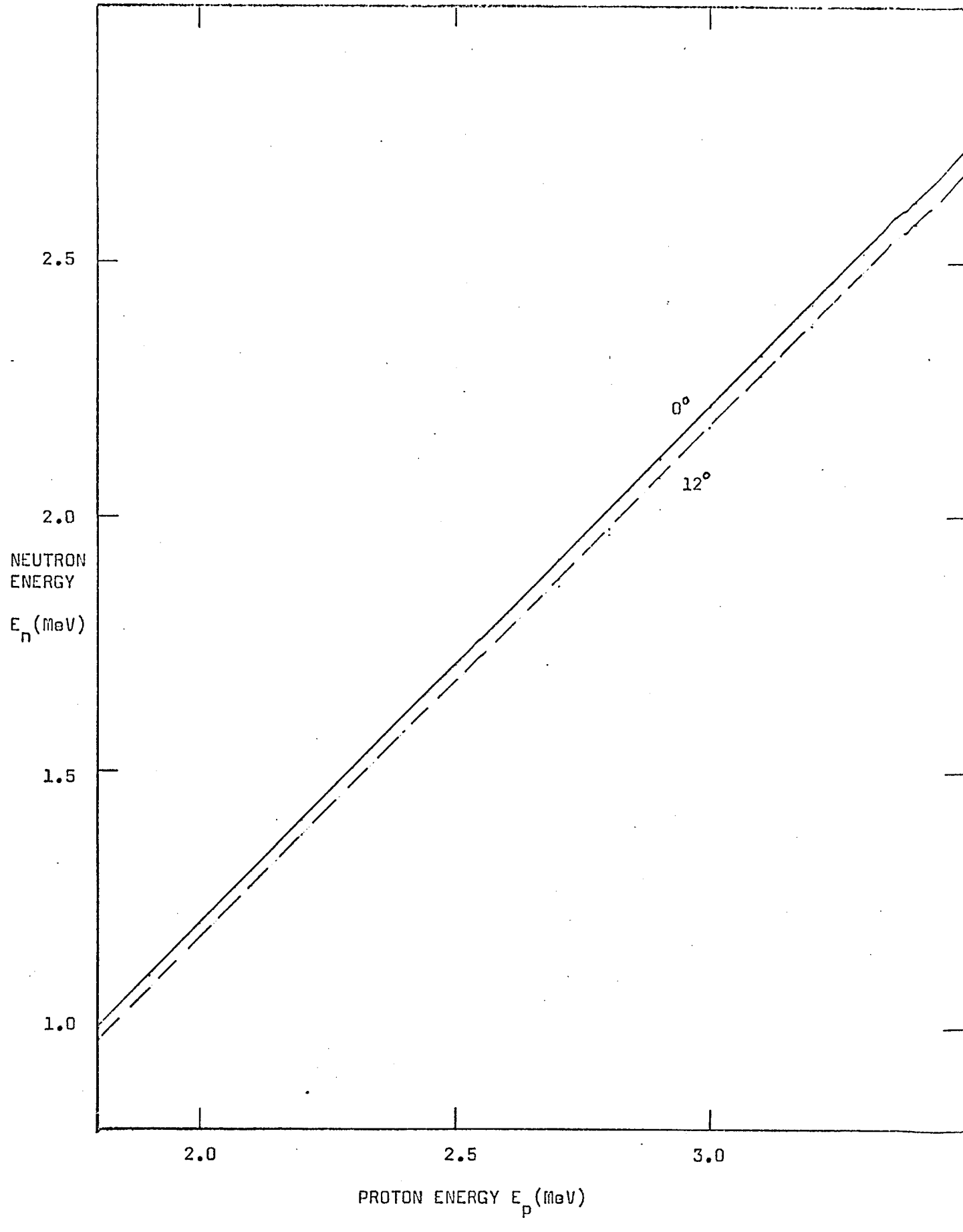


FIGURE 5.8 RELATIONSHIP BETWEEN PROTON AND NEUTRON ENERGY FOR THE $T(p,n)He^3$ REACTION

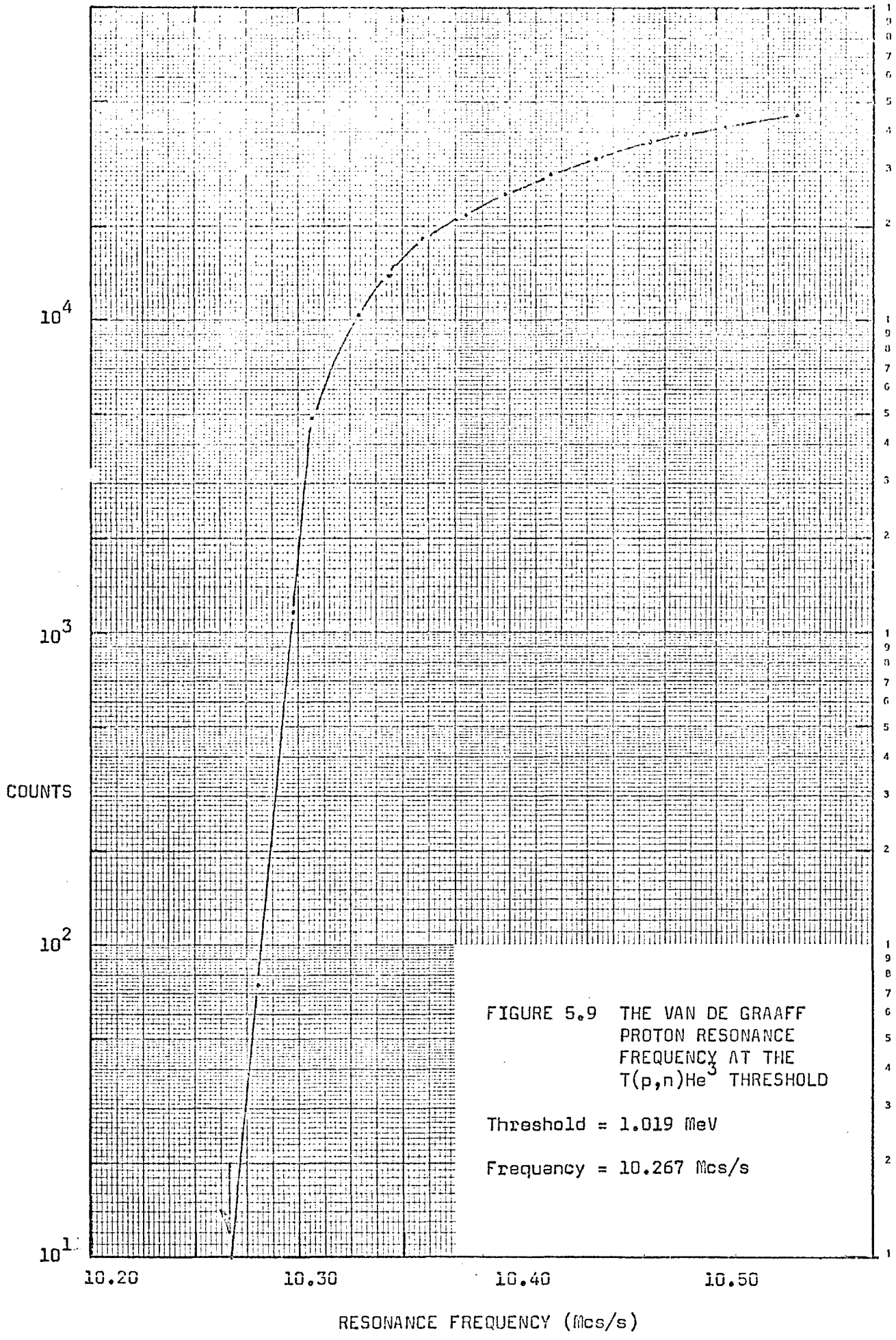


FIGURE 5.9 THE VAN DE GRAAFF PROTON RESONANCE FREQUENCY AT THE $T(p,n)He^3$ THRESHOLD

Threshold = 1.019 MeV

Frequency = 10.267 Mcs/s

The Van de Graaff was calibrated in terms of proton energy by the resonance frequency f of its bending magnet (nuclear magnetic resonance). First of all a magnet constant M_o must be determined from the threshold frequency f_{th}. The threshold was found by taking neutron counts with a BF_3 long counter placed in front of the target whilst the frequency was stepped up by small increments. The counting time was that taken to integrate over 100 Coulombs at the target. Timing by ordinary means was not advisable since the current would fluctuate and the reaction rate therefore not constant. Fig. 5.9 shows the plot of counts against frequency. The curve was extrapolated down to 1 count which was less than 0.025% of the highest count and this was taken to be the threshold frequency f_{th} = 10.267 Mc/s. The magnetic strength H_ρ was tabulated against proton energy (D.S. Mather, A.W.R.E.) and was related to f by

$$H_\rho = M_o \times f \qquad 5.8$$

At E_p = 1.019 MeV, f = 10.267 Mc/s and H_ρ = 145.899 so that M_o = 14.2119. The chosen operating frequencies were 18.320 Mc/s and 14.801 Mc/s giving H_ρ as 260.364 and 210.337 from which E_p was found to be 3.2414 MeV and 2.1169 MeV respectively.

The loss in energy per unit length dE_p/dx (keV/mgm cm^2) was known from the appropriate range-energy table (D.S. Mather) and hence the actual spread in the proton energy could be calculated for 0.5 mgm tritium in 0.9698 cm^2. The collimated neutrons in addition to the spread in the target had a 12° angular spread due to the cone (equation 5.4). Table 5.1 shows the calculated energy uncertainties together with the mean energies.

Proton Energy E_p (MeV)	3.241	2.117
dE_p/dx keV/mgm cm^2	70	92
Spread in E_p	0.036	0.046
Mean $\overline{E}_o$ (MeV)	$3.223 \pm .018$	$2.0934 \pm .023$
Neutron Energy E_n (MeV)		
at 0°	$2.442 \pm .019$	$1.299 \pm .024$
at 12°	$2.411 \pm .017$	$1.272 \pm .023$
Angular spread	0.031	0.027
Mean Neutron Energy $\overline{E}_n$ (MeV)	$2.427 \pm .023$	$1.285 \pm .027$

TABLE 5.1. ENERGY SPREAD AND AVERAGED ENERGY

When the beam was injected into the iron block the neutrons were subjected to elastic collisions which caused further energy spreads. However the main assumption was that if the mean energy peak remained sharp during moderation the neutrons could be considered as monoenergetic. The uncertainty due to elastic degradation was estimated by the following argument (Beghian).

The distance travelled by a neutron with velocity v in a time T (the life time in the iron) would be vT cm, so that if λ_{tr} is the transport mean free path, the average number of collisions suffered would merely be

$$\overline{n} = vT/\lambda_{tr} \qquad 5.9$$

Now if $\overline{\xi}$ is the average lethargy change per collision, then

$$\overline{n}\ \overline{\xi} = \ln (E_o/E) \qquad 5.10$$

$\overline{\xi}$ is to remain constant in the small interval $\Delta E = E_o - E$

$$\Delta E = E_o(1 - e^{-\overline{n}\ \overline{\xi}}) \qquad 5.11$$

The expression for $\overline{\xi}$ is

$$\bar{\xi} = (2/A)/(1 + \bar{\mu}_o) \qquad 5.12$$

with A = 56 the atomic mass number of the iron.

For E_n = 2.427 MeV, v ≃ 2 x 10^9 cm/sec, Σ^{tr} ≃ 0.13 (I. Langner et al.), $\bar{\mu}_o$ ≃ 0.37 and T ≃ 4 x 10^{-9} sec (calculated and averaged over the two sizes). This gives $\bar{n}$ = 1 and $\bar{\xi}$ ≃ 0.026 so that ΔE = 0.063. The average neutron energy in the block was threfore $\bar{E}_n$ = 2.395 ± 0.038 MeV.

For E_n = 1.285, v ≃ 1.5 x 10^9 cm/sec, Σ^{tr} ≃ 0.16 (A.B. Smith et al.), $\bar{\mu}_o$ ≃ 0.2 and T ≃ 1.2 x 10^{-8} sec giving $\bar{n}$ ≃ 2.9 and $\bar{\xi}$ ≃ 0.03. Thus ΔE = 0.106 and $\bar{E}_n$ = 1.232 ± 0.059 MeV.

5.3 THE INTEGRAL PROTON SPECTRUM

Since energy selection was to be made, it was worthwhile to have a fair idea of the fraction of the energy spectrum which was to be used for this purpose. The integral spectrum at each energy was obtained; the lack of a fast amplifier stretcher made it difficult for the differential spectrum to be observed on the M.C.P.H.A. which would only properly analyse pulses that had been stretched to more than 0.3 μs. The ideal recoil proton spectrum has a rectangular probability distribution

$$\left.\begin{aligned} P(E_p)\, dE_p &= dE_p/E_n \;;\quad 0 \leq E_p \leq E_n \\ &= 0 \qquad\qquad E_p > E_n \end{aligned}\right\} \qquad 5.13$$

and a corresponding integrated spectrum

$$I_p(B) = I_o \{1 - B/E_n\} \qquad 5.14$$

where $I_p(B)$ is the total number of knock-on protons with a bias energy B applied. I_o is the total number of protons and is given by

$$I_o = \phi_n(E_n)\, C\, \sigma_{n,p}(E_n) \qquad 5.15$$

where $\phi_n(E_n)$ is the flux of monoenergetic neutrons, C is the hydrogen concentration in the phosphor and $\sigma_{n,p}(E_n)$ is the (n,p) cross-section (barns) at E_n. The ideal light output from the detector would have a similar straight-line distribution as 5.13

$$L(V) = L_o \{1 - V/V_{max}\} \qquad 5.16$$

where L refers to the number of pulses, V_{max} is the maximum pulse height and V the bias voltage. However the light output is not a linear function of the proton recoil energy because of quenching effects whereby the primary excitation is suppressed by the high density of ionized and excited molecules. The result of this is a preponderance of small pulses so that the integral spectrum becomes concave. In addition to this the finite energy resolution of the detector will give it a tail. Second order effects such as end- and wall-effects, scattering on carbon and multiple scattering will further distort the spectrum. These have been thoroughly discussed in Fast Neutron Physics; they were very small and have been ignored.

A concave spectrum implied that the fraction of the energy spectrum which had been discriminated off would in fact be much greater than what the actual bias voltage setting suggested. To correct for this (i.e. to 'push' the spectrum back into a straight line) Birks has proposed a semi-empirical relation between the light output and proton energy which is

$$dL/dE_p = A/(1 + kB\ dE_p/dx) \qquad 5.17$$

A is a constant of the scintillator and includes the absolute efficiency; k and B are parameters describing the amount of non-linear response (quenching) present; x is the proton range in the phosphor. Equation 5.17, when integrated, would give the corrected number of pulses at the proton energy E_p.

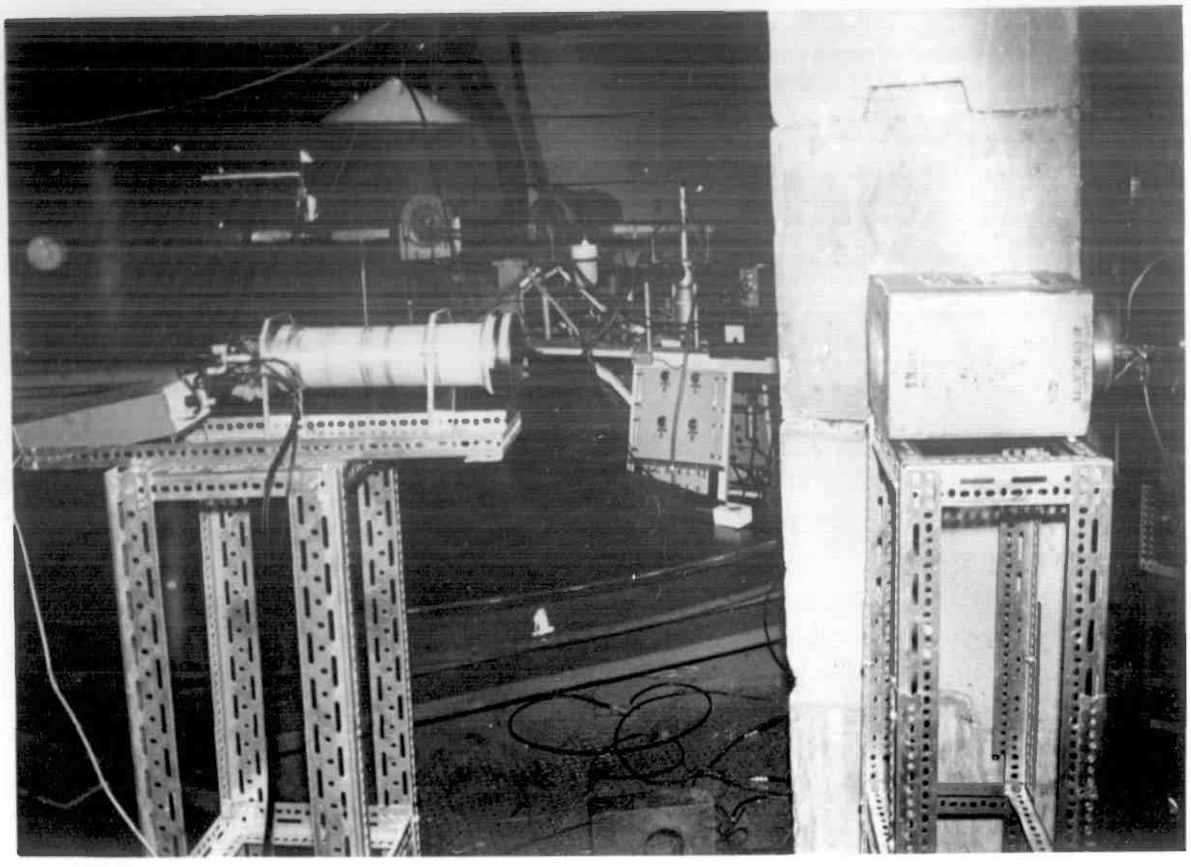
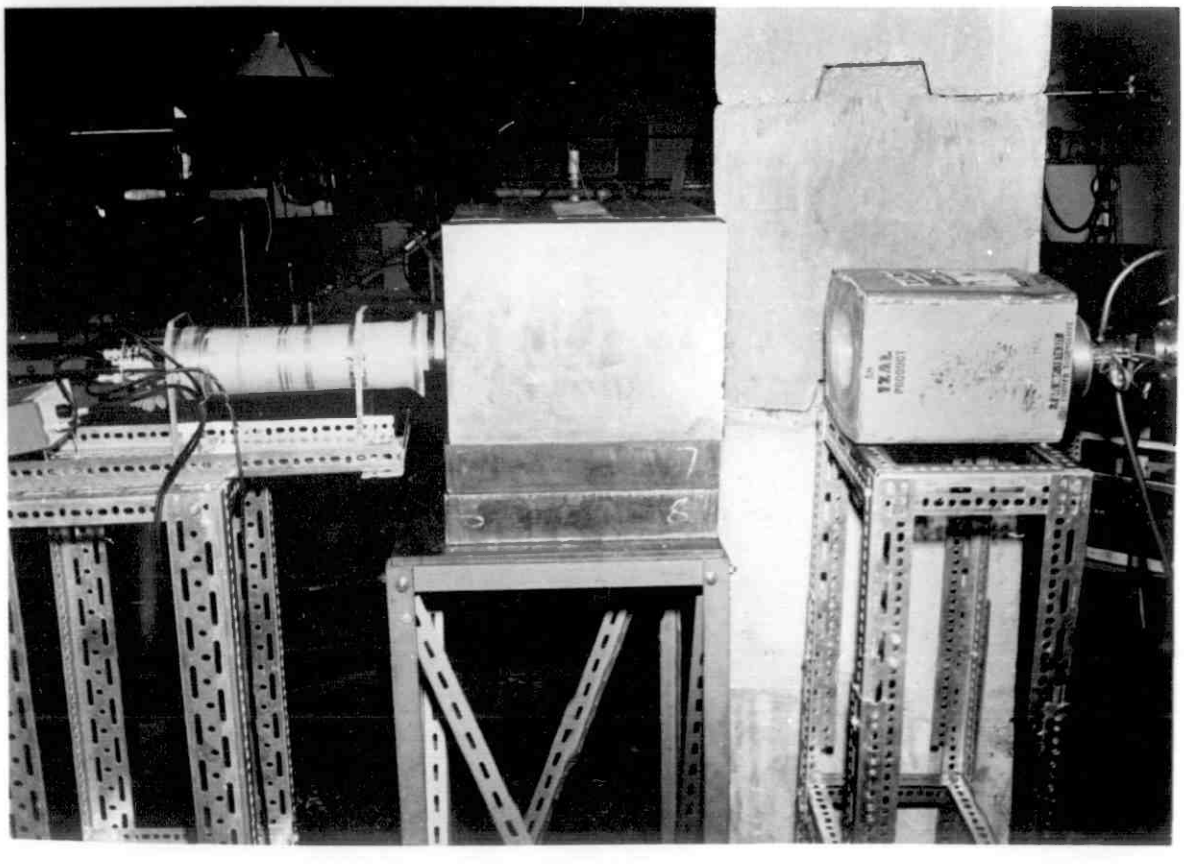


PLATE 1 DETECTOR-TARGET SET UP

PLATE 2 IN LINE DECAY MEASUREMENT



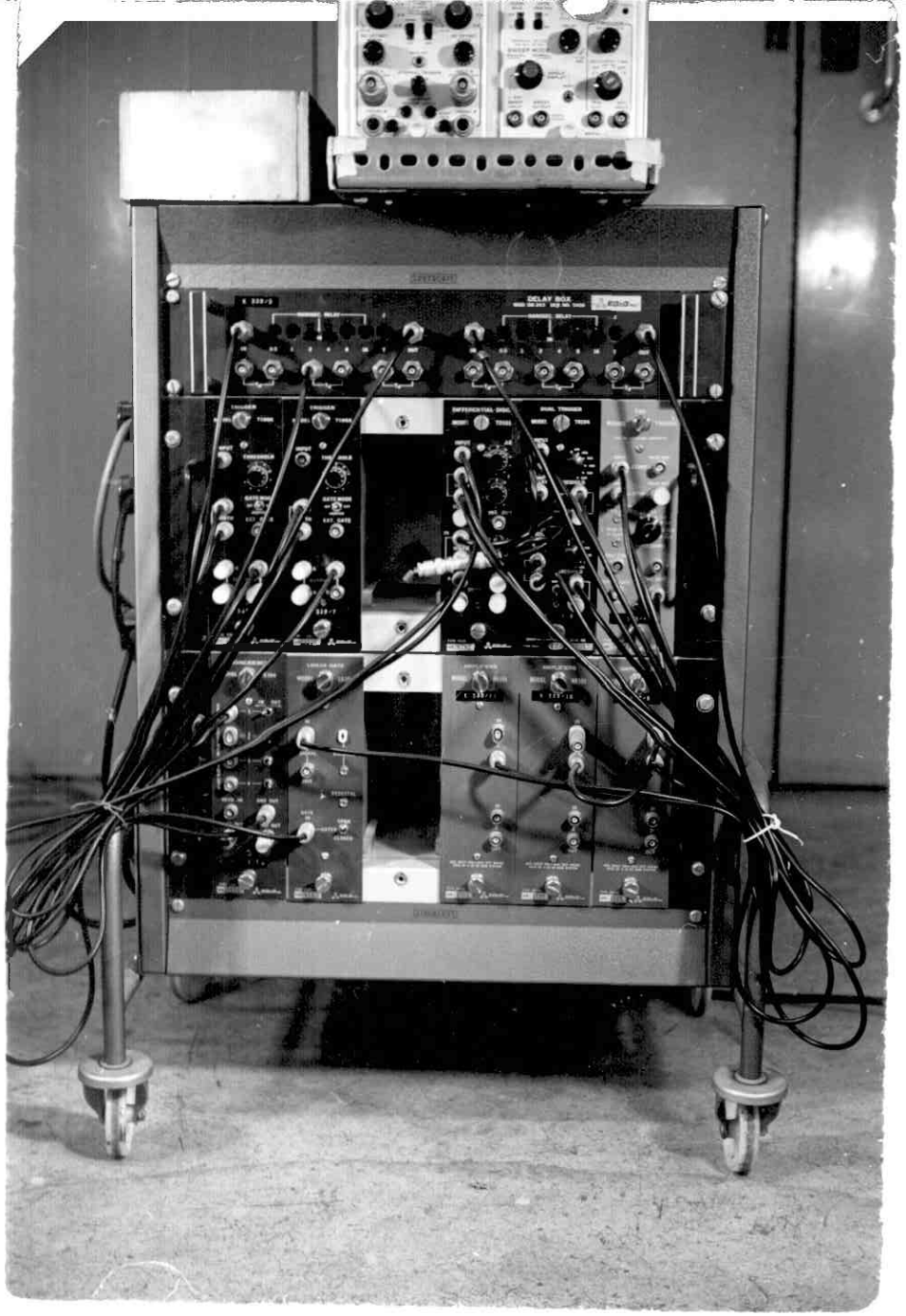


PLATE 4 FAST ELECTRONIC EQUIPMENT

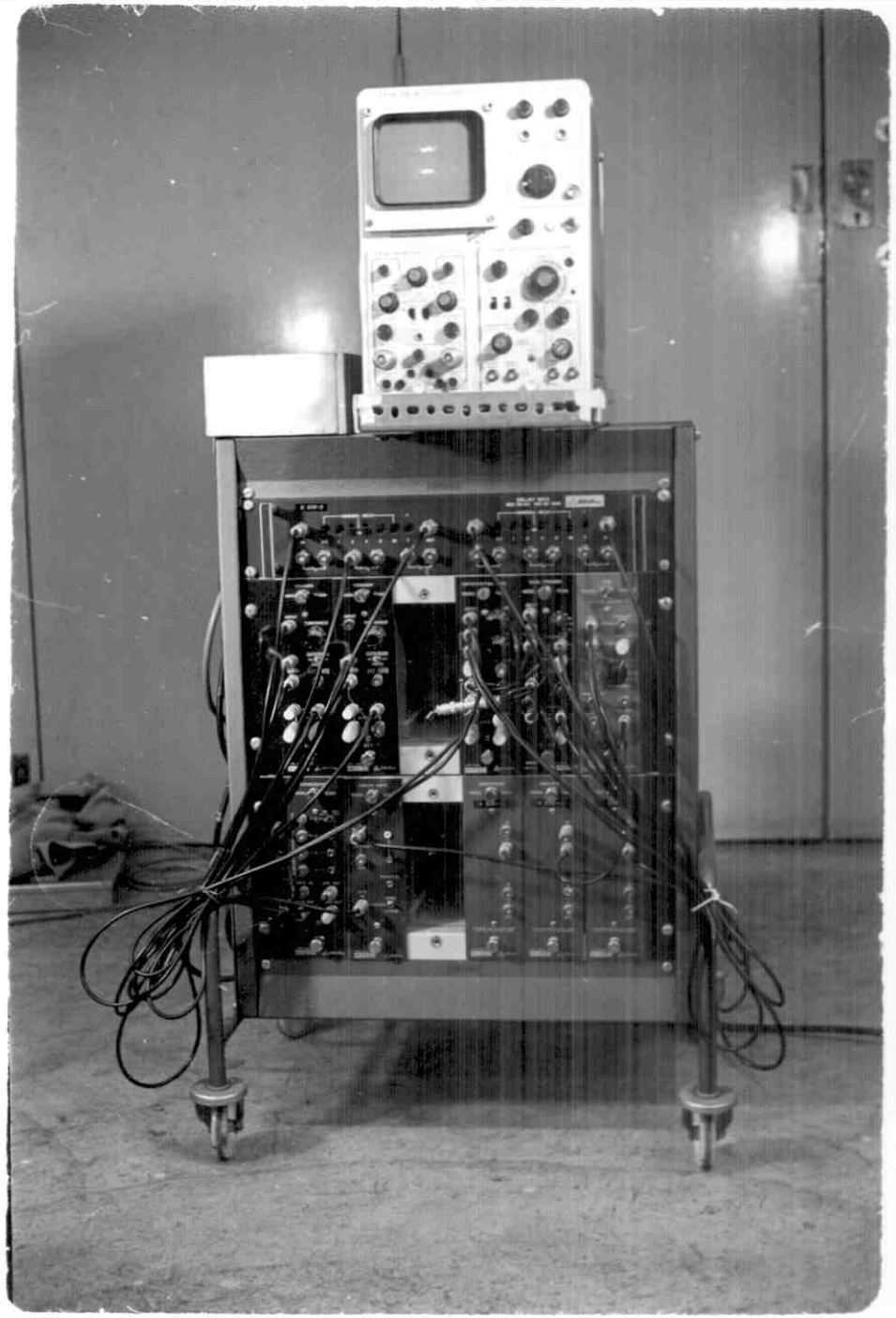


PLATE 5 EQUIPMENT WITH 'SCOPE

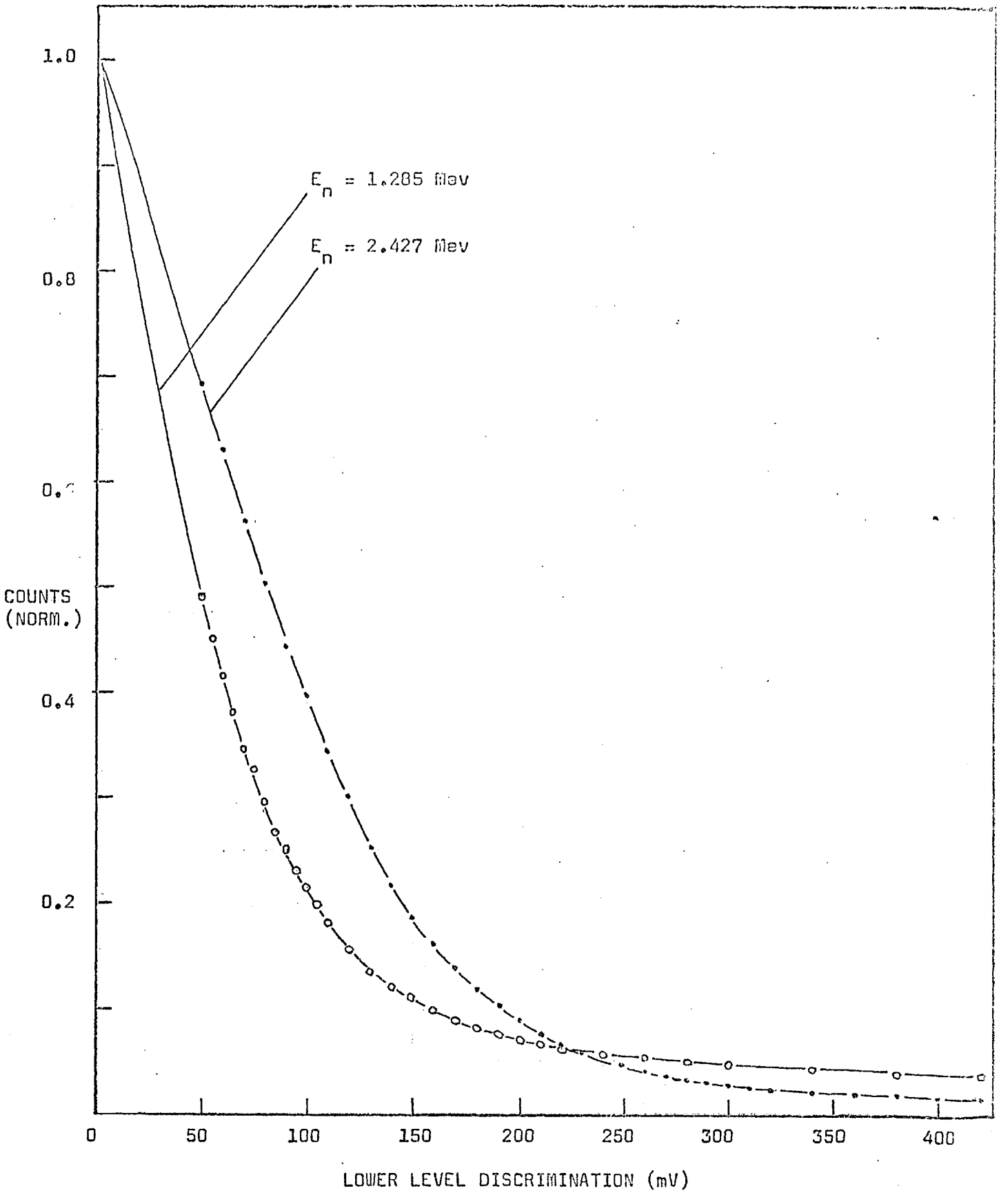


FIGURE 5.10 THE PROTON INTEGRAL SPECTRA

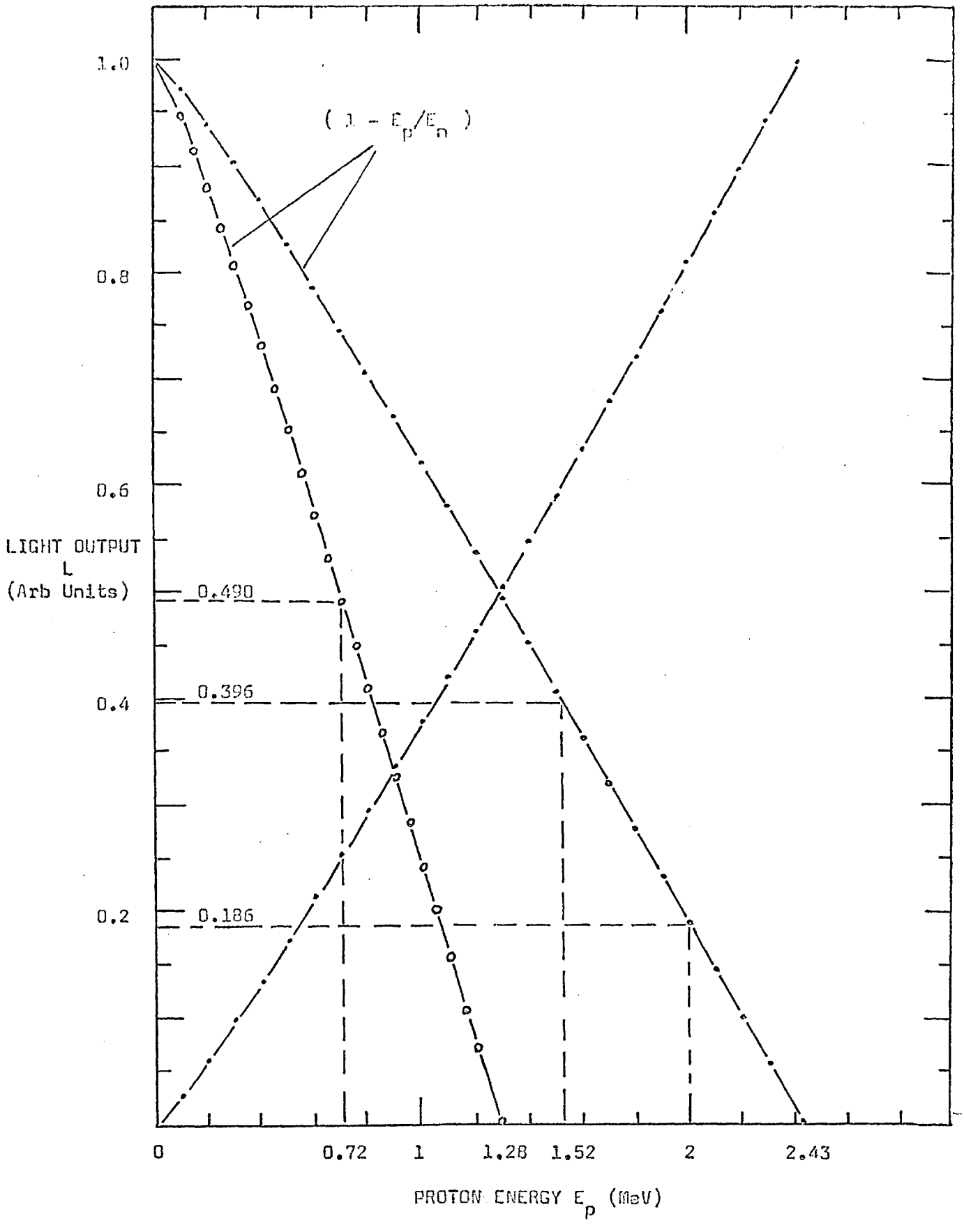
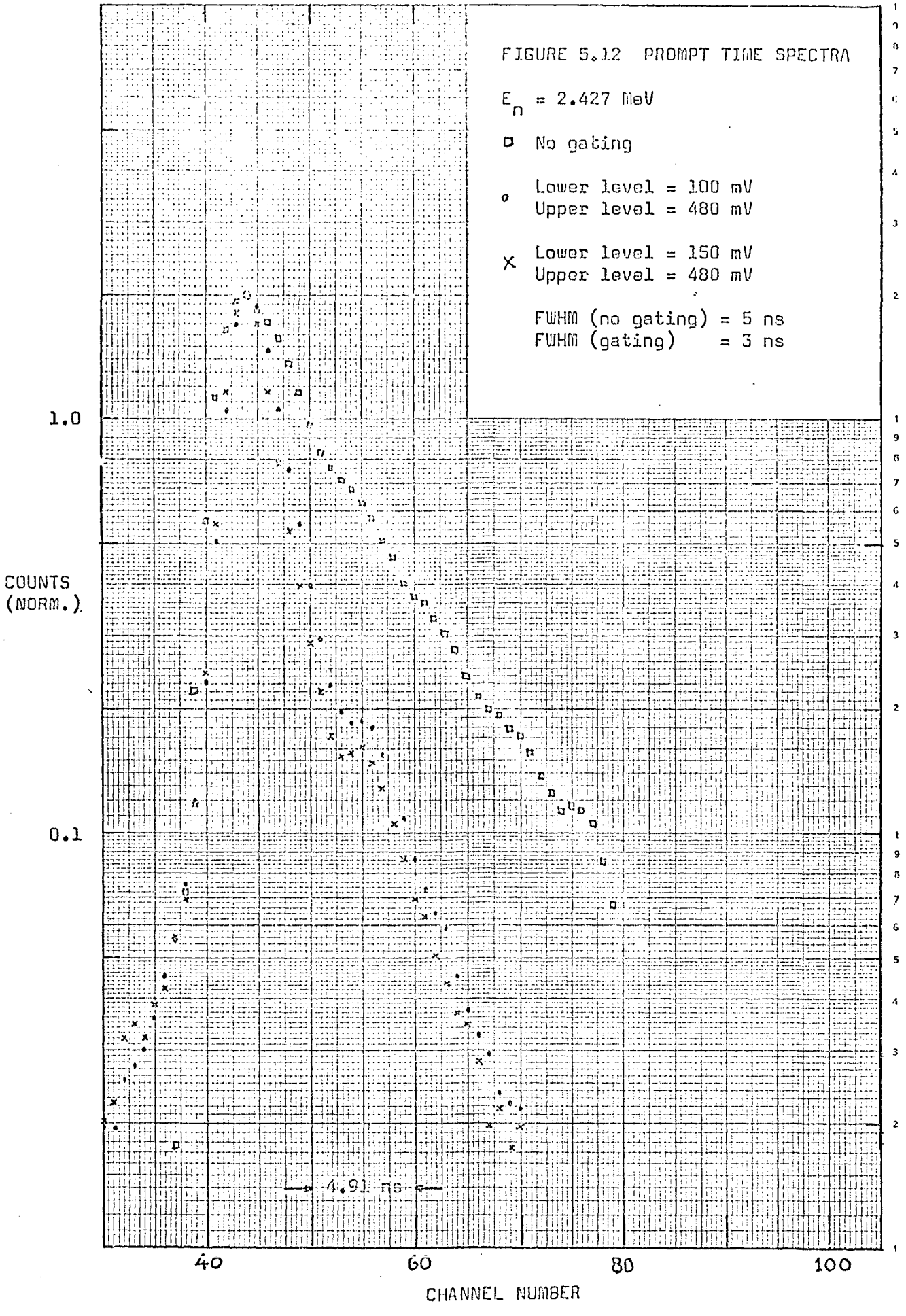


FIGURE 5.11 CORRECTION FOR THE PROTON INTEGRAL SPECTRUM


FIGURE 5.12 PROMPT TIME SPECTRA
E_n = 2.427 MeV
No gating
Lower level = 100 mV
Upper level = 480 mV
Lower level = 150 mV
Upper level = 480 mV
FWHM (no gating) = 5 ns
FWHM (gating) = 3 ns
1.0
0.1
COUNTS
(NORM.)
4.91 ns
40
60
80
100
CHANNEL NUMBER

The integration was carried out numerically using Simpson's Rule from $E_p = 0$ in steps of 100 keV up to $E_p = 1.285$ MeV and 2.427 MeV which were the selected neutron energies. A was normalized and the value of $kB = 0.0091$ gm cm^{-2} MeV^{-1} (Prescott and Rupaal) for NE 104 was adopted. The range-energy curve for proton in NE 104 was given by Nuclear Enterprises. When fitted using LEEFIT it was found to obey the approximate relation

$$dE_p/dx \simeq 8.75\ x^{-0.3} \qquad 5.18$$

for E_p from 0.1 up to 3 MeV; E_p was in MeV and x in gm cm^{-2}. (cf. Birks $dE_p/dx = 17.91\ x^{-0.443}$ for E_p from 1 to 150 MeV.) Fig. 5.11 shows the corrected integral spectra obtained. They are only approximately linear in view of the above assumptions and adopted values.

For obtaining the integral spectra the detector was placed about 1 metre from the target with the collimator in position but with the iron slabs and table removed. The dynode pulses were fed into the energy selection circuit (Fig. 5.4) which was operated in the discrimination mode (lower level E only). The stretched output was fed into an amplifier and then to a fast scaler (Harwell 2000). The bias voltage was increased from 50 mV in small steps usually of 10 mV until the counts were low. Counting time was that taken to integrate 400 μCoulombs at the target (approx. 60 secs). At $E_n = 2.427$ MeV the E.H.T. was set at 2400∅ volts whilst at $E_n = 1.285$ MeV it was increased to 2500∅ volts. This was done to slightly increase the pulse heights of the smaller energy neutrons. The counts were about 2×10^5 for the lowest (50 mV) bias and decreased by a factor of about 100 at 500 mV. The curve of counts vs. bias setting were extrapolated back to zero bias since 50 mV was the lowest possible setting. Assuming the equivalent counting time was 60 seconds the spectra were corrected for the 1 μs dead time of the amplifier and scaler. Fig. 5.10 shows the normalized spectra obtained.

The curves have rather long tails because of the presence of large pulses due to the target gammas which, although resolvable in terms of time, were not separable from the neutrons in energy. A comparison of the intensities of the gamma and neutron peaks (see later) showed that the gamma pulses could form as high as 8% of the total counts. It should be remembered that a gamma ray with the same energy as the neutrons can give a pulse several times larger than that due to the neutrons. However, for the purpose of estimating the bias energy corresponding to a particular voltage discrimination the uncertainty could be tolerated.

The ratio of the counts at a given voltage setting (say 100 mV) to that at zero bias was obtained. The energy which would give this same ratio in light output was then read off from the corrected graphs (Fig. 5.11). Thus at E_n = 2.427 MeV a 100 mV bias was equivalent to a 62% energy cut-off. It was decided to set the upper level to 480 mV where the counts fell to 1% of the maximum. If this corresponded to E_n, then 100 mV bias (uncorrected) would only be 21% of the upper level.

5.4 THE PROMPT NEUTRON TIME SPECTRUM

Prior to measuring the neutron decays, the prompt time spectra were obtained in order to determine their shapes, the time resolution and to illustrate the separation between neutron and target gamma peaks by time-of-flight. Table 5.2 below gives the various settings and results.

Detector distance from target:- 96 cm; Time disc:- 100 mV

Converter (TAC):- 0 - 100 ns range

Analyzer(MCP11A):- input amplification 5.5; 200 channels;

back bias; 0 V; 40 mV/ch giving 0.491 ns/ch

Upper level discrimination:- 480 mV

EHT:- 2.4 kV (E_n = 2.427 MeV); 2.5 kV (E_n = 1.285 MeV)

Counting time:- 15 minutes (E_n = 2.427 MeV); 21 minutes (E_n = 1.285 MeV)

Neutron Energy E_n MeV	Gating (mV lower level)	Maximum Counts	Position of peak (Channel no.)	Average Background
2.427	0	80749	49	2000
	50	56125	44	615
	100	43834	44	337
	150	23203	44	217
1.285	0	43242	53	2400
	50	20209	49	552
	100	7440	48	210
	150	2239	47	102

TABLE 5.2 SETTINGS AND RESULTS FOR PROMPT TIME SPECTRA

The slower time-of-flight of the proton and neutron beams in the case of the lower energy spectrum necessitated an offsetting relative delay of about 10 metres of 50 Ω cables (about 60 ns) in order to bring back the spectrum into the display screen. Figs. 5.12 and 5.13 give the normalised prompt time spectra with background subtracted and corrected for the 50 μs dead time of the converter. The F.W.H.M. for the high energy spectrum with no gating was 10 channels (5 ns) and gating improved this down to 6 channels (3 ns) which compared favourably with

the expected time resolution of 4 ns due to the proton pulse width. The lower energy spectrum had a slightly wider resolution, the ungated F.W. H.M. being 12 channels (6 ns) and the gated one about 9 channels (4.5 ns). This was attributed to the increased uncertainty in the time-of-flight as given by

$$\frac{dt}{t} = -\frac{1}{2}\frac{dE}{E} \qquad 5.19$$

the worsening being about 1 ns. Energy gating sharpened the peak considerably and the peak position shifted back by 4 or 5 channels. "Bumps" could be seen on the spectra at both energies. They occurred at about 12 channels (6 ns) from the peak in the high energy spectrum and at around 15 to 20 cha nels (7 - 10 ns) from the peak in the lower energy one. This strongly suggested the presence of room return neutrons especially from the huge concrete wall adjacent to the target-detector set up; this can be seen in Plates 5.1 and 5.2. The significance of these bumps will become apparent in the analysis of the decay spectra and will be discussed later.

To get the target gamma peak into the picture, the neutron peak was pushed up to the right of the analyzer display by switching the converter to the 0 - 300 ns range and back biasing the analyzer by 2 volts. The channel width was set at 0.506 ns. Figs. 5.14 and 5.15 show the peaks at E_n = 2.427 MeV. They were separated by about 91 channels (46 ns). The time-of-flight of the gamma rays over 96 cm is 3.2 ns and that of 2.427 MeV neutrons is 44.54 ns, giving a difference of 41.34 ns. The ratio of gamma peak intensity to that of the neutron (in the ungated mode) was about 0.08.

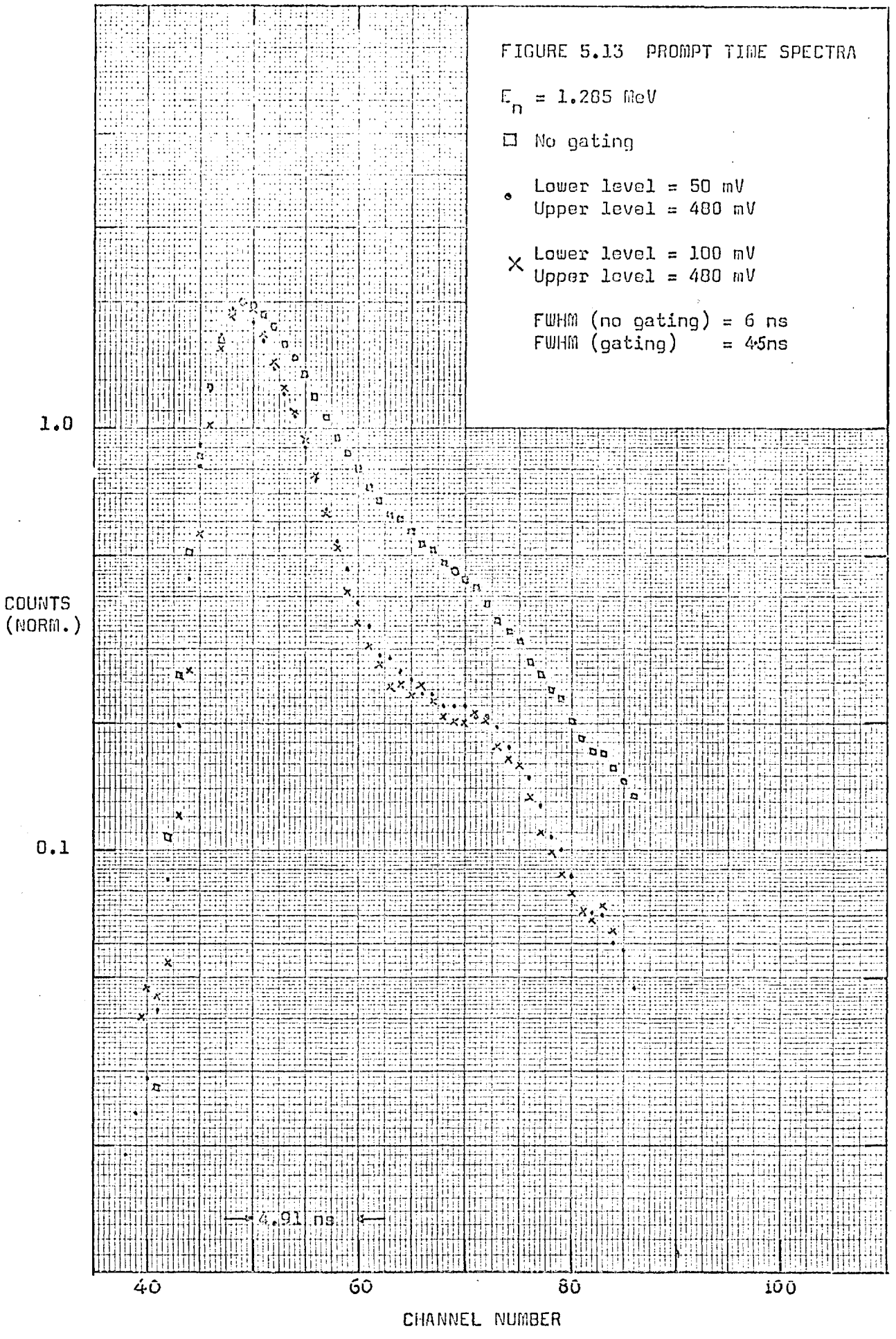

FIGURE 5.13 PROMPT TIME SPECTRA
E_n = 1.285 MeV
No gating
Lower level = 50 mV
Upper level = 480 mV
Lower level = 100 mV
Upper level = 480 mV
FWHM (no gating) = 6 ns
FWHM (gating) = 4.5ns
1.0
0.1
COUNTS (NORM.)
4.91 ns
40
60
80
100
CHANNEL NUMBER

FIGURE 5.14 TIME OF FLIGHT SEPARATION BETWEEN THE PROMPT NEUTRON SPECTRUM AND TARGET GAMMAS PEAK

E_n = 2.427 Mev Lower level gating = 0 mV

Difference between peaks = 90 channels = 45.54 ns

Neutron t.o.f over 96 cms = 44.54 ns ; Gamma t.o.f = 3.2 ns

Difference = 41.34 ns

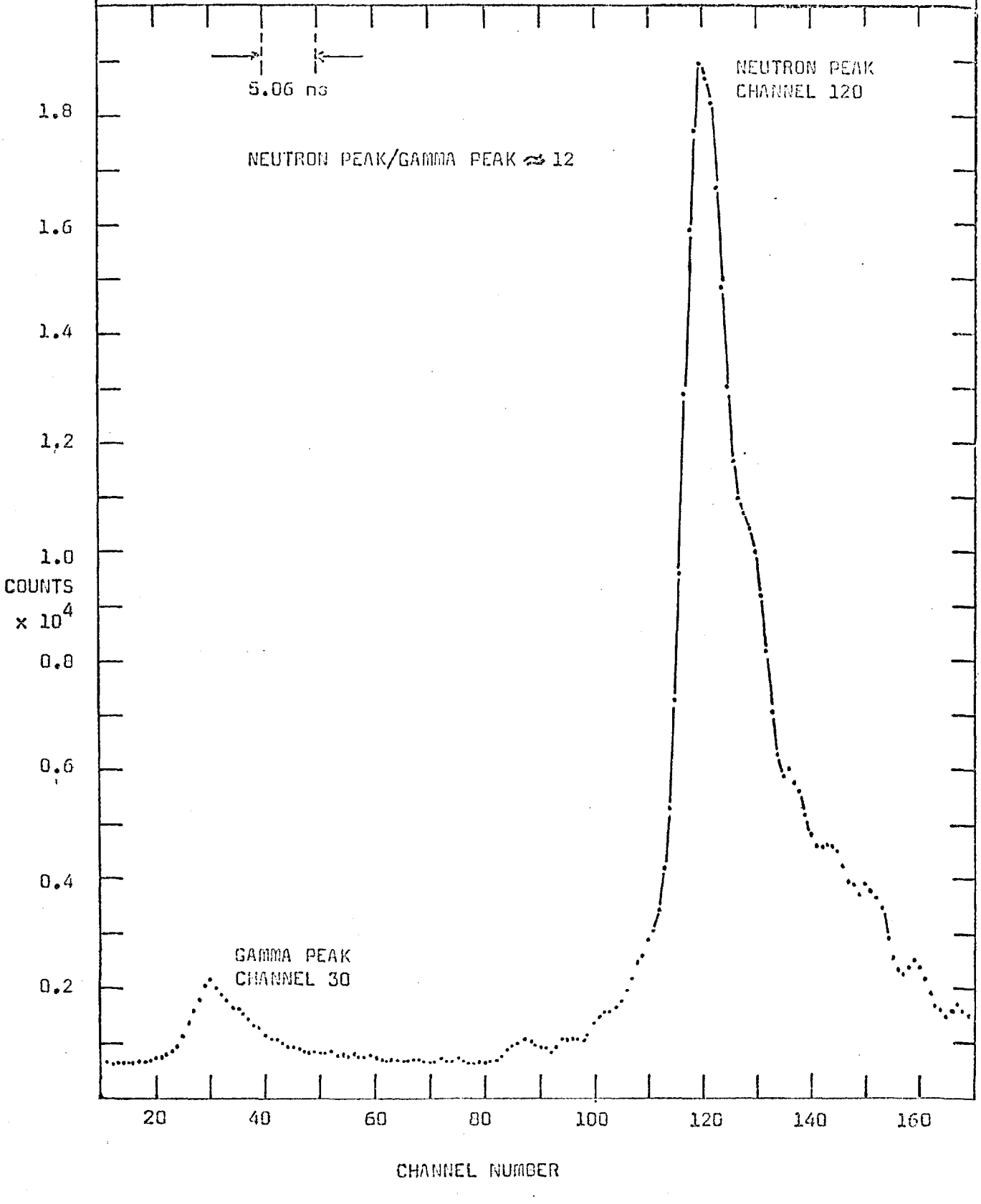
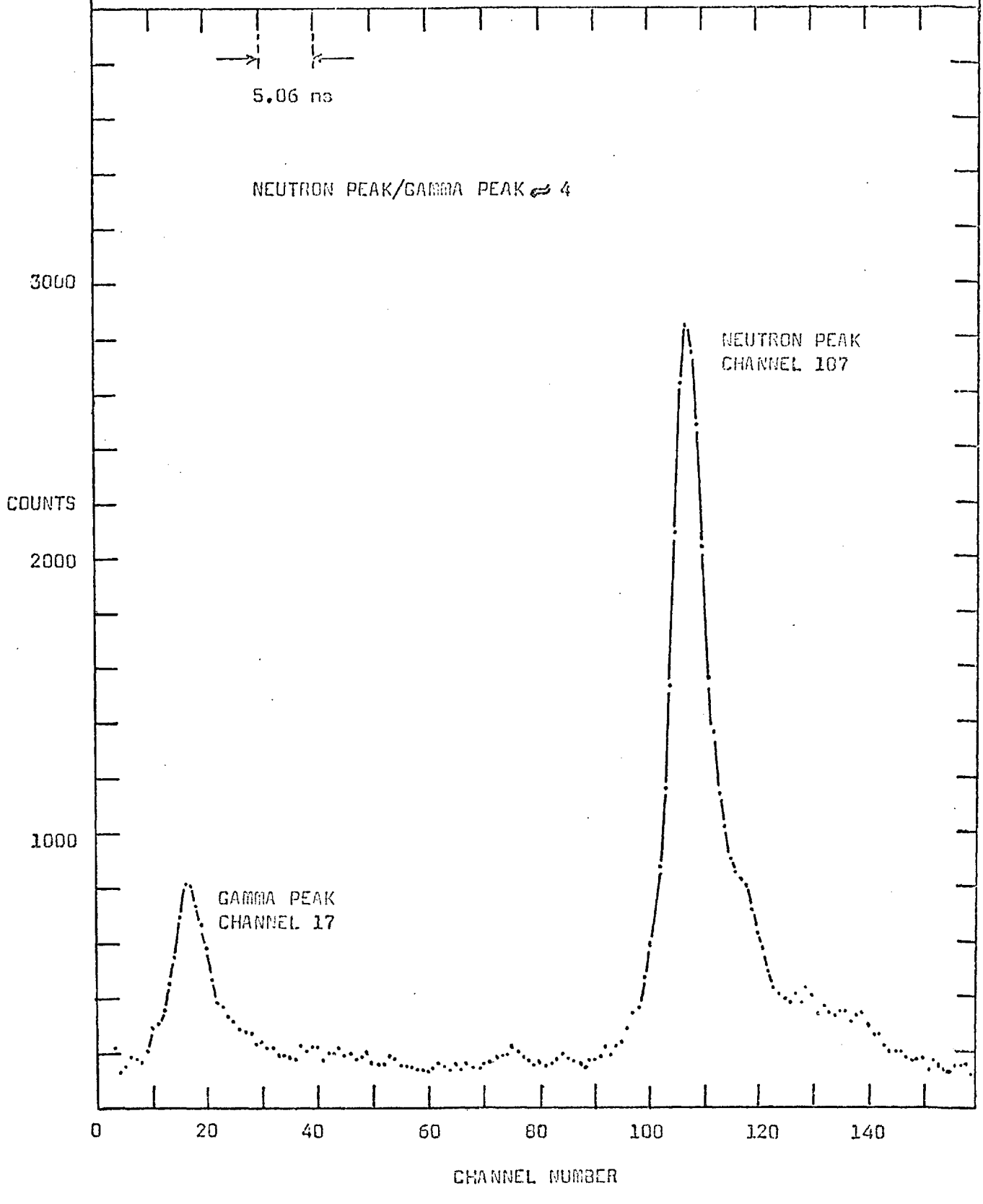
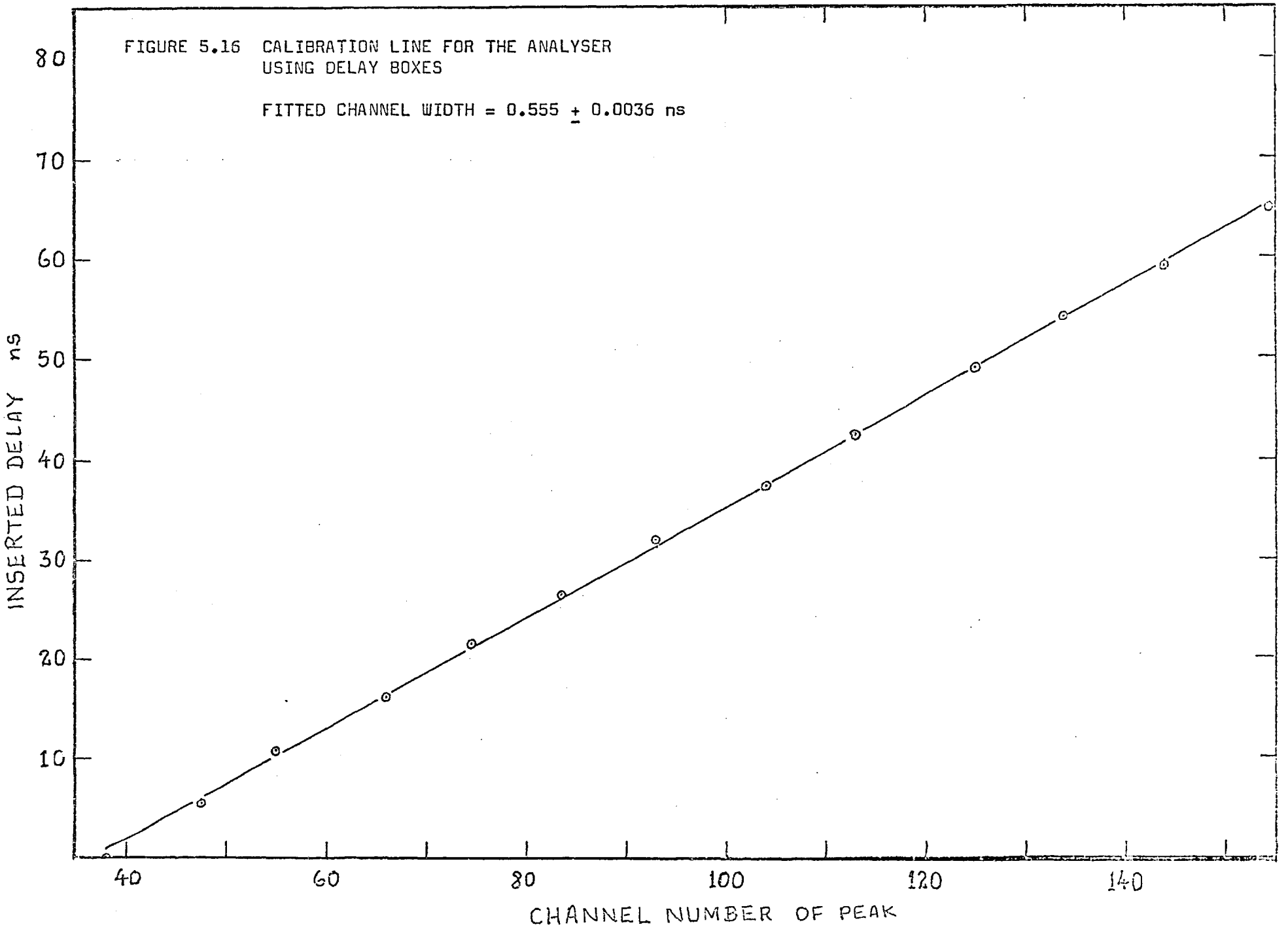


FIGURE 5.15 TIME OF FLIGHT SEPARATION BETWEEN THE PROMPT NEUTRON SPECTRUM AND TARGET GAMMAS PEAK

E_n = 2.427 Mev Lower level gating = 200 mV




FIGURE 5.16 CALIBRATION LINE FOR THE ANALYSER USING DELAY BOXES
FITTED CHANNEL WIDTH = 0.555 ± 0.0036 ns
INSERTED DELAY ns
10
20
30
40
50
60
70
80
40
60
80
100
120
140
CHANNEL NUMBER OF PEAK

5.5 NEUTRON DECAY MEASUREMENTS

The iron slabs were put in position on the table and centred with respect to the proton beam. For each buckling measurements were made at the two selected energies with the detector in the inline and then the perpendicular position. For the inline measurement the detector was placed about 1 cm from the centre of the surface on the far side from the target whilst for the latter case it was placed close to the centre of a surface normal to the beam. Table 5.3 shows the settings and operating conditions of the experiment.

EHT: 2.4 kV (2.427 MeV); 2.5 kV (1.285 MeV)
Anode amplification: 4 X; Dynode amplification: 10 X
Pick-up signal amplification; 16 X
Time signal disc: 100 mV
Converter (TAC) range: 0 → 300 ns
Analyzer (MCPHA): input amplification 15 X
sensitivity 40 mV/channel
channel width 0.54 ns/channel
channels used 200
back bias 1.5 volts
Average proton current:- 1.2 - 2 μA

TABLE 5.3 OPERATING CONDITIONS FOR NEUTRON DECAYS

Tables 5.4 and 5.5 give the various measurements made. After each measurement a print out of the decay spectrum was obtained. The whole experiment was performed within a period of four days.

DIMENSIONS
12" x 12" x 12"

DISTANCE OF DETECTOR FROM TARGET
90 cm (in line); 74 cm (perp.)

Injection Energy E_n MeV		Energy Gating (mV) E	E + ΔE	Maximum Counts	Counting time	Inserted delays
2.427	IN	100	400	2440	2 hrs 15 min	103 ns
	LINE	100	480	1745	2 hrs	103
	PERP	100	480	2375	1 hr	105
		150	480	2110	2 hrs	105
1.285	IN	50	480	2261	2 hrs 10 min	25
	LINE					
	PERP	50	480	2922	1 hr 55 min	30

TABLE 5.4 MEASUREMENTS WITH 12" x 12" x 12" BLOCK

DIMENSIONS
15" x 15" x 18"

DISTANCE OF DETECTOR FROM TARGET
89 cm (in line); 69 cm (perp.)

Injection Energy E_n MeV		Energy Gating (mV) E	E + ΔE	Maximum Counts	Counting time	Inserted delays
2.427	IN	100	480	1143	2 hrs 55 min	101 ns
	LINE					
	PERP	100	480	2398	2 hrs	105
		150	480	1823	2 hrs 25 min	105
1.285	IN	50	480	2039	2 hrs 30 min	17
	LINE					
	PERP	50	480	2282	1 hr 50 min	25

TABLE 5.5 MEASUREMENTS WITH 15" x 15" x 18" BLOCK

The spectra were shifted well to the right of the display screen so that background in the distant channels could be observed. Two small

spurious peaks came out of the background. These were found to be in channels 143 and 159 and were independent of energy, buckling, position of detector and energy gating which implied that they could well be instrumental in origin (due to either the analyzing side or to the Van de Graaff). The calculated value of 0.54 ns for the channel width was based on the result obtained in Chapter 4 with the converter range switched to 300 ns and the analyzer amplification and sensitivity changed. As a check against any instrumental errors when settings were altered the analyzer was calibrated against inserted delays. With the settings the same as for the decay measurements, a photomultiplier anode pulse was split with one pulse delayed with respect to the other and both were fed into the converter. The output was then fed into the analyzer and the position of the peaks for various delays was observed and printed out. A linear fit of delay against channel number was made and shown in Fig. 5.16. A value of 0.555 ± 0.004 ns/ch was obtained. However in view of the highly unreliable values of the inserted delays, this value was not adopted. For example quoted values of 30 and 60 ns when measured on the Tektronix 5614 Scope gave readings of 33 and 64 ns respectively. This calibration experiment merely showed that there were no serious electronic drifts as the settings were altered. For the high energy measurements (E_n = 2.395 MeV) gatings of 100 mV and 150 mV corresponded to cut-off energies of 1.52 and 2.00 MeV respectively whilst for the low energy measurements (E_n = 1.232 MeV) a gating of 50 mV corresponded to a bias energy of 0.72 MeV.

CHAPTER 6

ANALYSIS OF NEUTRON DECAY DATA

6.1 ANALYSIS PART I

The raw data were not corrected for dead time since the count rates were very low, less than one count per second even for the largest counts. The decay spectra were fed into the programme LEEFIT and fitted to a single exponential plus background according to the equation

$$C = C_o e^{-\lambda N} + B \qquad 6.1$$

where C and C_o are counts, N is the channel number, and λ is the decay constant, and B is the background. For each fit more than 100 points were used, the two spurious peaks in the background (mentioned earlier) being excluded. Guess values of C_o, λ and B were fed in and in all cases the fitting procedure converged after about 4 iterations. Typical tolerances were 2, 0.00005, and 1 for C_o, λ and B respectively. Standard deviations for these parameters were calculated and so was the "test of goodness" parameter defined as

$$\overline{\chi^2} = \sum_{i=1}^{n} \left[\frac{(C_i^t - C_i^o)}{C_i^o}\right] / (n-1) \qquad 6.2$$

where C_i^t is the calculated value, C_i^o the input value and n the number of points fitted.

The manner in which λ, B and $\overline{\chi^2}$ varied as points from the front (decay peak) were successively dropped was investigated, this being done to find the effects of spatial harmonics and background. Figs. 6.12 to 6.16 show some of the results obtained. Both λ and $\overline{\chi^2}$ did not seem to behave consistently although B remained reasonably constant throughout. On the basis of spatial effects only one would expect λ to converge to a constant value for both the in line and perpendicular spectra. However

it would appear that the rather high background also had a significant perturbation on λ, this effect becoming increasingly dominant as more points were dropped. Moreover the relatively low statistics would have an appreciable effect on the variation of $\overline{\chi}^2$. Figs. 6.1 to 6.11 show the neutron decay curves with the background subtracted. The criterion adopted in plotting out the fitted curves was to take the point corresponding to a decrease in $\overline{\chi}^2$ as the first front point. Spatial harmonics are discernible in the high energy, large buckling (small size) in line decays (Figs. 6.1 and 6.2) although they are not so apparent in the others. The time decay constants were obtained by dividing the slope by the channel width of 0.540 ns. The results are given in Table 6.5 and are compared with theoretical calculations.

6.2 COMPARISON WITH THEORETICAL CALCULATIONS

The cross-sections input used for the calculations were taken from data sets of A.B. Smith (1965), Nishimura et al. (1965) and Langner et al. (1968). The energy resolution of these up-to-date data is fine, being of the order of 20 keV or less. Point cross-sections were used since a one-velocity model was adopted. The iron slabs have the composition shown in Table 6.1. The impurities amounted to 1.226% and since the data for some of these were not reliable only iron cross-sections were used. It should be noted that the largest impurity, manganese ~~copper~~, has cross-sections similar to that of iron. Errors due to omitting the impurities would therefore be very small. In the DSN method the variation of decay with space intervals and S_n order was investigated and Table 6.2 shows that the decay was highly insensitive to the choice of space intervals and S_n order. For all other calculations 30 mesh intervals and n = 16 were used. To test the effect of the "buckling absorption" correction for the finite transverse sides,

the variation of λ with the different sides was also found and again the errors were very small.

The cross-sections were regarded as anisotropic to first order (transport correction), the non-elastic processes being isotropic. Keeping the total cross-section and the capture cross-section constant, various values of the time decay constants at the two energies and two bucklings were calculated as the non-elastic cross-section was increased by fixed percentages. The results are shown in Tables 6.3 and 6.4. The reason why the total rather than the self-scatter elastic cross-section was kept constant is because the former data is generally regarded as more reliable. Both the numerical and the analytical values are shown. At the worst, the discrepancy between the two was no more than 1%. Since the expansion method is better suited for cases where measurements with a reasonable number of bucklings could be made, the DSN results were taken for comparison with the experimental decays of the present project.

In all cases there was no agreement between theory and experiment if the non-elastic cross-section σ^{ne} was unchanged. The experimental values were all much lower than theoretical predictions. However there was some semblance of agreement if σ^{ne} was reduced by as much as 20% in the low energy and 50% in the high energy calculations. On examination of the decay curves it could be seen that some of the curves have "humps" (Figs. 6.5, 6.8, 6.9 and 6.10) which occur at about 40 channels from the peaks. This suggests that room return neutrons could be a source of errors in the fitted curves. In order to find out the contribution from this source and the effect of the high background the data were re-analysed.

E_n = 1.230 σ^t = 2.733 b; σ^c = 0.003 b; $\bar{\mu}_o$ = 0.2

σ^{ne} = 0.3304 b;

DIMENSION 12" x 12" x 12.5"

30 mesh intervals n = 16

N ORDER	DECAY x 10^8 SEC^{-1}	NO. OF INTERVALS	DECAY x 10^8 SEC^{-1}
4	0.9559	30	0.9562
8	0.9562	40	0.9561
16	0.9562	60	0.9561

DIMENSION	12" x 12" x 12.5"	15" x 15" x 18.5"	
SIDE (CM)	DECAY x $10^8 SEC^{-1}$	SIDE (CM)	DECAY x 10^8 SEC^{-1}
30.48	0.9562	38.10	0.7683
31.75	0.9568	47.00	0.7702

TABLE 6.2 VARIATION OF DECAY WITH SPACE INTERVALS, S_N ORDER AND SIDES.

IRON BS 15 (1961) FIRST GRADE

CONSTITUENT	% CONCENTRATION	DENSITY x 10^{24}atoms/cc
IRON	98.774	0.0847
CARBON	0.192	0.0838
MANGANESE	0.628	0.0789
NICKEL	0.086	0.0913
COPPER	0.200	0.0843
SULPHUR	0.060	-
PHOSPHORUS	0.060	-

TABLE 6.1 COMPOSITION OF THE IRON SLABS USED.

E_n = 2.39 MeV; σ^t = 3.20 b; σ^c = 0.001 b; $\bar{\mu}_o$ = 0.4

(DATA FROM NISHIMURA ET AL.)

DIMENSION 12" x 12" x 12.5"

σ^{ne} (barns)	% change (decrease)	THEORETICAL DECAYS x 10^8 sec^{-1}		
		DSN METHOD	$v\Sigma^{ne}_g + vDB^2_g$	CB^4_g
0.765	0	2.121	2.128	0.019
0.689	10	1.984	2.005	0.021
0.462	40	1.573	1.608	0.026
0.386	50	1.436	1.481	0.028
DIMENSION 15" x 15" x 18.5"				
0.765	0	1.858	1.865	0.008
0.689	10	1.721	1.734	0.009
0.462	40	1.310	1.341	0.011
0.386	50	1.173	1.210	0.012

E_n = 2.40 MeV; σ^t = 3.2 b; σ^c = 0.003; $\bar{\mu}_o$ = 0.365

(DATA FROM LANGNER ET AL.)

DIMENSION 12" x 12" x 12.5"

0.948	0	2.422	2.391	0.015
0.474	50	1.600	1.602	0.022
0.427	55	1.518	1.521	0.024
0.379	60	1.436	1.446	0.026
DIMENSION 15" x 15" x 18.5"				
0.948	0	2.167	2.163	0.007
0.474	50	1.335	1.341	0.010
0.427	55	1.253	1.258	0.010
0.379	60	1.170	1.182	0.011

TABLE 6.3 THEORETICAL DECAYS AT 2.395 MeV

E_n = 1.230; σ^t = 2.733 b; σ^c = 0.003 b; $\bar{\mu}_o$ = 0.2

(DATA FROM A.B. SMITH)

DIMENSION 12" x 12" x 12.5"

σ^{ne} (barns)	% change (decrease)	THEORETICAL DECAYS x 10^8 sec^{-1}		
		DSN METHOD	$v\Sigma^{ne} + vDB_g^2$	CB_g^4
0.3300	0	0.9562	0.9551	0.0181
0.2970	10	0.9141	0.9161	0.0185
0.2640	20	0.8720	0.8770	0.0189
DIMENSION 15" x 15" x 18.5"				
0.3300	0	0.7683	0.7698	0.0076
0.2970	10	0.7262	0.7292	0.0077
0.2640	20	0.6841	0.6889	0.0079

E_n = 1.235 MeV; σ^t = 2.320 b; σ^c = 0.0024 b; $\bar{\mu}_o$ = 0.131

(DATA FROM LANGNER ET AL.)

DIMENSION 12" x 12" x 12.5"

0.3530	0	1.0124	0.9968	0.0204
0.3354	5	0.9898	0.9762	0.0206
0.3177	10	0.9673	0.9555	0.0209
0.3001	15	0.9447	0.9348	0.0211
DIMENSION 15" x 15" x 18.5"				
0.3530	0	0.8177	0.8108	0.0087
0.3354	5	0.7950	0.7911	0.0087
0.3177	10	0.7723	0.7673	0.0088
0.3001	15	0.7496	0.7456	0.0089

TABLE 6.4 THEORETICAL DECAYS AT 1.23 MeV

$E_n = 2.395 \pm .038$ MeV — DIMENSION 12" x 12" x 12.5"

GATING (MV)		POSITION	DECAY x 10^8 sec^{-1}		
			EXPONENTIAL WITH BACKGROUND	SINGLE EXPONENTIAL (NO "HUMP)	SINGLE EXPONENTIAL (BKGD+ 10%)
E + ΔE	400	IN LINE	$1.428 \pm 4\%$	-	$1.831 \pm 3\%$
E	100				
	480	IN LINE	$1.457 \pm 4\%$	-	$1.817 \pm 3\%$
	100				
	480	PERP.	$1.100 \pm 3\%$	-	$1.180 \pm 2\%$
	100				
	480	PERP.	$0.890 \pm 4\%$	-	$1.340 \pm 4\%$
	150				
			DIMENSION 15" x 15" x 18.5"		
	480	IN LINE	$0.974 \pm 4\%$	-	$1.200 \pm 3\%$
	100				
	480	PERP.	$0.939 \pm 4\%$	$1.026 \pm 2\%$	$1.157 \pm 2\%$
	100				
	480	PERP.	$0.931 \pm 5\%$	$1.074 \pm 3\%$	$1.187 \pm 3\%$
	150				

TABLE 6.5 FITTED DECAYS AT 2.395 MeV

$E_n = 1.232 \pm 0.059$ MeV — DIMENSION 12" x 12" x 12.5"

GATING (MV)		POSITION	DECAY x 10^8 sec^{-1}		
			EXPONENTIAL WITH BACKGROUND	SINGLE EXPONENTIAL (NO "HUMP")	SINGLE EXPONENTIAL (BKGD+ 10%)
E + ΔE	480	IN LINE	$0.851 \pm 4\%$	$0.951 \pm 2\%$	$0.976 \pm 2\%$
	50				
	480	PERP.	$0.781 \pm 5\%$	-	$0.878 \pm 3\%$
	50				
			DIMENSION 15" x 15" x 18.5"		
	480	IN LINE	$0.571 \pm 5\%$	$0.709 \pm 2\%$	$0.758 \pm 2\%$
	50				
	480	PERP.	$0.489 \pm 5\%$	-	$0.515 \pm 2\%$
	50				

TABLE 6.6 FITTED DECAYS AT 1.232 MeV

6.3 ANALYSIS PART II

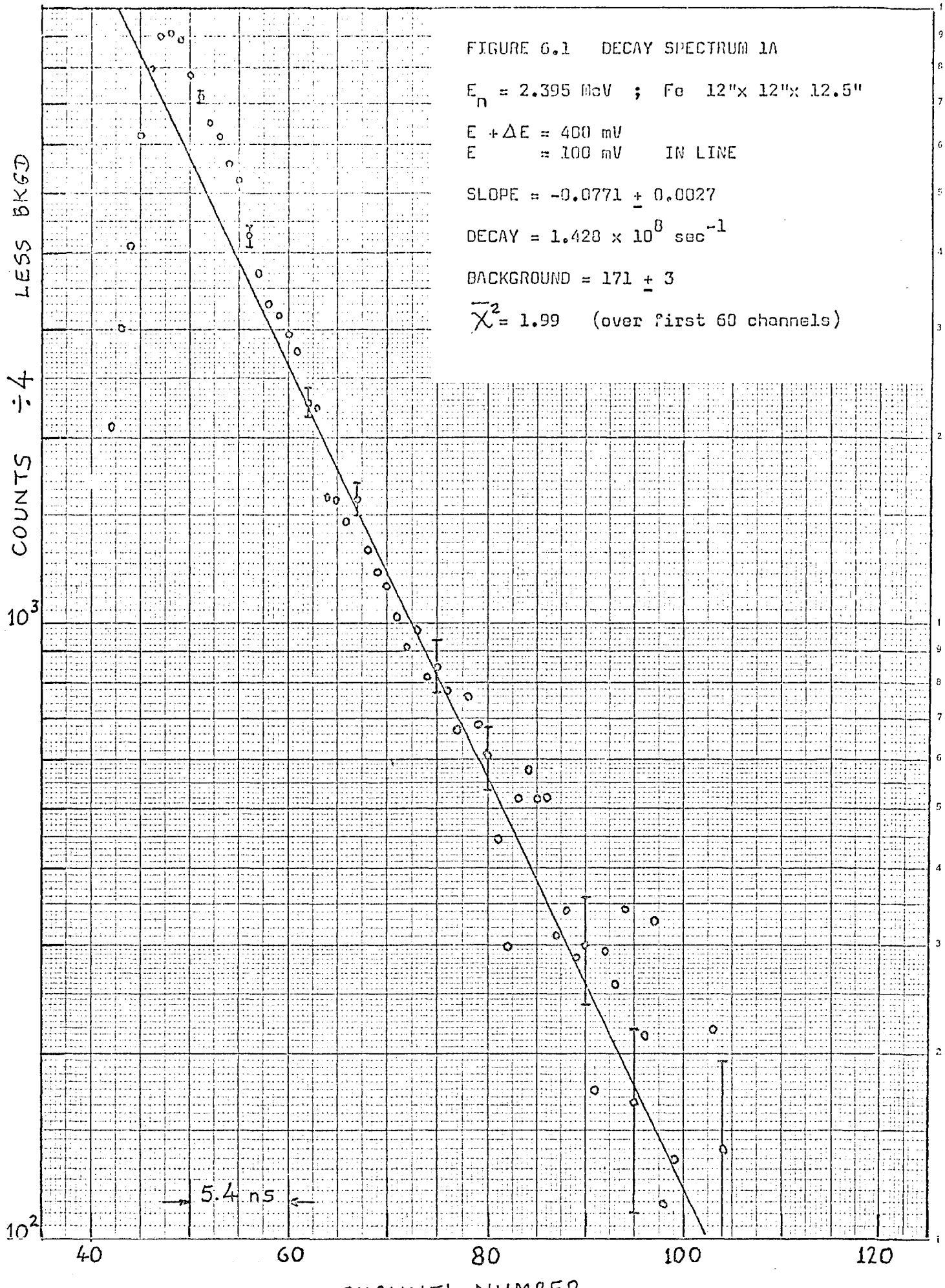
Whenever the "humps" are apparent the data of the decay spectra were fitted to a single exponential without the background obtained from the first analysis. The humps were excluded so that only the first 40 points were fitted. This procedure was applied to Figs. 6.5, 6.8, 6.9 and 6.10. The results are shown in the second decay column of Tables 6.5 and 6.6. There was a marked increase in the value of the decay especially in the low energy case where the increase was greater than 10%. The background from the fitting procedure could be uncertain by an appreciable amount particularly if a time-dependent background was present. To find the effect of this uncertainty the background was increased by 10% and all the spectra were then fitted to a single exponential with the new background subtracted from the data. The results are shown in the third decay column of Tables 6.5 and 6.6. Again the decays showed an increase of as much as 10%. It should be noted that the errors in the fitted decays were unaffected by the procedures adopted in the second part of the analysis. In fact they were slightly improved. This shows that the low statistics and uncertain background were such that the slopes could be altered significantly without affecting the errors.

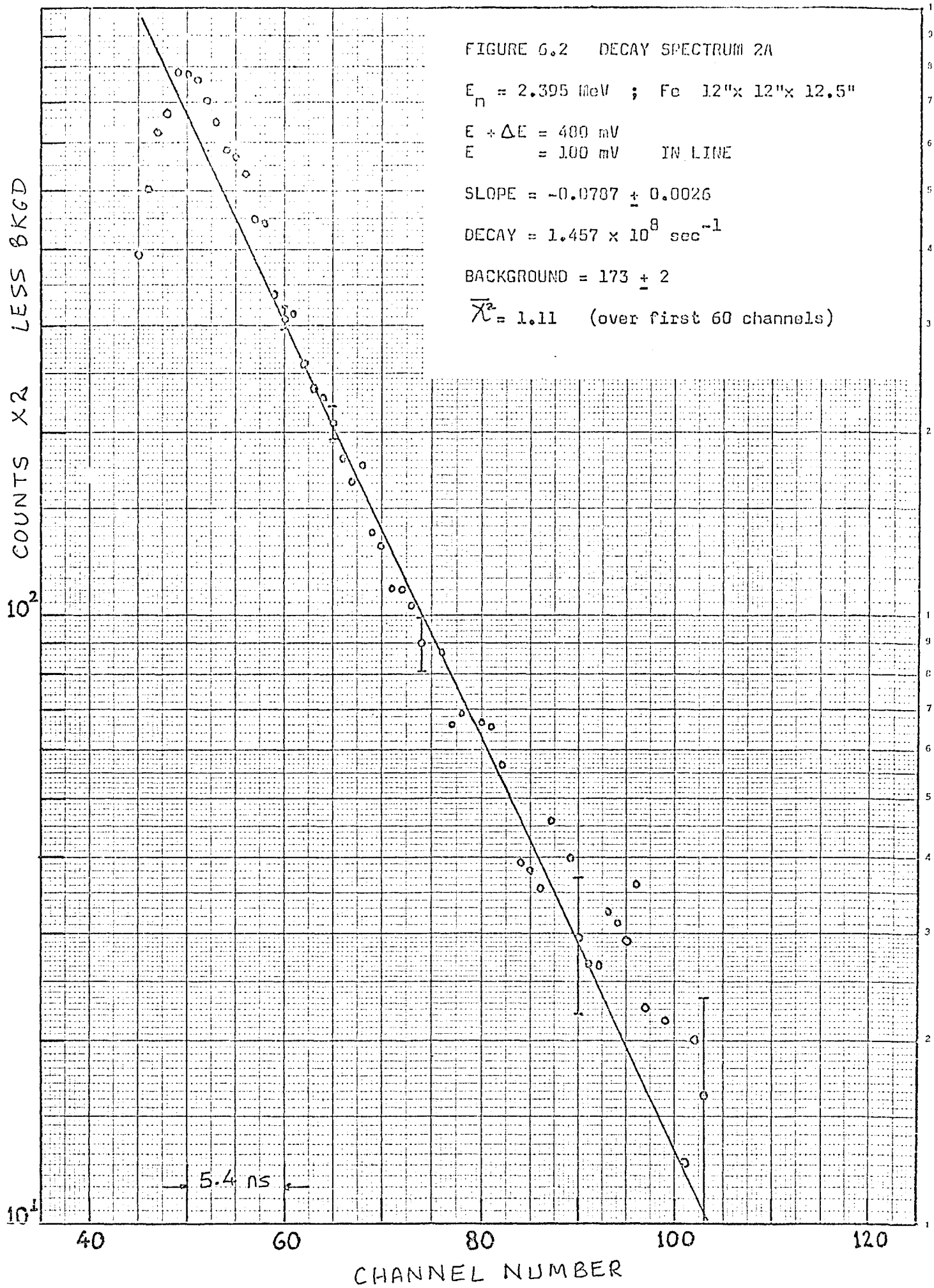
For the high energy decays the room return neutrons were apparent only in the small buckling (large size) perpendicular measurements. In the case of the small buckling the results were quite consistent for both the in line and perpendicular decays and they did not show a great change on reanalysis. Certainly the values of 1.2, 1.157 and 1.187 ($\times 10^8$ sec^{-1}) seem to agree with the theoretical value of 1.173 with σ^{ne} = 0.386 barns, (a decrease of 50%) for Nishimura's data and 1.170 with σ^{ne} = 0.379 barns (a decrease of 60%) for Langner's data. In the case of the large buckling the in line decays were far higher than the

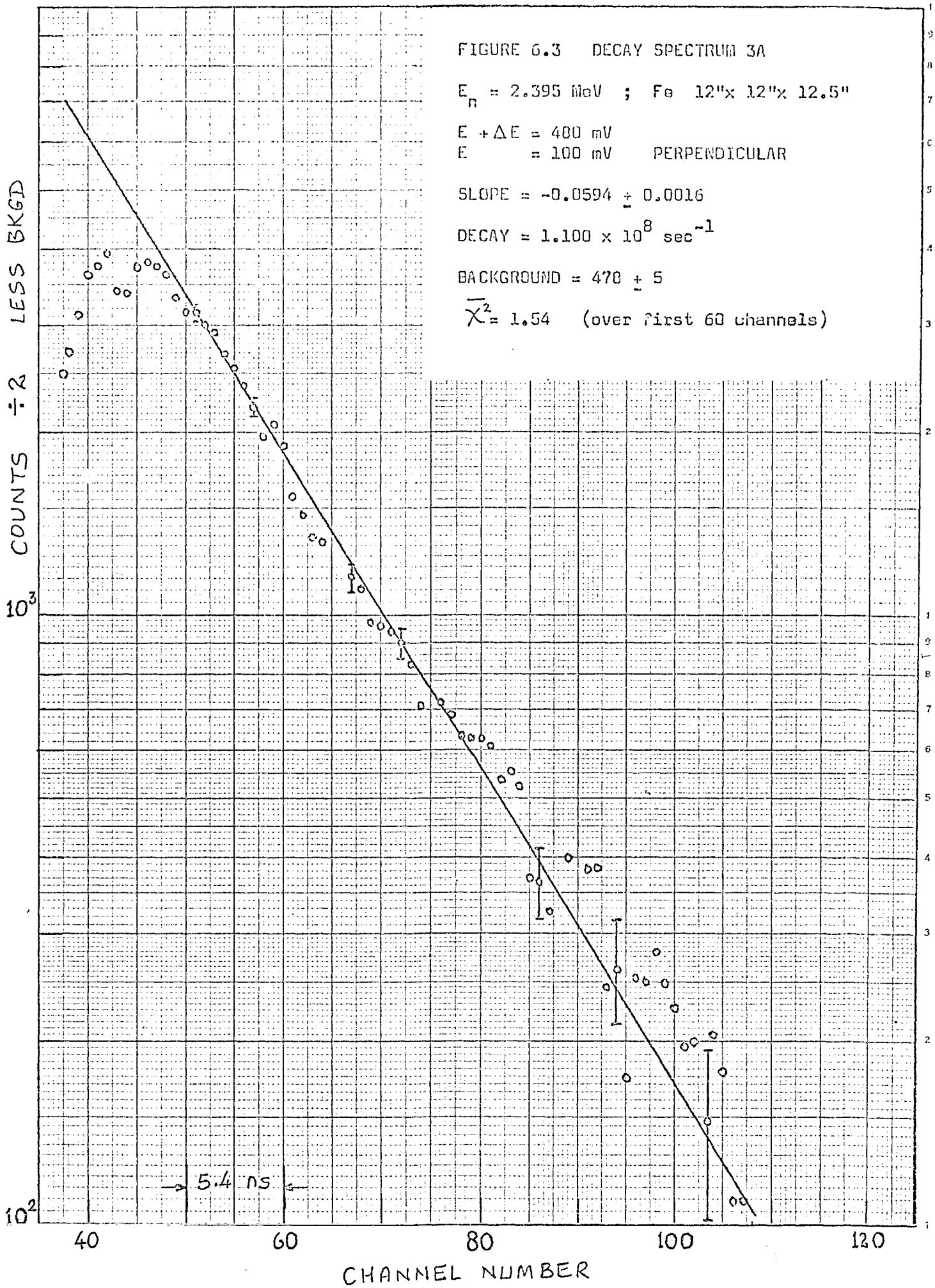
perpendicular decays although the two in line decays agreed well with each other. Raising the background by 10% increased the values by about 30% so that it would appear that these results were greatly affected by background and statistics and this could account for the discrepancy in the values. The values of 1.428 and 1.457 ($\times 10^8$ sec^{-1}) obtained from the first analysis for the in line decays compare favourably with the calculated values of 1.436 with σ^{ne} = 0.386 barn and 1.436 with σ^{ne} = 0.379 barn.

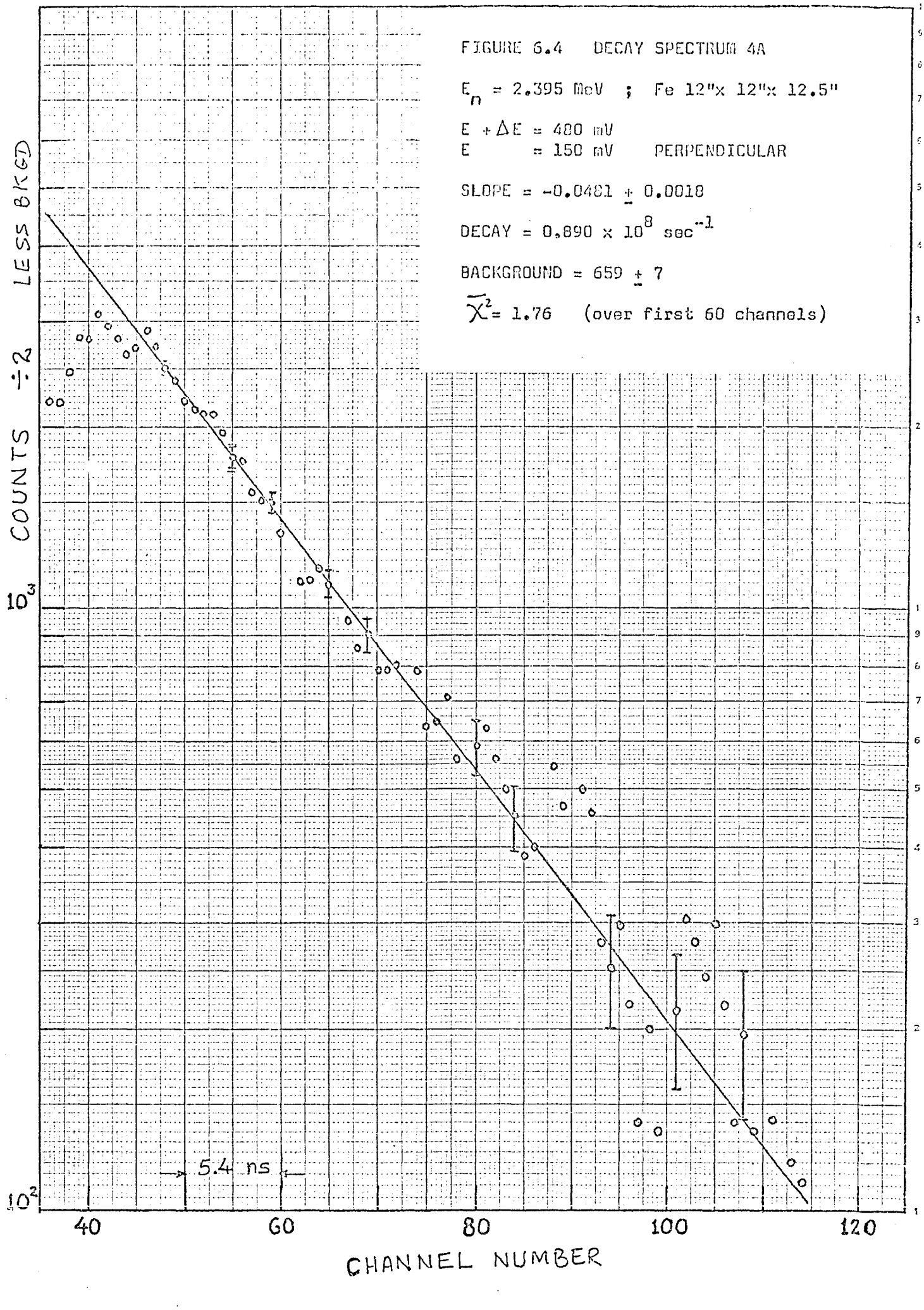
For the low energy decays the room returns were quite distinct in the in line measurements with both bucklings (Figs. 6.5 and 6.10). The perpendicular measurements gave much lower values for the decays. Re-analysis increased the values by over 10% for the large buckling and 30% for the in line measurement with the small buckling. It would seem to suggest that the perpendicular decays were heavily contaminated with both room returns and background build up since even the in line results showed the room returns which were not observable in the corresponding cases at the high energy. The in line value of 0.951 ($\times 10^{-8}$ sec^{-1}) for the large buckling is to be compared with the theoretical value of 0.956 with σ^{ne} = 0.33 barn (no change) for Smith's data and 0.9447 with σ^{ne} = 0.3001 barn (15% decrease) for Langner's data. For the small buckling the in line decay is 0.709 whilst the calculation yielded 0.7262 with σ^{ne} = 0.297 barn (10% decrease) for Smith's data and 0.7496 with σ^{ne} = 0.3001 barn (15% decrease) for Langner's data.

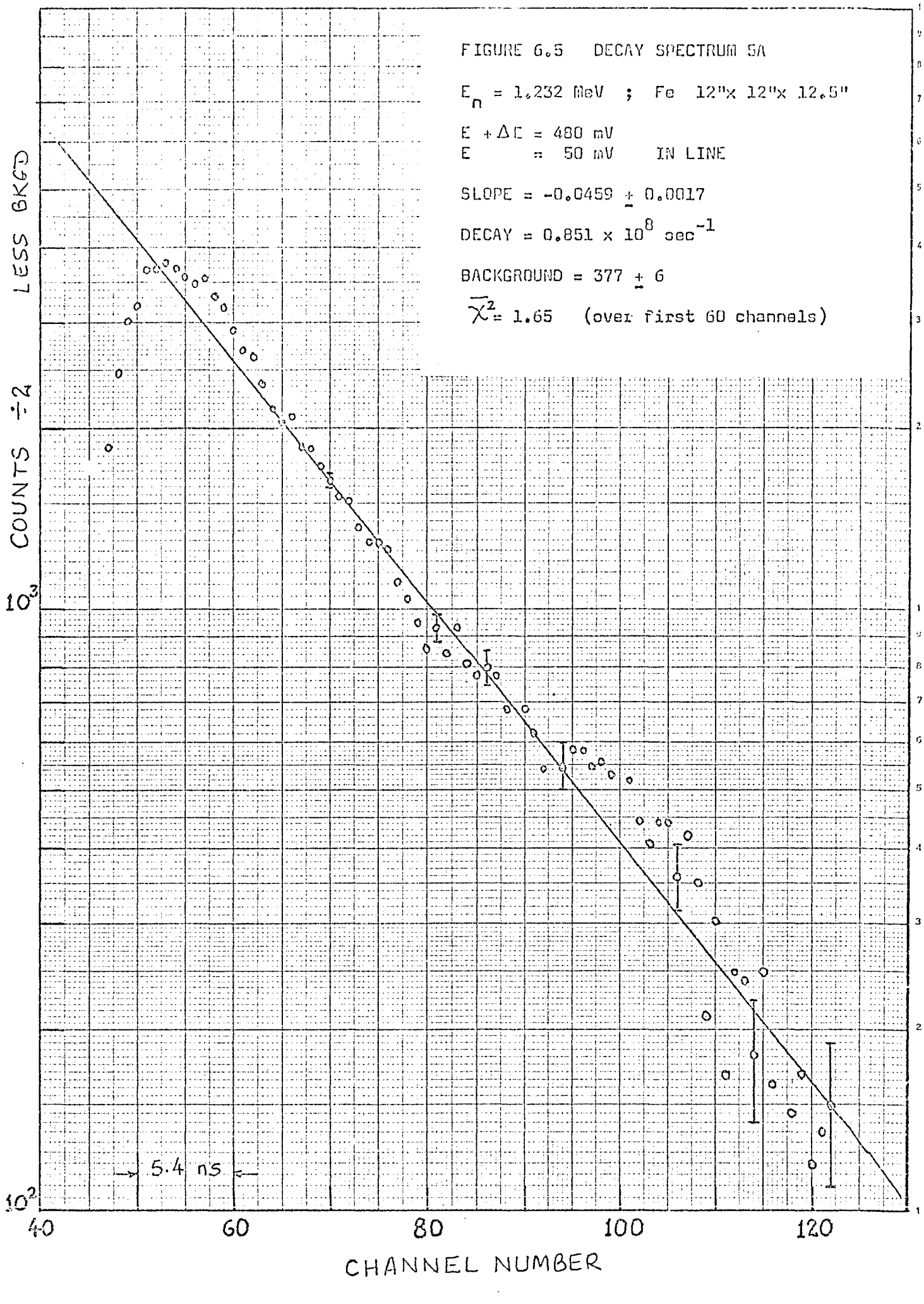
The errors in the actual fitted decays amounted to 5% whilst contributions from background and room returns were at least 10% so that an accuracy of not less than $\pm$ 15% was possible under the circumstances. The errors in the total cross-sections and $\bar{\mu}_o$ were not quoted but it is usually reasonable to assume an error of 5% for these data (Beghian).

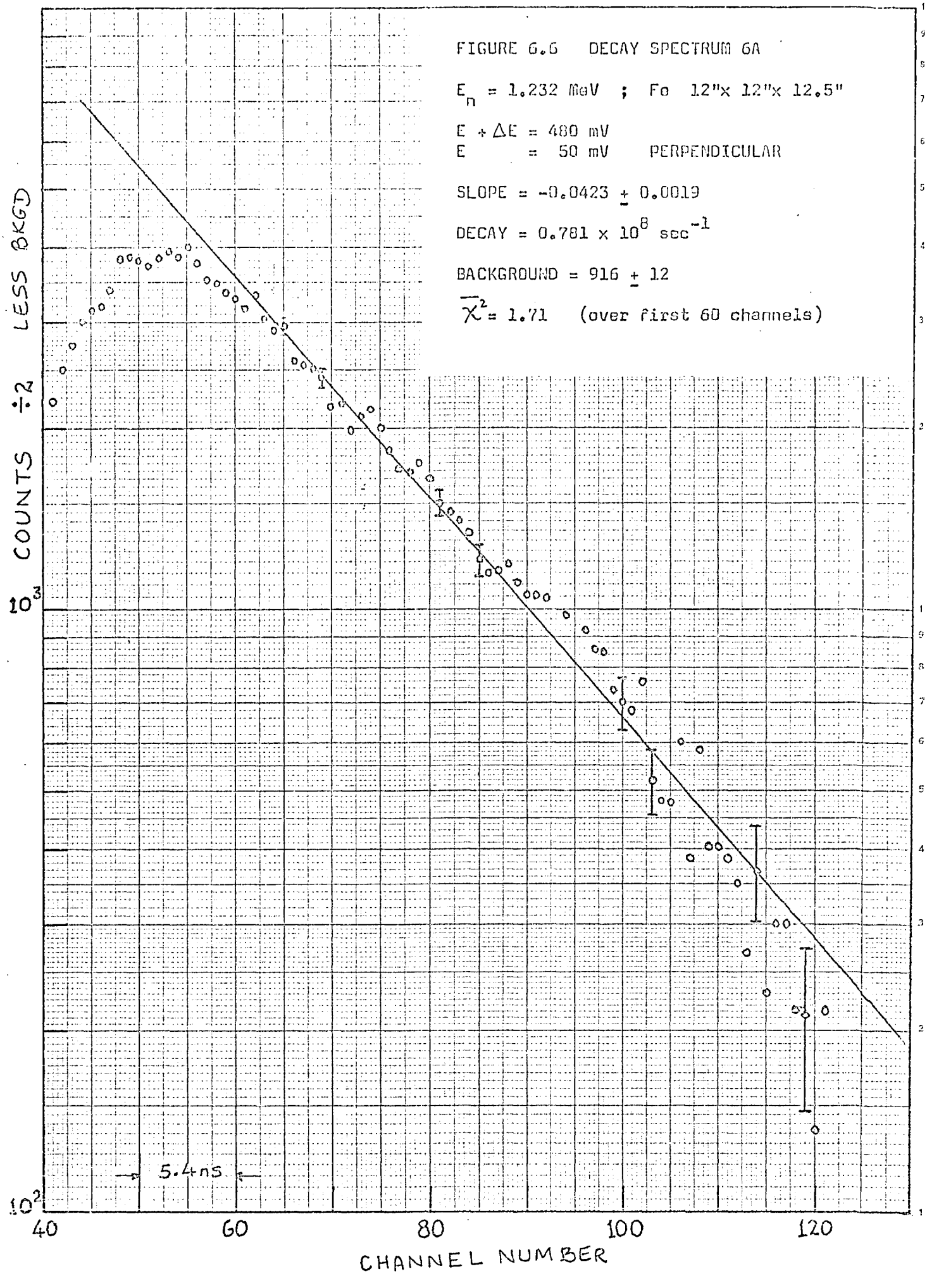

FIGURE 6.1 DECAY SPECTRUM 1A
E_n = 2.395 MeV ; Fe 12"x 12"x 12.5"
E +ΔE = 400 mV
E = 100 mV IN LINE
SLOPE = -0.0771 ± 0.0027
DECAY = 1.428 x 10^8 sec^{-1}
BACKGROUND = 171 ± 3
$\overline{\chi}^2$ = 1.99 (over first 60 channels)
COUNTS ÷4 LESS BKGD
10^3
10^2
5.4 ns
40
60
80
100
120
CHANNEL NUMBER

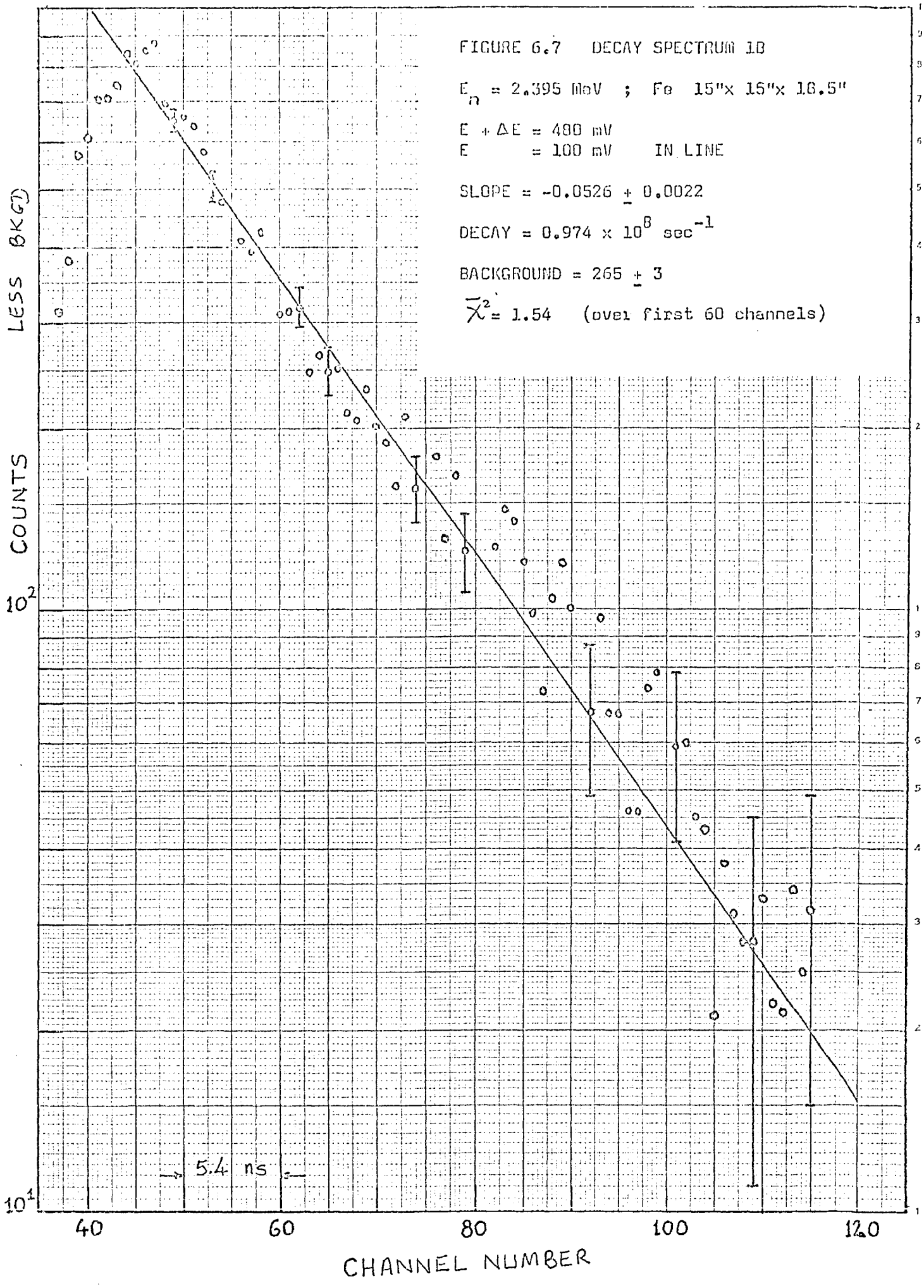

FIGURE 6.2 DECAY SPECTRUM 2A
E_n = 2.395 MeV ; Fe 12"x 12"x 12.5"
E + ΔE = 400 mV
E = 100 mV IN LINE
SLOPE = -0.0787 ± 0.0026
DECAY = 1.457 x 10^8 sec^{-1}
BACKGROUND = 173 ± 2
$\overline{\chi^2}$ = 1.11 (over first 60 channels)
COUNTS X2 LESS BKGD
10^2
10^1
5.4 ns
40
60
80
100
120
CHANNEL NUMBER

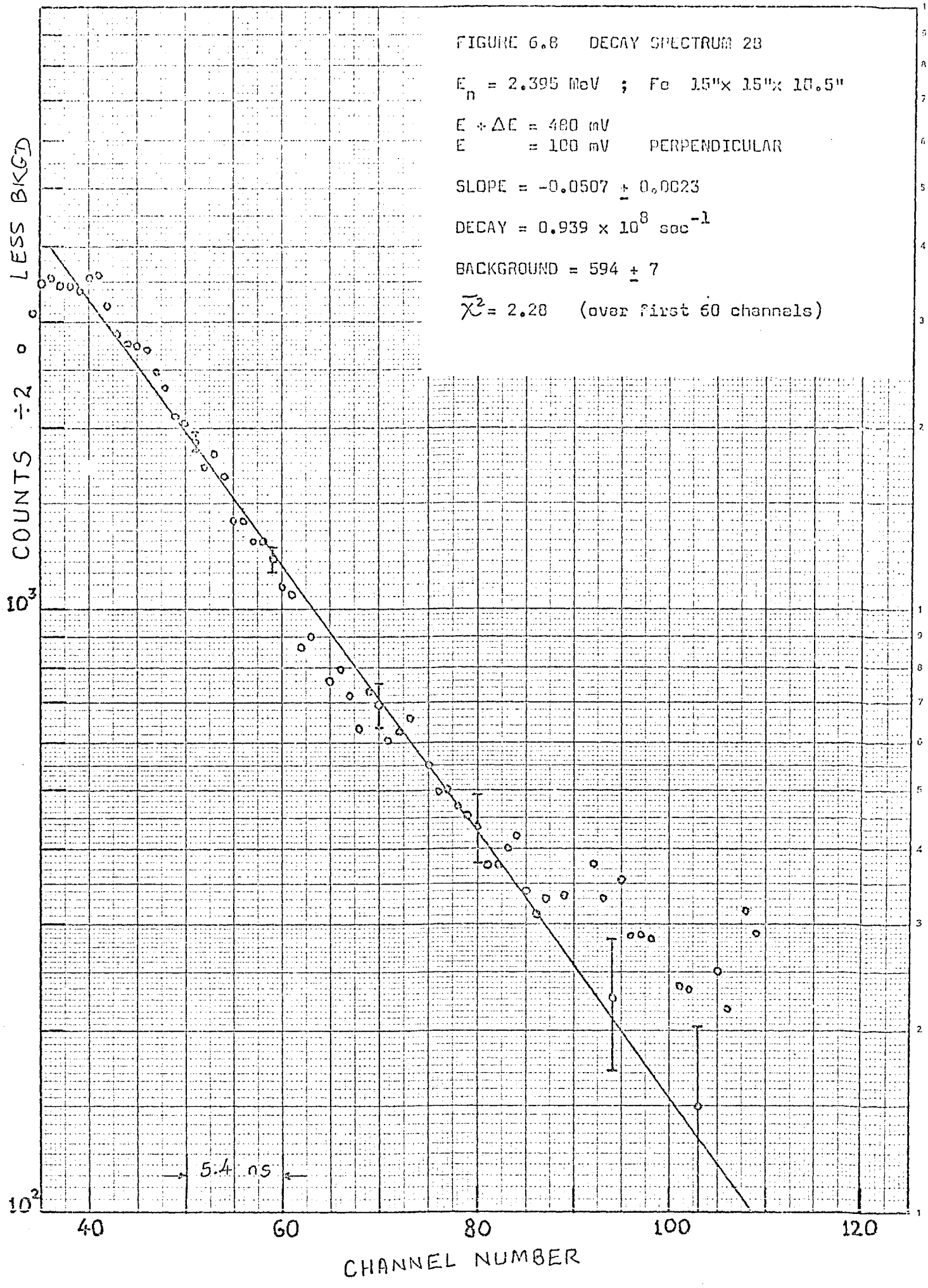

FIGURE 6.3 DECAY SPECTRUM 3A
E_n = 2.395 MeV ; Fe 12"x 12"x 12.5"
E +ΔE = 480 mV
E = 100 mV PERPENDICULAR
SLOPE = -0.0594 ± 0.0016
DECAY = 1.100 x 10^8 sec^{-1}
BACKGROUND = 478 ± 5
$\overline{\chi^2}$ = 1.54 (over first 60 channels)
COUNTS ÷2 LESS BKGD
10^3
10^2
5.4 ns
40
60
80
100
120
CHANNEL NUMBER

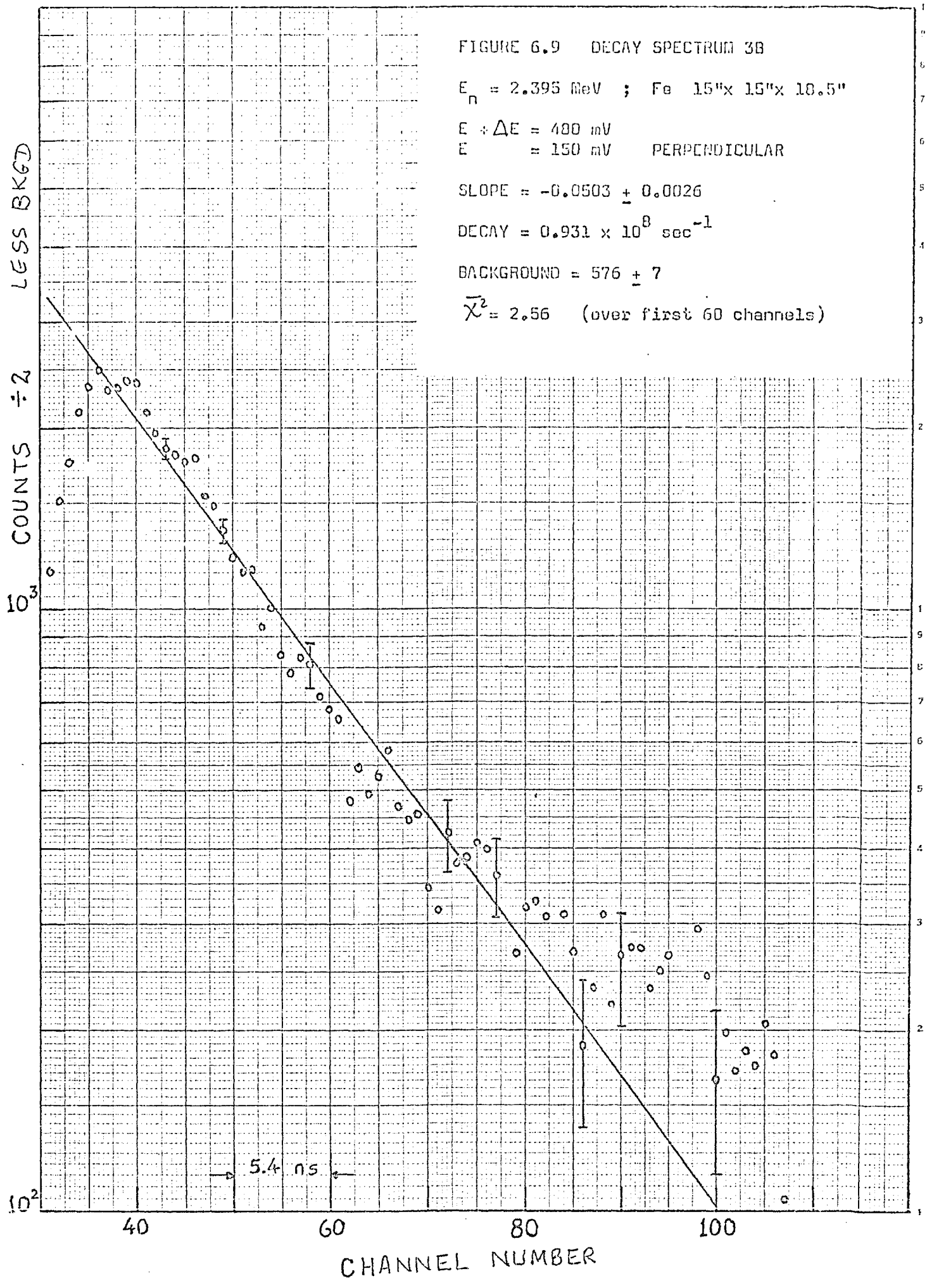

FIGURE 6.4 DECAY SPECTRUM 4A
E_n = 2.395 MeV ; Fe 12"x 12"x 12.5"
E + ΔE = 480 mV
E = 150 mV PERPENDICULAR
SLOPE = -0.0481 ± 0.0018
DECAY = 0.890 x 10^8 sec^{-1}
BACKGROUND = 659 ± 7
$\bar{\chi}^2$ = 1.76 (over first 60 channels)
COUNTS ÷2 LESS BKGD
10^3
10^2
5.4 ns
40
60
80
100
120
CHANNEL NUMBER

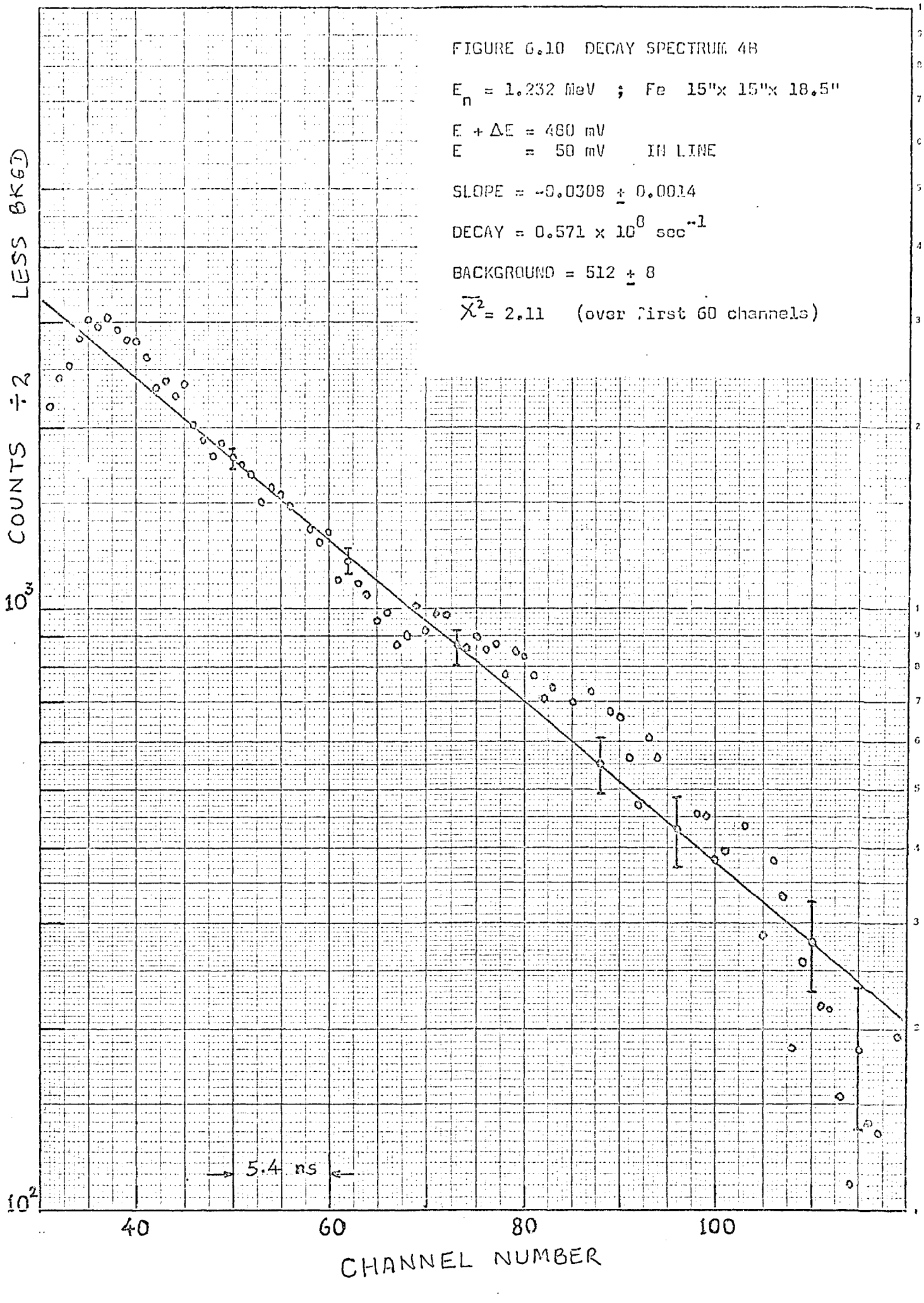

FIGURE 6.5 DECAY SPECTRUM 5A
E_n = 1.232 MeV ; Fe 12"x 12"x 12.5"
E +ΔE = 480 mV
E = 50 mV IN LINE
SLOPE = -0.0459 ± 0.0017
DECAY = 0.851 x 10^8 sec^{-1}
BACKGROUND = 377 ± 6
$\bar{\chi}^2$ = 1.65 (over first 60 channels)
LESS BKGD
COUNTS ÷2
10^3
10^2
5.4 ns
40
60
80
100
120
CHANNEL NUMBER

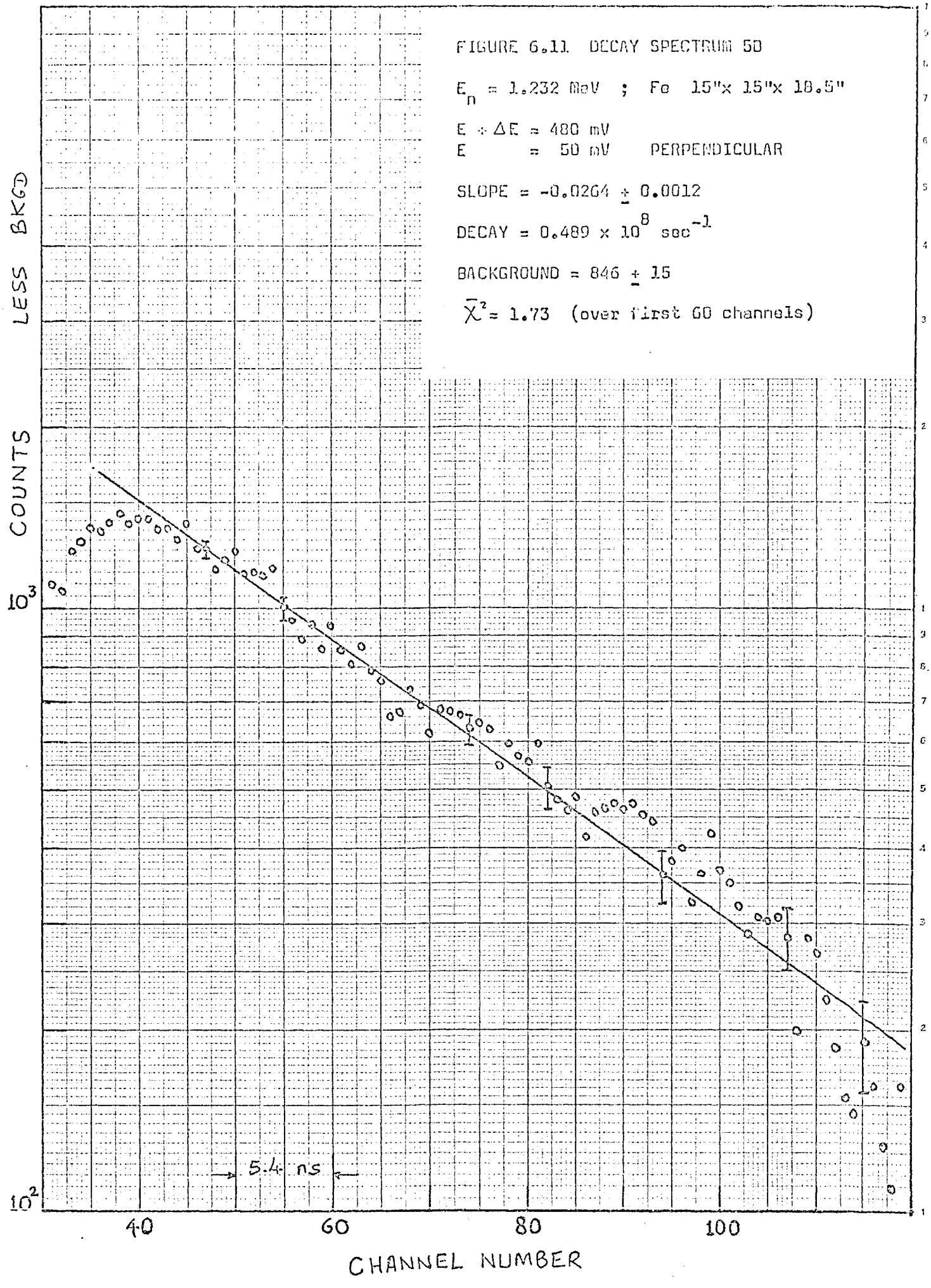

FIGURE 6.6 DECAY SPECTRUM 6A
E_n = 1.232 MeV ; Fo 12"x 12"x 12.5"
E + ΔE = 480 mV
E = 50 mV PERPENDICULAR
SLOPE = -0.0423 ± 0.0019
DECAY = 0.781 x 10^8 sec^{-1}
BACKGROUND = 916 ± 12
$\overline{\chi^2}$ = 1.71 (over first 60 channels)
COUNTS ÷2 LESS BKGD
10^3
10^2
5.4ns
40
60
80
100
120
CHANNEL NUMBER


FIGURE 6.7 DECAY SPECTRUM 1B
E_n = 2.395 MeV ; Fe 15"x 15"x 16.5"
E + ΔE = 480 mV
E = 100 mV IN LINE
SLOPE = -0.0526 ± 0.0022
DECAY = 0.974 x 10^8 sec^{-1}
BACKGROUND = 265 ± 3
$\bar{\chi}^2$ = 1.54 (over first 60 channels)
LESS BKGD
COUNTS
10^2
10^1
5.4 ns
40
60
80
100
120
CHANNEL NUMBER


FIGURE 6.8 DECAY SPECTRUM 28
E_n = 2.395 MeV ; Fe 15"x 15"x 18.5"
E + ΔE = 480 mV
E = 100 mV PERPENDICULAR
SLOPE = -0.0507 ± 0.0023
DECAY = 0.939 x 10^8 sec^{-1}
BACKGROUND = 594 ± 7
$\tilde{\chi}^2$ = 2.28 (over first 60 channels)
LESS BKGD
COUNTS ÷2
10^4
10^3
10^2
5.4 ns
40
60
80
100
120
CHANNEL NUMBER


FIGURE 6.9 DECAY SPECTRUM 3B
E_n = 2.395 MeV ; Fe 15"x 15"x 10.5"
E + ΔE = 480 mV
E = 150 mV PERPENDICULAR
SLOPE = -0.0503 ± 0.0026
DECAY = 0.931 x 10^8 sec^{-1}
BACKGROUND = 576 ± 7
$\bar{\chi}^2$ = 2.56 (over first 60 channels)
LESS BKGD
COUNTS ÷ 2
10^3
10^2
5.4 ns
40
60
80
100
CHANNEL NUMBER


FIGURE 6.10 DECAY SPECTRUM 4B
E_n = 1.232 MeV ; Fe 15"x 15"x 18.5"
E + ΔE = 480 mV
E = 50 mV IN LINE
SLOPE = -0.0308 ± 0.0014
DECAY = 0.571 x 10^8 sec^{-1}
BACKGROUND = 512 ± 8
$\overline{X^2}$ = 2.11 (over first 60 channels)
COUNTS ÷2 LESS BKGD
10^3
10^2
5.4 ns
40
60
80
100
CHANNEL NUMBER


FIGURE 6.11 DECAY SPECTRUM 5D
E_n = 1.232 MeV ; Fe 15"x 15"x 18.5"
E + ΔE = 480 mV
E = 50 mV PERPENDICULAR
SLOPE = -0.0264 ± 0.0012
DECAY = 0.489 x 10^8 sec^{-1}
BACKGROUND = 846 ± 15
$\bar{\chi}^2$ = 1.73 (over first 60 channels)
LESS BKGD COUNTS
10^3
10^2
5.4 ns
40
60
80
100
CHANNEL NUMBER

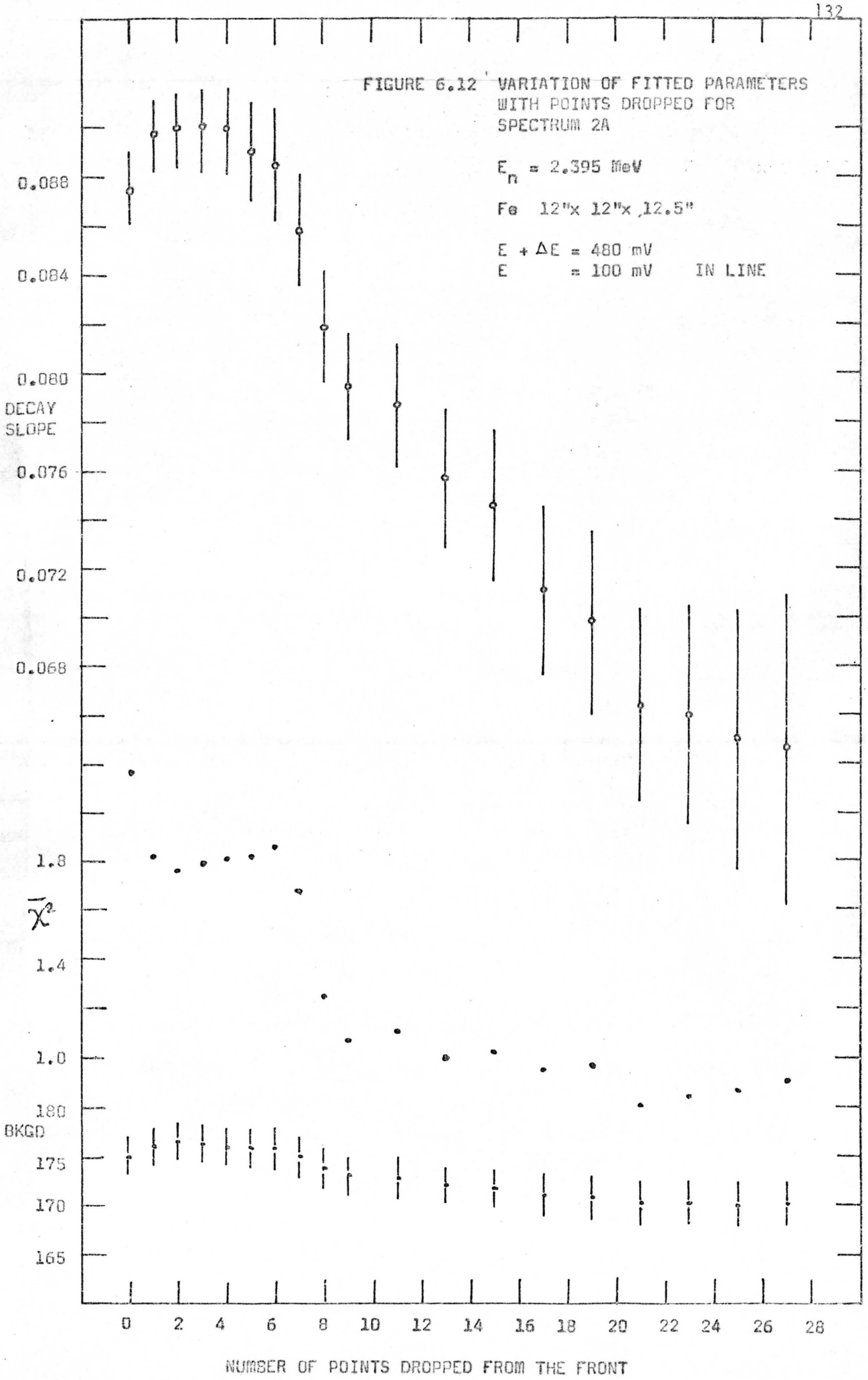

FIGURE 6.12 VARIATION OF FITTED PARAMETERS WITH POINTS DROPPED FOR SPECTRUM 2A
E_n = 2.395 MeV
Fe 12"x 12"x 12.5"
E + ΔE = 480 mV
E = 100 mV IN LINE
0.088
0.084
0.080
DECAY SLOPE
0.076
0.072
0.068
1.8
$\bar{\chi}^2$
1.4
1.0
180
BKGD
175
170
165
0 2 4 6 8 10 12 14 16 18 20 22 24 26 28
NUMBER OF POINTS DROPPED FROM THE FRONT

FIGURE 6.13 VARIATION OF FITTED PARAMETERS WITH POINTS DROPPED FOR SPECTRUM 18

E_n = 2.395 MeV Fe 15"x 15"x 18.5"

E + ΔE = 480 mV
E = 100 mV IN LINE

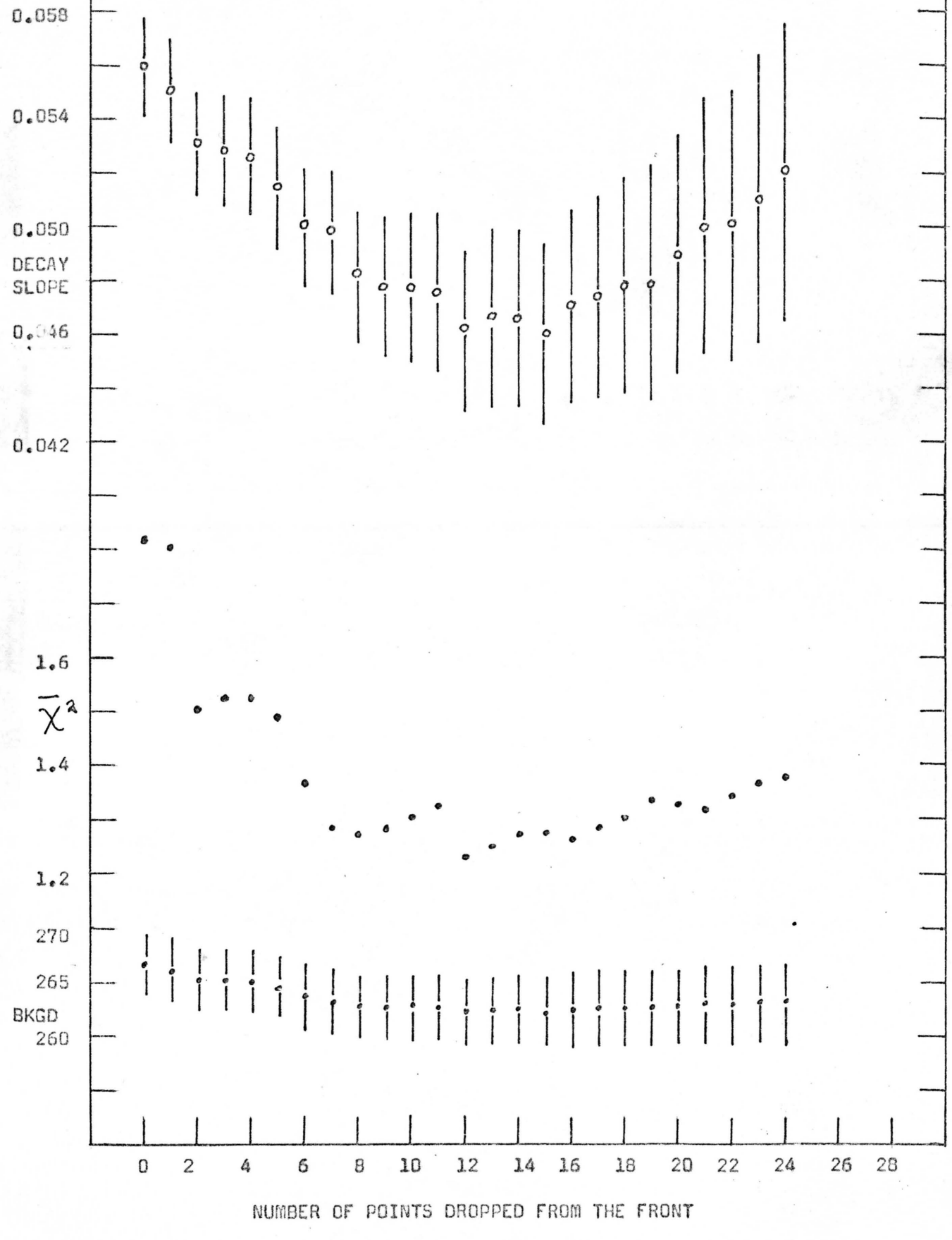
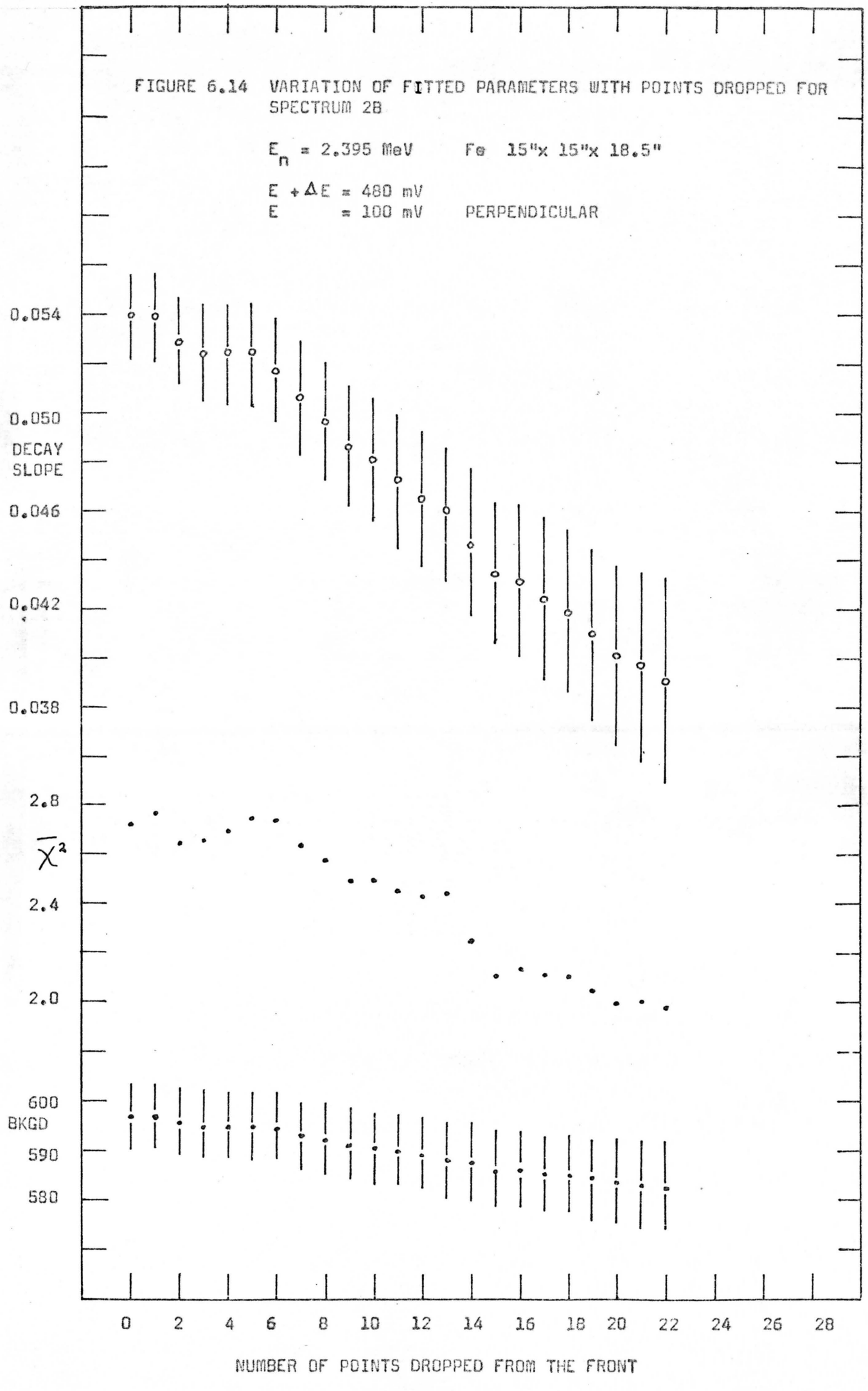


FIGURE 6.14 VARIATION OF FITTED PARAMETERS WITH POINTS DROPPED FOR SPECTRUM 2B

E_n = 2.395 MeV Fe 15"x 15"x 18.5"

E + ΔE = 480 mV
E = 100 mV PERPENDICULAR



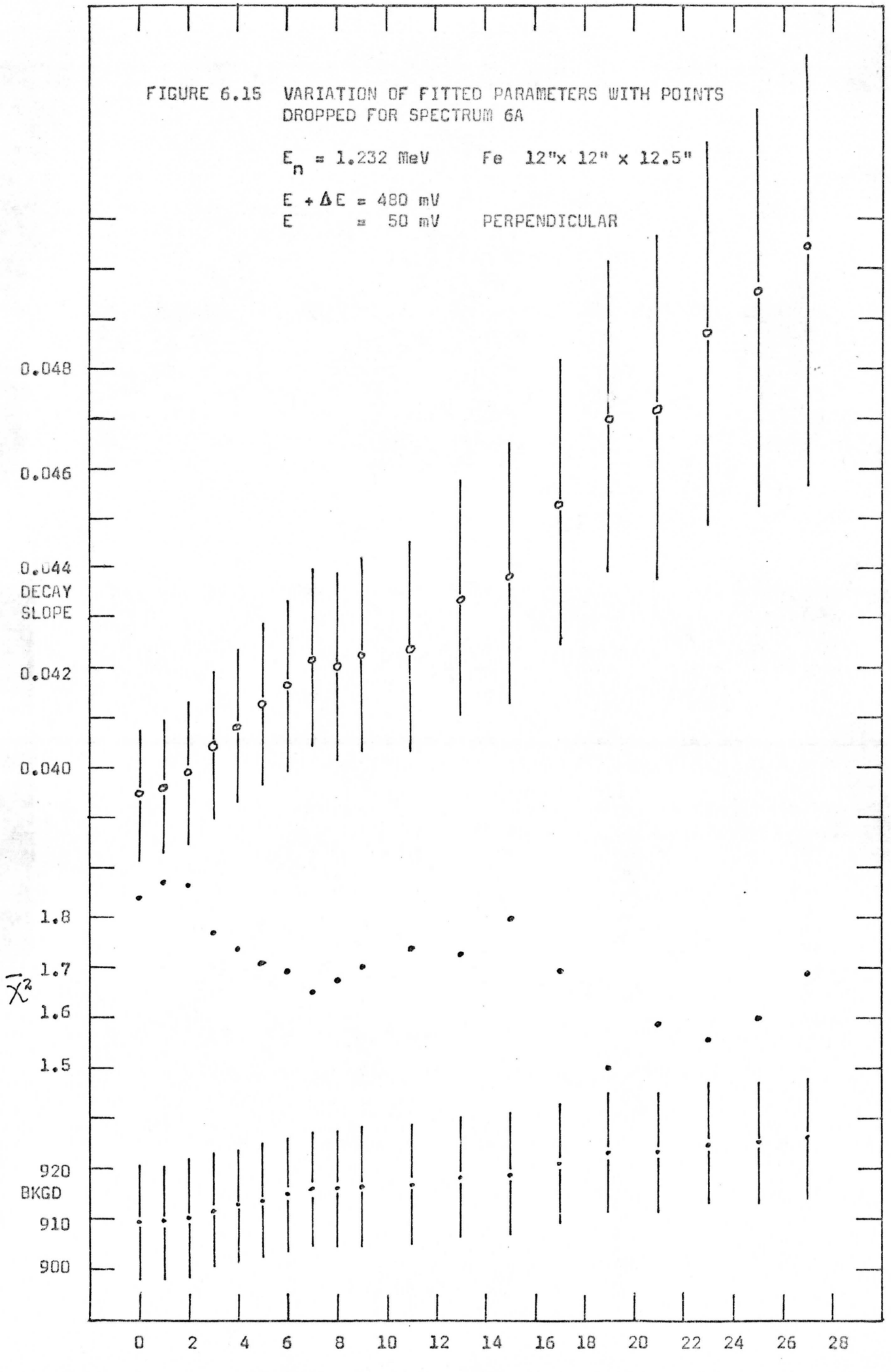

FIGURE 6.15 VARIATION OF FITTED PARAMETERS WITH POINTS DROPPED FOR SPECTRUM 6A
E_n = 1.232 MeV Fe 12"x 12" x 12.5"
E + ΔE = 480 mV
E = 50 mV PERPENDICULAR
0.048
0.046
0.044
DECAY SLOPE
0.042
0.040
1.8
1.7
1.6
1.5
$\bar{\chi}^2$
920
BKGD
910
900
0 2 4 6 8 10 12 14 16 18 20 22 24 26 28
NUMBER OF POINTS DROPPED FROM THE FRONT

FIGURE 6.16 VARIATION OF FITTED PARAMETERS WITH POINTS DROPPED FOR SPECTRUM 48

E_n = 1.232 MeV Fe 15"x 15"x 18.5"

E + ΔE = 480 mV
E = 50 mV IN LINE

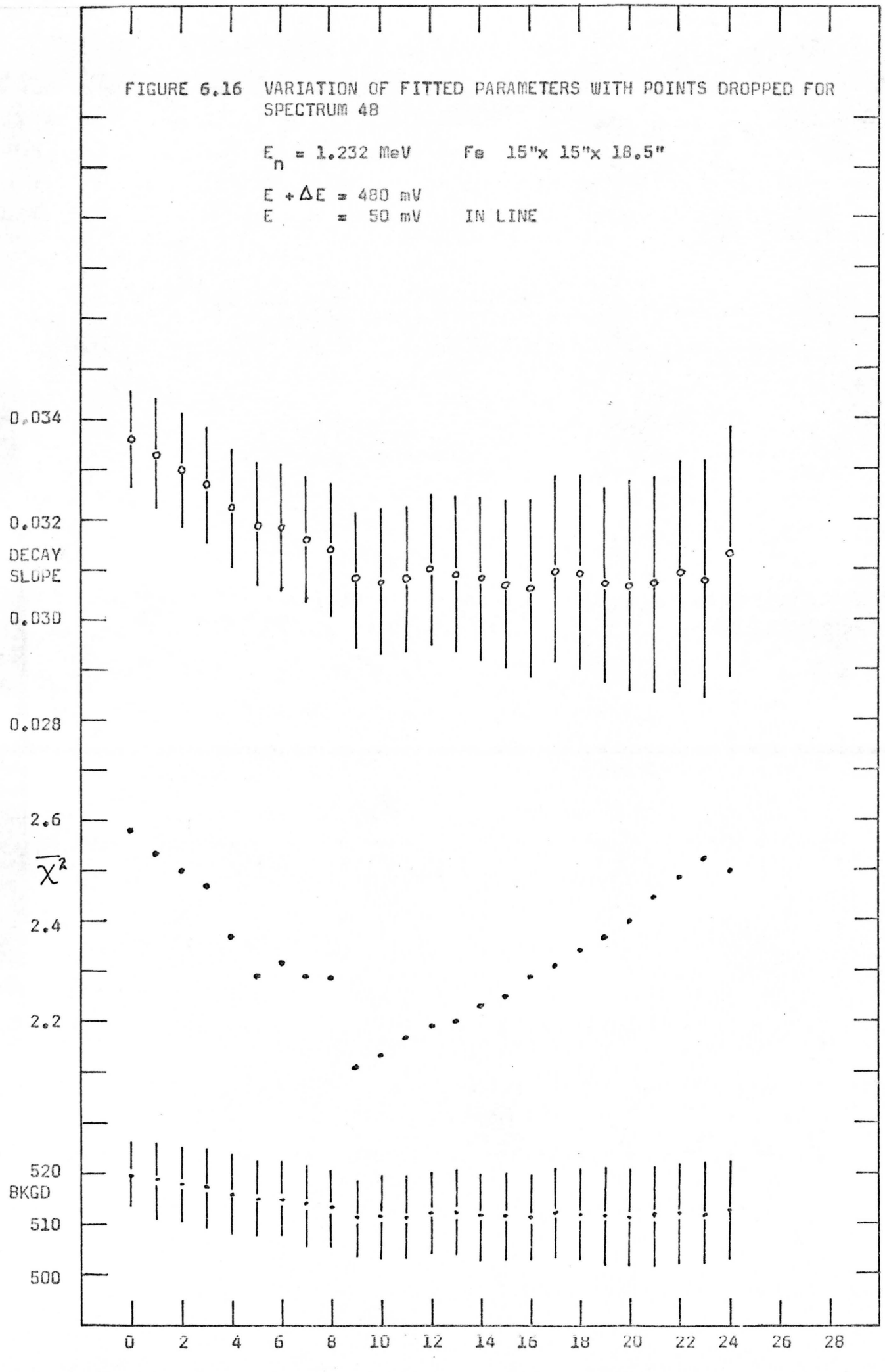


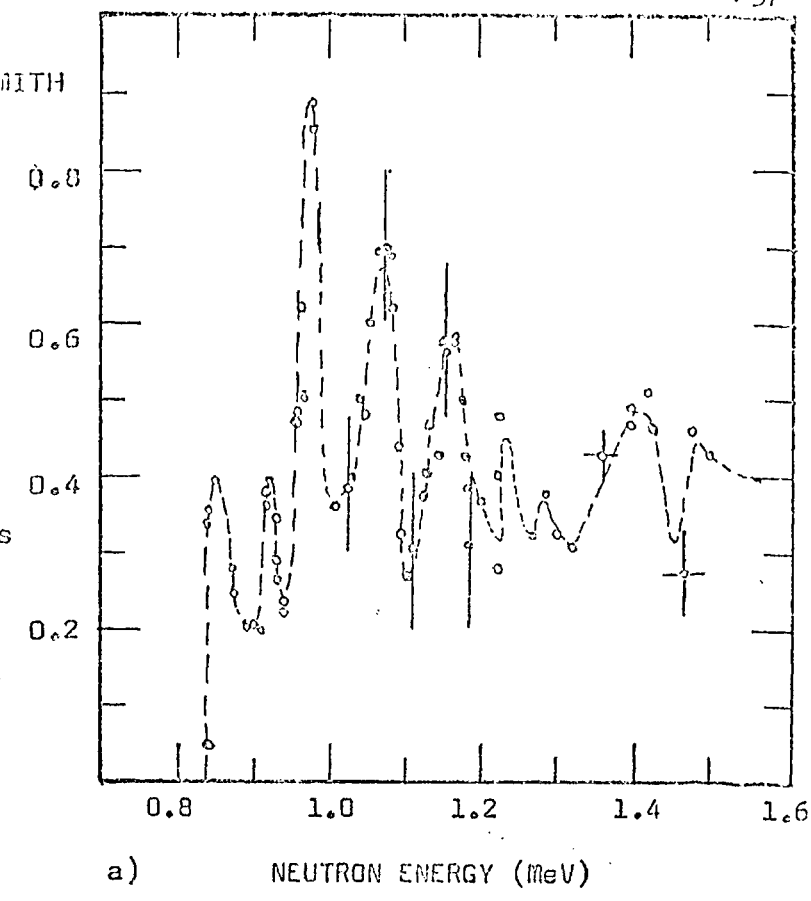
FIGURE 6. 17 DATA FROM A.B.SMITH FOR IRON

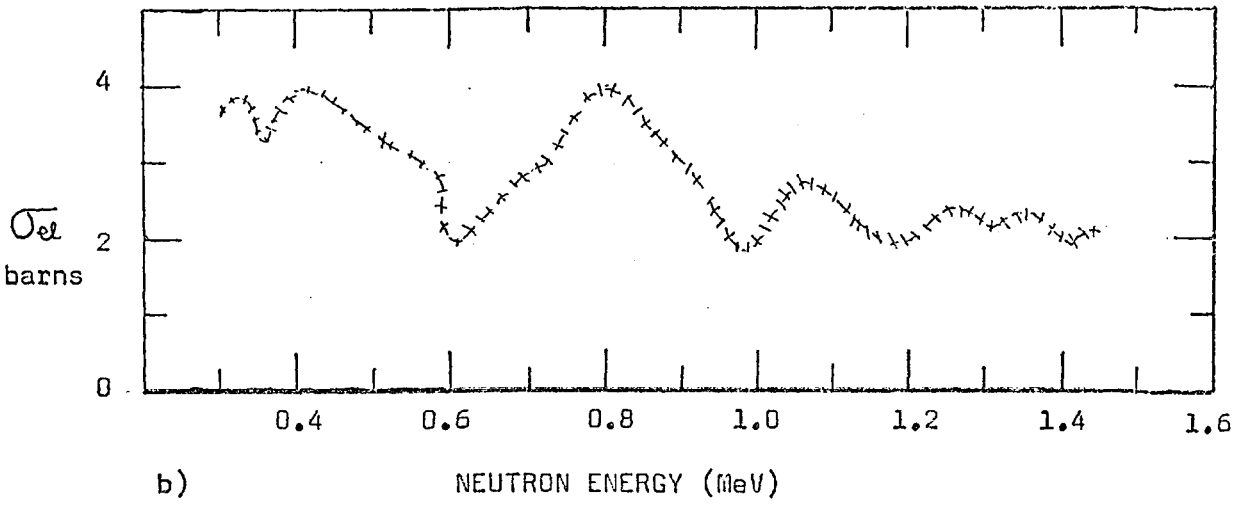
a) Inelastic excitation of the 850 keV state.

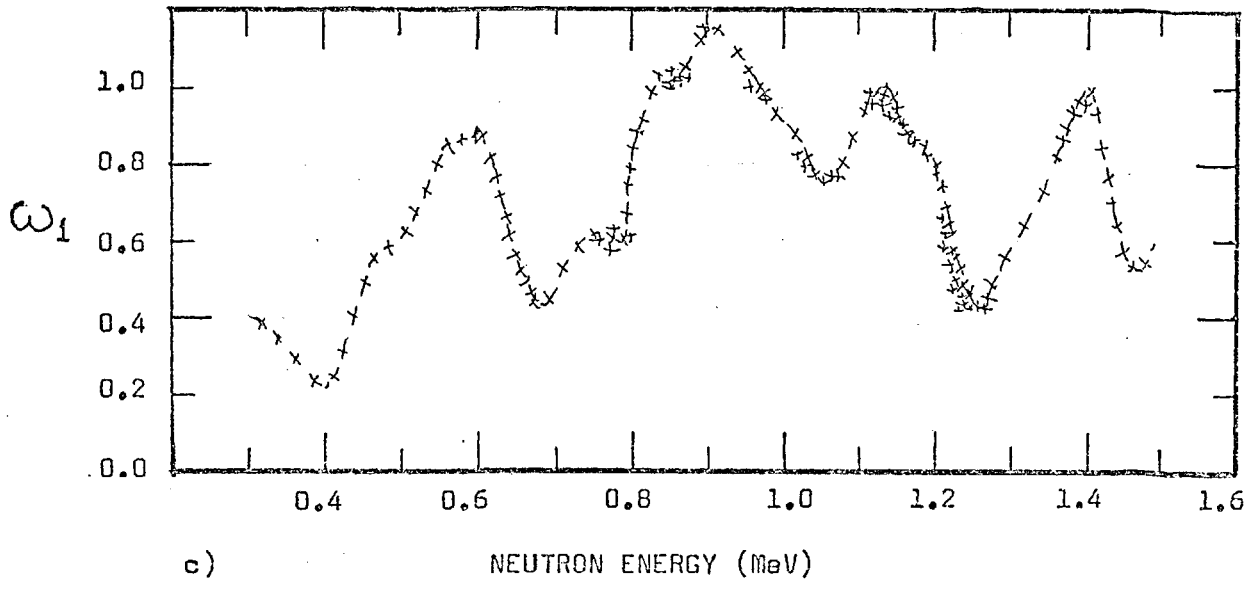
b) Elastic scattering cross section.

c) First coefficient of the Legendre expansion of the angular distributions.

$\bar{\mu}_0 \approx \omega_1/3$







CHAPTER 7

CONCLUSION

The experiment has shown that when energy gating was applied to bias the neutron detector so as not to count neutrons which had lost energy it was possible to measure some kind of decays. These spectra fitted well to a single exponential plus background. Unfortunately interpretation of the results was rendered difficult by the relatively high background contingent to such fast pulsed experiments and by the presence of room scattered neutrons. These troublesome sources were very much in evidence in the present experiment where adequate precautions to minimise these effects could not be taken because of the limited time. The spectra could well have been "sitting on top" of a time dependent background which was not investigated. Another source of error was the low counting statistics. It needed a time of around 2 hours to register a peak value of merely 2000 counts. The estimated energy spread was from $\pm$ 38 keV to $\pm$ 59 keV so that it included several resonances of the cross-sections used, the latter having resolution of 20 keV or less. However that was the best that could be achieved with the set-up used.

This project is the first of its type to be conducted in the United Kingdom to the best knowledge of the author and in his opinion it would be worthwhile to carry out further investigations along this line. To help improve the technique and reduce the errors the following suggestions are made.

a) The neutron yield should be increased by using higher proton currents and richer targets. The detector should be moved as near to the target as practical manoeuvring of the metal slabs would permit. This would ensure better counting statistics.

b) The room in which the experiment is performed must be free of scattering materials and it might even be worthwhile to shield the detector with paraffin. The beam tube must be some height from the floor. To test the effect of background it is suggested that the neutron beam be blocked by a slab of paraffin with the metal assemblies and detector placed in position as for the decay measurements. In this way the behaviour of the background, especially in those channels which would later be occupied by the decay spectra, could be observed. The importance of performing this cannot be overstressed.

c) As has been mentioned in Chapter 5 the neutron energy spectrum was contaminated by target gamma rays since the latter could only be separated out in time. A way of eliminating the gammas is to gate the energy spectrum itself by the time spectrum from the time-to- amplitude converter, the gamma peak in the latter being excluded by using a differential discriminator. The "purified" energy spectrum is then used to gate the time spectrum from the other output of the converter. An alternative solution is to insert a pulse shape (n,γ) discrimination circuit at the base of the detector. However this would mean using a different phosphor, possibly a liquid such as NE 213. The slower decay time of the liquid phosphor and the added electronics would conceivably increase the time resolution.

d) To further reduce background due to random gammas and elastically scattered neutrons, a twin detector might be a better proposition than a single detector.

As many as six bucklings should be used so that the results could be fitted according to the analytical expansion formula. The number of energies might also be increased. The technique could be extended to multiplying media such as natural uranium and to assemblies containing

slabs of different materials. If the above procedures for reducing errors are adopted it will be interesting to see whether errors to within 10% or even less can be achieved.

REFERENCES

1. ASKEW J.R. and BRISSENDEN R.J. Some improvements in the Discrete Ordinate Method of B.G. Carlson for solving the Neutron Transport Equation. AEEW-R161 (1963).
2. BECKURTS K.H. A review of pulsed neutron experiments on non-multiplying media. Symp. Pulsed Neutron Research, Karlsruhe (1965). I.A.E.A. (SM-62/1)pp. 3/32.
3. BEGHIAN L.E. et al. Journ. Nucl. Sci. Eng. 15 (1963) pp. 357/81.
4. BEGHIAN L.E. et al. Journ. Nucl. Sci. Eng. 17 (1963) pp. 82/89.
5. BEGHIAN L.E. et al. The Pulsed Neutron Technique applied to Fast Non-multiplying Assemblies. Symp. Pulsed Neutron Research (1965). I.A.E.A. (SM-62/74) pp. 511/26.
6. BIRKS J.B. The Theory and Practice of Scintillation Counting. Pergamon Press (1954). p. 187.
7. CARLSON B.G. Numerical Solution of Transient and Steady State Neutron Transport Problems, LA 2260 (1959).
8. CARLSON B.G. The Numerical Theory of Neutron Transport. Methods of Computational Physics. Acam. Press 1963, pp. 1/42.
9. CARLSON B.G. Numerical Formulation and Solution of Neutron Transport Problems. LA 2996 (1963).
10. d'OULTREMONT P. et al. Contribution to the Study of Fast Neutron Non-Multiplying Assemblies by the Pulsed Neutron Technique. Symp. Pulsed Neutron Research (1965). I.A.E.A. SM-62/4, pp. 493/510.
11. GATTI E. and SVELTO V. Nucl. Inst. Meth. 43 (1966), pp. 248/68.
12. GLASSTONE S. and EDLUND M.C. The Elements of Nuclear Reactor Theory. Van Nostrand (1963), p. 97.
13. GODDARD A.J.H. Private Communications.
14. HEATH R.L. I.R.E. Trans. Nucl. Sci. NS9 [3] 196] p. 294.

15. HIRAOKA T. et al. Nucl. Sci. Technology 1 (1964) pp. 108/09

16. JOHNSON P.W. Ph.D. Thesis London University 1966.

17. LANGNER et al. Tables of evaluated Neutron Cross Sections for Fast Reactor Materials. KFK 750 Karlsruhe (1968).

18. LANGSDORF Jr. A. et al. Neutron Scattering Angular Distribution. ANL 5567 Revised (1961).

19. LATHROP K.D. DTF IV, a FORTRAN IV Program for solving the Multigroup Transport Equation with Anisotropic Scattering. LA-3373 (1965).

20. LEE C.E. The Discrete S_n Approximation to Transport Theory. LA 2595 (1961).

21. MACRACKEN D.D. and DOM W.S. Numerical Methods and Fortran Programming. Wiley Int. 1964.

22. MARION J.B. and FOWLER J.L. Fast Neutron Physics Vols. I & II. Interscience (1963).

23. MATHER D.S. Priviate Communication.

24. MULLARD Handbook on Photomultiplier Tubes.

25. NELKIN M. Nucl. Sci. Eng. 7 (1960) p. 210.

26. NISHIMURA et al. Nucl. Phys. 70 (1965) p. 421.

27. POST R.F. and SCHIFF L.J. Phys. Rev. 80 (1950) p. 1113.

28. PRESCOTT J.R. and RUPALL A.S. Canad. J. Phys. 39 (1961) p. 221.

29. SMITH A.B. Inelastic Neutron Scattering; a Compendium. Proc. Int. Conf. on the Study of Nuclear Structure with Neutrons, Antwerp (1965).

30. STORRER F. Pulsed Neutron Experiments on Fast and Intermediate Systems. Symp. Pulsed Neutron Research. (1965). I.A.E.A. (SM-62/88) pp. 317/36.

31. WILLIAMS M.M.R. Proc. Brookhaven Conf. on Neutron Thermalization. BNL 719 (C-32) 1962, Vol. IV, p. 1331.

32. YIFTAH S et al. Fast Reactor Cross Sections. Pergamon Press (1960) p. 71.

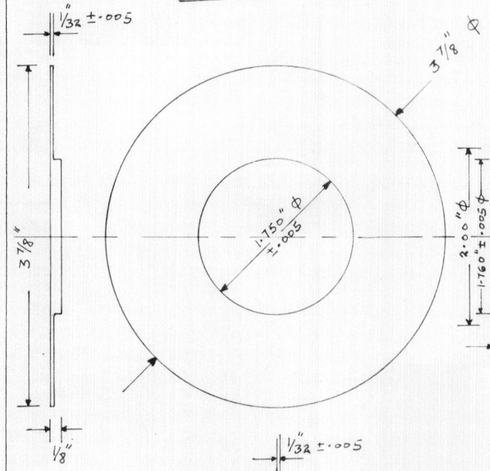
33. GREENSPAN H., KELHER C.N. and OKRENT D (eds.) Computing Methods In Reactor Physics (1968) Gordon Breach.

34. WIGNER E.P. and WEINBERG A.M. The Physical Theory of Neutron Chain Reactors. Chicago Univ. Press (1958).

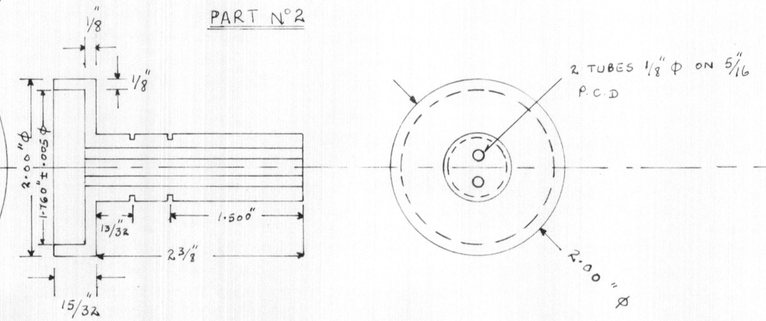
DRAWING NUMBER

LIMITS ON DIMENSIONS		
DEC	±	010"
FRACT	±	1/32"
DEC MM	±	0·25 MM
UNIT MM	±	1 MM
UNLESS SPECIFIED		

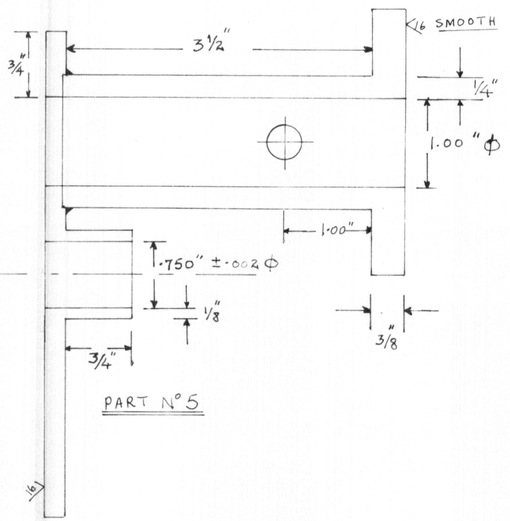
PART N°1



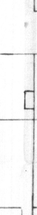
PART N°2



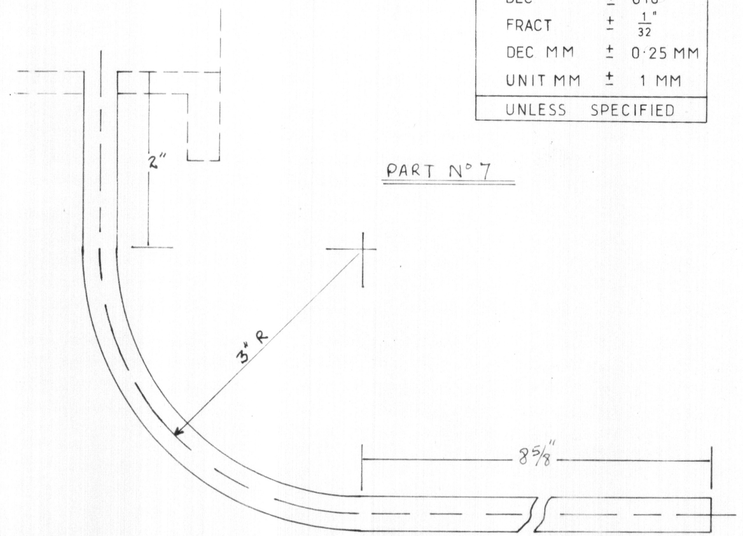
PART N°4



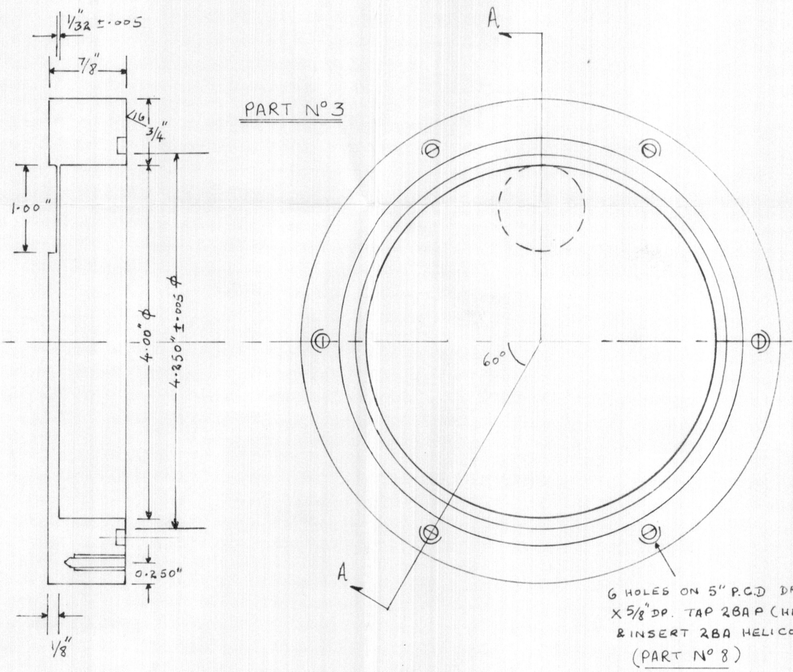
PART N°5



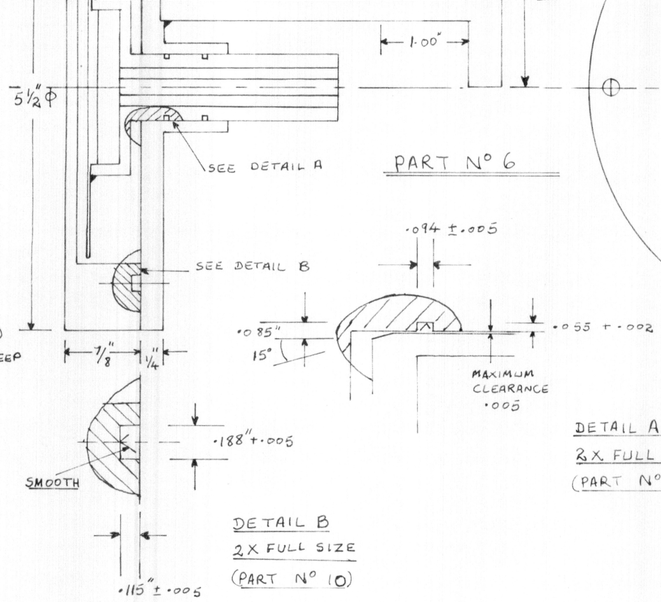
PART N°7



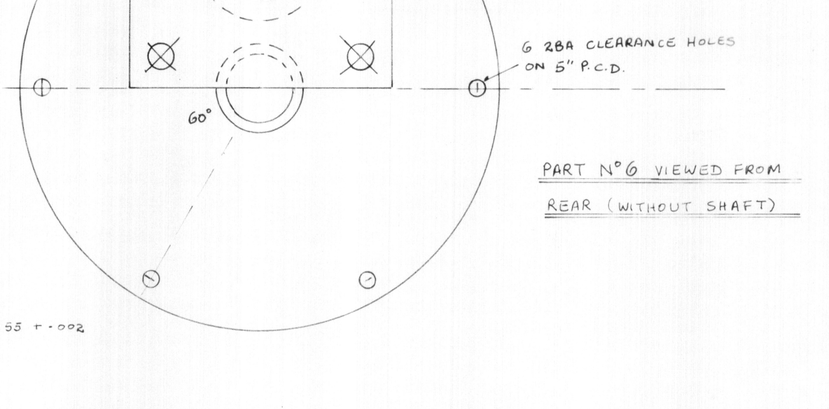
PART N°3



SECTION AA



PART N°6



PART N°6 VIEWED FROM REAR (WITHOUT SHAFT)

DETAIL A
2X FULL SIZE
(PART N° 9)

DETAIL B
2X FULL SIZE
(PART N° 10)

NOTE

1) ITEMS 1 & 2 TO BE BRAZED OR WELDED TOGETHER. WELD TO BE VACUUM TIGHT
2) ITEM 4 TO BE BRAZED OR WELDED ONTO ITEM 5. WELD TO BE VACUUM TIGHT
3) ITEM 7 TO BE BRAZED OR WELDED INTO ITEM 4. WELD TO BE VACUUM TIGHT
4) ALL EXTERNAL CORNERS ·030"/45° CHAMFER UNLESS STATED
5) ALL INTERNAL CORNERS ·030"R MAXIMUM UNLESS STATED
6) ITEM 9 FOR 'O' RING SEALS ·614" ±·005 I.D. X ·070" ±·003 X SECTION J. WALKER CHART N° 50A 50-016 (ON ORDER)
7) ITEM 10 FOR 'O' RING SEAL 4.234" ±·015 I.D X ·139" ±·004 X SECTION J. WALKER CHART N° 50A 50-244 (ON ORDER)

PART Nº	Nº OFF	DESCRIPTION	MATERIAL	REMARKS
10	1	GROOVE FOR 'O' RING SEAL		SEE NOTE
9	2	GROOVES FOR 'O' RING SEALS		SEE NOTE
8	6	2BA HELICOIL INSERT		
7	1	VACUUM CONNECTION	BRASS	3/8" O.D. x 1/4" I.D.
6		ASSEMBLY IN SECTION		
5	1	BACK PLATE	BRASS	
4	1	HOLDER	BRASS	
3	1	FRONT COVER PLATE	BRASS	
2	1	ROTATING SHAFT WITH COOLING TUBES	BRASS	
1	1	ROTATING DISC	BRASS	

Mechanical Engineering Dept.	DRAWN	R. S. H. LEE	SCALE	TITLE	ROTATING TARGET ASSEMBLY	CLASS	DRAWING NUMBER
Imperial College	APPROVED		1/1				R. T. A. 1.
London S.W. 7	TRACED		DATE	AMMDTS		GROUP	NAME
	CHECKED						